Title

Improving Biomass-Burning Smoke Properties, Evolution, Emissions, and Air Quality Forecasts in Models

Permalink

https://escholarship.org/uc/item/10f4k7m8

Author

Howes, Calvin

Publication Date

2024

Peer reviewed|Thesis/dissertation

UNIVERSITY OF CALIFORNIA

Los Angeles

Improving Biomass-Burning Smoke Properties, Evolution, Emissions, and Air Quality Forecasts in Models

A dissertation submitted in partial satisfaction

of the requirements for the degree Doctor of Philosophy

in Atmospheric and Oceanic Sciences

by

Calvin Howes

2024

ABSTRACT OF THE DISSERTATION

Improving Biomass-Burning Smoke Properties, Evolution, Emissions, and Air Quality Forecasts in Models

by

Calvin Howes
Doctor of Philosophy in Atmospheric and Oceanic Sciences
University of California, Los Angeles, 2024
Professor Pablo Saide Peralta, Chair

Aerosol modeling is central to both climate projections and air quality forecasts. In climate modeling, the total estimated aerosol radiative forcing uncertainty range (-2 to -0.6 W m^{-2} in IPCC AR6) is dominated by that of aerosol-cloud interactions (-1.7 to -0.3 W m^{-2}). These interactions depend on the properties of the aerosol population as well as its evolution and transport over long distances. In particular, smoke from burning biomass undergoes drastic and poorly-constrained evolutionary changes throughout its lifetime. Smoke emissions are typically estimated from satellite observations that are vulnerable to sensor deficiencies or cloud cover, and, lacking a reference source of truth, emissions inventories have large discrepancies in emission amounts. Smoke composition, size distribution, and vertical placement are best quantified from limited and expensive in situ observations. These limitations, coupled with the complex and variable impact of smoke particles on cloud nucleation, create significant uncertainties in assessing smoke's overall influence on radiative budgets and human health.

In this dissertation, I address the task of reducing these uncertainties in the modeling of biomass-burning smoke. The southeastern Atlantic provides an excellent study region for smoke's climatic impacts and evolution, as it has enormous smoke emissions from burning in southern Africa, coupled with a near-permanent offshore stratocumulus cloud deck. We evaluate WRF-CAM5, CESM, and E3SM with observations from three overlapping field campaigns in the southeastern Atlantic in 2017—ORACLES, CLARIFY, and LASIC. The wide spatial extent of the campaigns and the redundancy of several observations provide an excellent basis from which to understand smoke properties. I find that the models often lack important aerosol chemical processes in both the free troposphere and boundary layer, as well as inaccurate cloud properties and responses to aerosols. I implement sensitivity tests to two global earth system models, CESM and E3SM. As a result, I show that aerosol oxidation in the free troposphere is likely driving the loss of 25-50% of organic aerosol mass over timescales of ~4-12 days through this region, a process which E3SM and WRF-CAM5 initially lacks. I also demonstrate that dimethyl sulfide emissions and this oxidative loss are key factors representing the nearly tripling of sulfate by mass fraction in the boundary layer from the free troposphere. Modeled cloud droplet number concentration is shown to be highly sensitive to updraft biases. By doubling updraft strength in E3SM and CESM in line with aircraft measurements, I reduce the normalized mean bias against observed cloud droplet nucleation efficiency by ~25% on average.

I further improve smoke emissions for air quality forecasts by using Doppler weather radar to improve wildfire emissions during the record-breaking 2020 western United States wildfire season. Previous satellite-based emissions estimates during this period are plausibly underestimated by an order of magnitude or more during the largest and most intense fire periods. Correcting for emissions gaps in WRF-Chem reduces bias in AOD by 5-50% and decreases bias in surface $PM_{2.5}$ from -25% to +3% over the entire western US. For both variables, improvements are larger when focusing on the strongest burning regions and time periods. This thesis outlines significant overall improvements in smoke chemical modeling that stand to improve both long-term climate projections and short-term air quality forecasting and early-warning systems.

The dissertation of Calvin Howes is approved.

Gang Chen

Paquita Zuidema

Jasper F Kok

Pablo Saide Peralta, Committee Chair

University of California, Los Angeles

2024

Table of Contents

List of Figures

Figure 2.4: Hygroscopicity and the corresponding properties of smoke in the FT+BL between model and observations. (a) Hygroscopicity from WRF-CAM5 (green), first with all species then excluding dust and chloride to match AMS (‘mod’ subscript), AMS-based, and data from the Nenes group, grouped and then disambiguated by CCN supersaturation setting. Calculations were made with the CCN and GIT UHSAS together; (d, g, f) Hygroscopicity from WRF-CAM5 and AMS for each campaign and atmosphere level. (b, c, e, f, h, i, k, l) average composition by mass fraction of smoke in ORACLES and CLARIFY FT and BL, and colocated WRF-CAM5 samples. Model OA here includes secondary OA, a distinct model variable. WRF-CAM5 SOA was generally less than 3% of total mass.

Figure 2.5: Aging trends in FT for mean diameter (a, c) and OA:BC mass ratio (b, d). Sample sizes for each box-whisker are listed at top of each figure. Observational data are filtered for total aerosol mass>10 μg m^{-3} and rBC mass>0.1μg m^{-3}, and same subset is then sampled in WRF-CAM5. Black diamonds represent mean, red lines represent median.

Figure 2.6: Time series of smoke properties at ASI in August 2017. Vertical dashed lines delineate periods of smoky, medium, and clean conditions. a-b) refractory BC and CO concentration, respectively. Overlaid on both are rainfall accumulation from WRF-CAM5, LASIC, and UK Met devices summed on each day; c) Accumulation mode number concentration; d) Accumulation mode geometric mean diameter; e) Hygroscopicity from the CCN and SMPS from LASIC, and bulk composition in the accumulation mode in WRF-CAM5; f) PBL inversion height from WRF-CAM5, from the LASIC radiosonde VAP, and recalculated from radiosonde matching the algorithm applied to WRF-CAM5; g) inversion

strength from WRF, from the LASIC radiosonde VAP, and recalculated from radiosonde profiles using the same algorithm as applied to WRF-CAM5.

Figure 2.7: Number and volume distributions from LASIC selected to be representative of the range of conditions during smoky, medium, and clean conditions at ASI. WRF-CAM5 plots show the sum of the accumulation and nucleation mode lognormals.

Figure 2.8: Histogram of 3-hourly rain rate measured by LASIC. In the legend, n represents the total number of rain events sampled over the detection threshold of 0.05mm per hr. Note UK Met rain data is only archived daily and is not included here.

Figure 2.9: Observed and modeled cloud properties and BL turbulence. (a-b) Cloud droplet number (weighted by LWC) compared against below-cloud aerosol concentration from observations and WRF-CAM5 in (a) ORACLES and (b) CLARIFY cloud transects. Axes of (a) and (b) show kernel PDFs of each distribution, on the same scale. c-d) Normalized PDFs of activation efficiency, the ratio N_{CLD}/N_{AER} for each campaign and WRF-CAM5. Diamonds on the x-axes represent the median of the like-colored population. (e-f) Spectra of BL turbulent updrafts from each campaign WRF-CAM5 between 100m and 700m. Note: aerosol number concentration in observations is taken from PCASP for consistency across campaigns, which has a lower size limit of ~110nm. This cutoff was virtually imposed on the WRF-CAM5 size distribution as well for this figure.

Figure 3.1: Smoke properties from models and corresponding observations in ORACLES and CLARIFY campaigns. (a, d) geometric-mean particle diameter in the accumulation mode; (b, e) number concentration, (c, f) mass concentration. Distribution means are given

by black diamonds, medians are red horizontal lines, and red crosses are outliers (greater than 1.5 times the interquartile range beyond the box). Note the CLARIFY campaign only provided sizing data from the PCASP instrument.

Figure 3.2: Aerosol composition breakdown in the FT and BL. FT figures (a-c, g-j) are selected from a minimum smoke concentration, while BL figures (d-f, k-n) are selected based on altitude. All figures combine samples from both ORACLES and CLARIFY campaigns. Species shown here are only the ones directly represented in both observations and models. Dust and chloride are excluded from model composition, while NO_3 and NH_4 are excluded from AMS observations.

Figure 3.3: Aging trends in particle mean diameter (a, c) and organic aerosol to black carbon (OA:BC) mass ratio (b, d). Figures a-b compare trends $E3SM_{BASE}$ and $CESM_{BASE}$ against observations, while figures (c-d) show $E3SM_{BASE}$ and its sensitivities to changes in the photolysis scheme. Solid lines are the mean of values binned into each day or range, and the shaded region represents the standard deviation.

Figure 3.4: Aerosol-cloud activation efficiency and turbulence in ORACLES (top) and CLARIFY (bottom) in both observations (orange) and colocated models (blue). Columns 1 and 3 show baseline model performance in E3SM and CESM, respectively, for each quantity. Columns 2 and 4 show performance in the builds with doubled updraft strength in the cloud activation scheme, $E3SM_{2W}$ and $CESM_{2W}$ respectively.

Figure 3.5: Maps of average smoke and aerosol properties through the SEA region during August 2017, showing both the base model values and the difference from the modified builds. Figs. a-f show OA mass fraction in the smoky FT. Base performance is shown for

E3SM (a) and CESM (e), and differences against the base configuration for each model in (b-d, f). The same layout follows for geometric mean diameter of FT smoke (g-l) and boundary layer SO_4 mass fraction (m-r).

Figure 3.6: Maps of average cloud properties through the SEA region during August 2017, showing both the base model values and the difference from the modified builds. (a-d) show average low cloud fraction. Base performance is shown for E3SM (a) and CESM (c), and differences when increasing turbulence for each model in (b, d). The same layout follows for cloud droplet number concentration (N_{CLD}) (e-h).

Figure 4.1: Time series of satellite and radar-based FRP from (a) August Complex (b) Creek Fire and (c) Red Salmon Fire in September of 2020. FRP's shown are from GOES-R ABI Geostationary (green), Doppler radar estimation (purple, dashed) and RAVE (yellow, dotted).

Figure 4.2: (a) Time series of daily mean AOD for MAIAC (red), the reference WRF-Chem run (purple) and Doppler run (blue); (b) scatter plot of daily-mean values from the Doppler run compared to MAIAC AOD. All point values are shown as a daily average for the entire model domain.

Figure 4.3: Maps of simple bias in AOD over the whole domain (a-b) and zoomed in showing CA/NV (c-d). The top row shows values from the reference WRF-Chem run, and bottom shows the Doppler WRF-Chem run, with a strong overall decrease in the largest bias regions.

Figure 4.4: Time series of whole-domain AOD statistics comparing the reference WRF-Chem run and AOD from the MODIS instrument on Aqua, using the MAIAC algorithm. Plots show (a) mean bias against observations; (b) normalized mean bias; (c) Pearson r correlation coefficient; (d) root-mean-squared error; (e) normalized mean error; (f) ratio of modeled to observed AOD value. Horizontal lines are superimposed at the level of unity—a bias of zero, or a ratio of 1 between model and observations.

Figure 4.5: Time series of whole-domain AOD statistics comparing the Doppler WRF-Chem run and AOD from the MODIS instrument on Aqua, using the MAIAC algorithm. Plots show (a) mean bias against observations; (b) normalized mean bias; (c) Pearson r correlation coefficient; (d) root-mean-squared error; (e) normalized mean error; (f) ratio of modeled to observed AOD value. Horizontal lines are superimposed at the level of unity—a bias of zero, or a ratio of 1 between model and observations.

Figure 4.6: Time series (a-b) and scatter plots (c-d) of daily mean AOD for both the reference WRF-Chem run (top) and Doppler run (bottom). Values are shown for only the CA/NV region.

Figure 4.7: Time series (a-b) and scatter plots (c-d) of daily mean AOD for both the reference WRF-Chem run (top) and Doppler run (bottom). Values are shown for only the PNW region.

Figure 4.8: Time series (a-b) and scatter plots (c-d) of daily mean AOD for both the reference WRF-Chem run (top) and Doppler run (bottom). Values are shown for only the IMW region.

Figure A.5: Cloud properties in E3SM and CESM and their sensitivities to various changes in chemical schemes averaged per column in August 2017. (a-f) cloud fraction is a unitless decimal fraction between 0 and 1, and (g-l) cloud droplet number concentration is in cm^{-3}.

List of Tables

observation dataset they're being co-located with (e.g., E3SM – ORA denotes samples from $\mathrm{E3SM_{BASE}}$ co-located with the ORACLES flight tracks, and E3SM – CLR is similar for CLARIFY data). Ranges are shown for ORACLES diameter because multiple instruments provided plausible measurements (UHSAS, LDMA, and PCASP). Note the CLARIFY campaign only provided sizing data from the PCASP instrument.

Acknowledgements

Chapter Two is a version of the following published work:

Howes, C., Saide, P. E., Coe, H., Dobracki, A., Freitag, S., Haywood, J. M., Howell, S. G., Gupta, S., Uin, J., Kacarab, M., Kuang, C., Leung, L. R., Nenes, A., McFarquhar, G. M., Podolske, J., Redemann, J., Sedlacek, A. J., Thornhill, K. L., Wong, J. P. S., Wood, R., Wu, H., Zhang, Y., Zhang, J., and Zuidema, P.: Biomass-burning smoke's properties and its interactions with marine stratocumulus clouds in WRF-CAM5 and southeastern Atlantic field campaigns, Atmos. Chem. Phys., 23, 13911–13940, https://doi.org/10.5194/acp-23-13911-2023, 2023.

In Chapter Two, we acknowledge the contributions of co-authors. CH and PES designed the model–observation comparison. PES acquired the resources to support this research. AN, AD, SF, GMM, HC, JMH, SGH, CK, SG, MK, AN, JR, AJS, KLT, RW, JZ, JU, JP, and PZ provided data from instruments during the ORACLES, LASIC, and CLARIFY observation periods. CK, HW, JMH, JZ, PZ, SF, SG, SGH, and JU assisted with further analysis of observational data. CH led the model and observational data processing for this comparison with scripting assistance from PES. PES and CH ran the model and implemented configuration changes. CK, JPSW, JU, LRL, and YZ provided substantial components of the model configuration. CH wrote the first draft. PS provided major input throughout writing, and AJS, AND, GEM, JR, JZ, LRL, PZ, RW, SF, SG, SGH, and YZ provided further editing and feedback.

Funding, advising support, and computational resources for Chapter Three were provided through the National Center for Atmospheric Research visiting student program and the US Department of Energy Office of Science Graduate Student Research internship program.

In Chapter Three, Pablo Saide served as PI and provided feedback throughout the study design and analysis. Further editorial feedback has come or will come from Paquita Zuidema, Yan Feng, Jens Redemann, Rob Wood, Andrew Gettelman, Mary Barth, Yan Feng, Manish Shrivastava, and Maria Zawadowicz. Mary Barth and Andrew Gettelman provided CESM support and guidance on configuration changes. Wenfu Tang built most of the model configuration and input data used for this study as well as insight on model modifications and interpretation. Yan Feng provided E3SM build and interpretation support. Manish Shrivastava provided E3SM code changes and advice for sensitivity testing. MERRA data processed for E3SM nudging was provided by Shuaiqi Tang and Jerome Fast.

In Chapter Four, Pablo Saide served as PI and provided feedback throughout the study design and analysis. Laura Thapa provided insight on data processing and analytical scripts as well as model fire code changes. Xinxin Ye built the WRF-Chem configuration as well as updating plume rise code. Fangjun Li and Xiaoyang Zhang provide RAVE data and feedback on its application.

Financial support for this work was provided by NASA grants 80NSSC19K1463, 80NSSC18K0629, and 80NSSC20K1650, DOE LASIC grant DE-SC0018272, NSF grants 2013461 and 2238338, and NOAA grant NA18OAR4310107, and funding from The Anthony and Jeanne Pritzker Family Foundation.

Vita

2022	Science Graduate Student Research Program, US Department of Energy, Argonne National Laboratory, Lemont, IL
2022	Visiting Student Researcher, National Center for Atmospheric Research, Boulder, CO
2020	Master of Science in Atmospheric and Oceanic Science, University of California, Los Angeles (UCLA)
2014	Technical Services, Epic Systems Corporation (Epic), Madison, WI
2010	Bachelor of Science, Engineering Physics, University of Colorado, Boulder (CU)

Publications

Howes, C., Saide, P.E., Zuidema, P., Redemann, J., Sedlacek, A.J., Gupta, S., Howell, S.G., Freitag, S., Haywood, J.M., Nenes, A., Podolske, J., Thornhill, K.L, Zuidema, P.: Biomass-burning smoke aging, composition, and cloud interactions in southeastern Atlantic field campaigns, E3SM, and CESM. (*2024, in preparation).*

Howes, C., Saide, P. E., Coe, H., Dobracki, A., Freitag, S., Haywood, J. M., Howell, S. G., Gupta, S., Uin, J., Kacarab, M., Kuang, C., Leung, L. R., Nenes, A., McFarquhar, G. M., Podolske, J., Redemann, J., Sedlacek, A. J., Thornhill, K. L., Wong, J. P. S., Wood, R., Wu, H., Zhang, Y., Zhang, J., and Zuidema, P.: Biomass-burning smoke's properties and its interactions with

marine stratocumulus clouds in WRF-CAM5 and southeastern Atlantic field campaigns, Atmos. Chem. Phys., 23, 13911–13940, https://doi.org/10.5194/acp-23-13911-2023, 2023.

Howes, C. T., X. Wang, J. Deca, and M. Horányi. “Laboratory Investigation of Lunar Surface Electric Potentials in Magnetic Anomaly Regions.” *Geophysical Research Letters* 42, no. 11 (2015): 4280–87. https://doi.org/10.1002/2015GL063943.

Saide, P. E., Krishna, M., Ye, X., Thapa, L. H., Turney, F., Howes, C., and Schmidt, C. C.: Estimating Fire Radiative Power Using Weather Radar Products for Wildfires, Geophys. Res. Lett., 50, e2023GL104824, https://doi.org/10.1029/2023GL104824, 2023.

Lenhardt, E. D., Gao, L., Redemann, J., Xu, F., Burton, S. P., Cairns, B., Chang, I., Ferrare, R. A., Hostetler, C. A., Saide, P. E., Howes, C., Shinozuka, Y., Stamnes, S., Kacarab, M., Dobracki, A., Wong, J., Freitag, S., and Nenes, A.: Use of lidar aerosol extinction and backscatter coefficients to estimate cloud condensation nuclei (CCN) concentrations in the southeast Atlantic, Atmos. Meas. Tech., 16, 2037–2054, https://doi.org/10.5194/amt-16-2037-2023, 2023.

Chapter 1

Introduction

Wildfires and smoke have become one of the predominant symbols of a warming climate in much of the world over the last few decades. Wildfires are flashy, dangerous, expensive, and emit enormous amounts of biomass-burning aerosols (BBA) and gases that are both harmful to humans and can powerfully alter the atmosphere. In the 2019-2020 Australian wildfire outbreak, for example, the single most severe hour of burning emitted 1.4% of the country's entire annual CO_2 budget (Li et al., 2021a). In 2021, in my home state of Colorado, the most expensive wildfire in state history started, spread, and burnt out entirely within only two anomalously-windy days that caused an estimated $USD 2 billion dollars in damages (Phillips, 2022).

Aside from the dramatic power of wildfires, aerosol emissions and interactions broadly represent one of the largest uncertainties in global climate modeling efforts (Bellouin et al., 2019). As fires increase in frequency, severity, financial threat, or all three as the planet continues to warm (Buechi et al., 2021; Burke et al., 2021; Jones et al., 2022; Liu et al., 2010), and as our understanding of air quality and emissions evolves, it becomes increasingly critical to understand phenomena of smoke emissions and evolution in the atmosphere. In this chapter, we review the fundamentals of atmospheric chemical modeling and emissions of biomass-burning aerosols, as well as some key smoke-related processes that underlie the following chapters.

1.1. Smoke Properties and Emissions in Models

Earth-system models (ESMs) operate by inputting the current knowledge of the world-state and allowing the model to evolve that state according to the equations of realistic physical processes, including constraints and boundary conditions. In atmospheric chemistry modeling as applied in this research, input data mostly take the form of meteorological conditions and emissions inventories of aerosols and gases from various sources such as fires or anthropogenic activities. The choice of which emissions inventory to use is not at all trivial, as they are themselves constructed from varied observations and assumptions about unknown or unknowable parameters such as vegetation density and regrowth, fuel moisture, below-cloud burning tendencies, or especially biomass consumption (Li et al., 2022). However, constrained smoke emissions are critical to attain accurate modeling of the smoke impacts on the atmosphere and climate more broadly. The construction of, and uncertainties inherent to, building emissions inventories will be discussed further in section 1.2 and chapter 4 of this work.

Burning biomass directly emits a wide range of particles. These are usually categorized as black carbon, primary and secondary organic aerosols (OA), sulfate, ammonium, nitrate, and metallic salts. These particles are primarily emitted in sizes under 2.5 μm, and the majority by number are predominantly between 40 and 400 nm diameter (Hays et al., 2005; Kalogridis et al., 2018; Keshtkar and Ashbaugh, 2007; Zhang et al., 2011). A large component of smoke is also gases, including semi-volatile organic compounds that are able to condense over time into secondary organic aerosol (SOA) (Gilardoni et al., 2016). These aerosol compounds have a range of hygroscopicity values (κ)—a measure of the aerosol tendency to uptake liquid water—that then impacts the particle’s ability to act as cloud condensation nuclei (CCN) (Petters and Kreidenweis, 2008). The optical properties of BBA are also uncertain and dynamic, depending on factors such as composition, age, transport, radiation wavelength, and cloud processing (Bond and Bergstrom, 2007; Che et al., 2022; Chen and Penner, 2005; Ponczek et al., 2022; Reid et al., 1998; Zhai et al., 2017). In addition, the most realistic mixture state of smoke remains an open research topic in observation and modeling work and leads to significant uncertainty in total radiative effects of smoke (Sedlacek et al., 2022; Zhai et al., 2017).

Most of the smoke properties mentioned above also change over time as the aerosol physical and chemical properties evolve. For example, particles undergo heterogeneous chemistry and photolysis that oxidize OA, changing their density, optical properties, and hygroscopicity (Chang et al., 2010; Dang et al., 2022; Dobracki et al., 2023; Kuwata et al., 2011). Particles also undergo changes in mixing, size, and chemistry when they mix inside cloud droplets and can further be modified by wet and dry scavenging or new particle formation. In total, these forces and others drive large changes in the character and interactions of an aerosol population over long distances. Smoke, as a result, has highly dynamic properties that remain difficult to constrain in modeling projects. Therefore, a major goal of this work is to offer further constraints on smoke properties and evolution in models in order to improve climate projections.

1.2. Biomass-burning Smoke Emissions and Air Quality

Emissions from fires have been shown to correlate with both the radiant energy emitted by combustion, fire radiative power (FRP) and the total burned area (Darmenov et al., 2015; van der Werf et al., 2010; Wooster, 2002). These are respectively referred to as the “bottom-up” and the “top-down” approaches when estimating emissions. FRP is typically measured from satellite radiometers, while burn area is measured from satellite optical imagery (Giglio et al., 2010). Smoke emissions inventories are then built by linearly scaling FRP or burned-area observations with emissions factors based on land cover and fuel type (Andreae, 2019; Wooster, 2002). Uncertainties and differences arise in different emission inventories for various reasons, including differing observational resolution, temporal gaps in data availability, overpass patterns, or assumptions about land cover type and burning dynamics such as fuel moisture. Satellite imagery can also be limited by cloud cover and, for FRP, saturation of a sensor pixel. Different modern emissions inventories themselves span a wide range of total emissions mass (Faulstich et al., 2022), which may then even be magnified in models’ differing ability to represent atmospheric concentrations (Li et al., 2019)

The extremely negative impact of smoke on human health is difficult to understate and is broadly documented (Borchers-Arriagada et al., 2024; Johnston et al., 2021; Matz et al., 2020; Stowell et al., 2019). In the United States alone, smoke particulates account for nearly 1 million disability-adjusted life-years lost annually between 2006-2018, and smoke pollutant levels are expected to keep rising (Burke et al., 2021; O’Dell et al., 2021). Fires emit the great majority of smoke mass in the $PM_{2.5}$ range, which is most harmful to cardiopulmonary health in humans. Fires also emit carbon monoxide (CO) and other volatile organic compounds (VOCs) that are directly toxic. Operational forecasting and early-warning systems exist to mitigate harms to humans, but these too require continuous advances and constraints in model design and emissions (Li et al., 2024).

1.3. Outline of the Thesis

Chapter 2 of this work evaluates the performance of the Weather Research and Forecasting Model with Chemistry (WRF-Chem) with the Community Atmosphere Model version 5 (combined, WRF-CAM5). This model is evaluated—focusing on BBA—against observations from three field campaigns overlapping in the Southeastern Atlantic Ocean (SEA) region in August of 2017. This was during the burning season in southern Africa, which generates enormous annual emissions. We examine a wide range of modeled and observed smoke properties in order to identify biases and better understand key processes impacting smoke and climate in the region. This study covers aerosol size distribution, hygroscopicity, chemical composition, mixing state, new particle formation, CCN ability, and boundary-layer turbulence. Through this work we uncover both critical model biases and important trends in smoke properties as it advects across thousands of kilometers and several weeks.

In chapter 3, we apply similar evaluations from the same field campaigns to two global ESMs, the Energy Exascale Earth System Model (E3SM) version 2 and the Community Earth System Model (CESM) version 2. This study focuses on a few key biases and processes in these models, first identified in the WRF-CAM5 work. First, we assess aging of smoke mean particle diameter and composition due to incorporation of photolytic evaporation of organics in E3SM. Second, we examine the role of oceanic emissions of dimethyl sulfide (DMS) in the formation of boundary layer sulfate aerosol in both models, independently and in combination with the photolysis scheme. Finally, we quantify the sensitivity cloud droplets number to turbulent updraft speed, finding a large model bias compared to observations in both turbulence and cloud properties.

In chapter 4, we discuss results from ongoing work evaluating the potential for Doppler weather radar to update the Regional ABI and VIIRS fire Emissions (RAVE) fire emissions inventory for the western US wildfire season in September 2020. We do this by extrapolating FRP from Doppler data that may be missing or underestimated in the satellite observations underpinning RAVE. These updated emissions are then fed into WRF-Chem to study the impact on air quality modeling skill over the western US. We compare the model with satellite observations of aerosol optical depth (AOD) and ground-level observations of $PM_{2.5}$ and analyze the model improvements. Preliminary results from this work suggest great potential for Doppler radar as a complimentary dataset to constrain and improve fire emissions and, therefore, modeling efforts for both air quality and climate science.

Chapter 2

Biomass-burning smoke properties and its interactions with marine stratocumulus clouds in WRF-CAM5 and southeastern Atlantic field campaigns

An edited version of this paper was published by Copernicus Publications. Copyright (2023) Calvin Howes.

Abstract

A large part of the uncertainty in climate projections comes from uncertain aerosol properties and aerosol-cloud interactions, as well as the difficulty in remotely sensing them. The southeast Atlantic functions as a natural laboratory to study biomass-burning smoke and constrain this uncertainty. We address these gaps by comparing the WRF-CAM5 model to multi-campaign observations (ORACLES, CLARIFY, and LASIC) of the southeastern Atlantic in August 2017 to evaluate a large range of the model's aerosol chemical properties, size distributions, processes, and transport, as well as aerosol-cloud interactions. Overall, while WRF-CAM5 is able to represent smoke properties and transport, some key discrepancies highlight the need for further analysis. Observations of smoke composition show a overall decrease in aerosol mean diameter as smoke ages over 4-12 days, while the model lacks this trend. A decrease in the OA:BC mass ratio and OA:CO suggest the model is missing processes that selectively remove OA from the particle phase, such as photolysis and heterogeneous aerosol chemistry. A large (factor of ~2.5) enhancement in sulfate from the FT to the BL in observations is not present in the model,

pointing to the importance of properly representing secondary sulfate aerosol formation from marine dimethyl sulfide and gaseous SO_2 smoke emissions. The model shows a persistent overprediction of aerosols in the MBL, especially for clean conditions, that multiple pieces of evidence link to weaker aerosol removal in the modeled MBL than reality. This evidence includes several model features, such as not representing observed shifts towards smaller aerosol diameters, inaccurate concentration ratios of carbon monoxide and black carbon, underprediction of heavy rain events, and little evidence of persistent biases in modeled entrainment. Average below-cloud aerosol activation fraction (N_{CLD}/N_{AER}) remains relatively constant in WRF-CAM5 between field campaigns (~0.65), while it decreases substantially in observations from ORACLES (~0.78) to CLARIFY (~0.5), which could be due to the model misrepresentation of clean aerosol conditions. WRF-CAM5 also overshoots an observed upper limit on liquid cloud droplet concentration around N_{CLD}=400-500 cm^{-3} and overpredicts the spread in N_{CLD}. This could be related to the model often drastically overestimating the strength of boundary layer vertical turbulence by up to a factor of 10.We expect these results to motivate similar evaluations of other modeling systems and promote model development to reduce critical uncertainties in climate simulations.

2.1. Introduction

Among the anthropogenic radiative forcers quantified by the IPCC (Intergovernmental Panel on Climate Change), aerosols and their related cloud feedbacks have the largest uncertainty in global net radiative forcing (Bellouin et al., 2020; Boucher et al., 2013; Myhre et al., 2013; Szopa et al., 2021). This is especially true of shallow stratocumulus clouds that top the boundary layer (Schneider et al., 2017).

Southern Africa is one of the largest regional sources of biomass-burning aerosols (BBAs) in the world, driven largely by human activities related to agricultural burning and land clearing annually during the dry season (Andela and Van Der Werf, 2014; Earl et al., 2015). Those emissions form large regional plumes that, depending on meteorological conditions, advect westward and interact with the expansive, bright, semi-permanent stratocumulus cloud deck off the west coast (Adebiyi and Zuidema, 2016; Garstang et al., 1996; Kaufman et al., 2003; Miller et al., 2021; Zhang and Zuidema, 2021). The complexity of aerosols and cloud behavior introduces a large source of uncertainty in aerosol radiative effects over the southeast Atlantic (SEA) (Redemann et al., 2021; Zhang et al., 2016; Zuidema et al., 2016). These radiative effects are a product of both the smoke plume properties and the underlying cloud albedo in the SEA, wherein the latter are also influenced by microphysical aerosol-cloud interactions (Adebiyi and Zuidema, 2018; Bond et al., 2013; Chand et al., 2009; Cochrane et al., 2019; Eck et al., 2013; Kaufman et al., 2003; Leahy et al., 2007; Magi et al., 2008; Waquet et al., 2013) (Cochrane et al., 2019; Eck et al., 2013; Kaufman et al., 2003; Leahy et al., 2007; Magi et al., 2008; Waquet et al., 2013; Chand et al., 2009; Bond et al., 2013; Christensen et al., 2020; Adebiyi and Zuidema, 2018).

Aerosol-cloud interactions in the SEA can drive large regional uncertainty in radiative effects through multiple mechanisms. Absorbing aerosols in this region have been, to varying degrees, connected to changes in cloud albedo, fraction, lifetime, drizzle rate, cloud droplet size and number, and large-scale breakup or persistence (Diamond et al., 2022; Yamaguchi et al., 2015; Zhang and Zuidema, 2019; Zhou et al., 2017) (Christensen et al., 2020; Diamond et al., 2022; Yamaguchi et al., 2015, 2017; Zhang & Zuidema, 2019; Zhou et al., 2017). Therefore, constraint on both smoke representation in models, and especially aerosol-cloud interactions, is crucial to reducing uncertainties in global climate projections.

Campaigns that utilize in situ observation platforms are critical to quantify aerosol-cloud interactions and are less vulnerable to assumptions about aerosol properties or distribution than satellite measurements (Kaufman et al., 2003; Li et al., 2020). Different models generally utilize a wide range of parameter values for aerosol physical and chemical properties such as size distribution parameters, optical properties, hygroscopic water uptake, and density, among others (Che et al., 2021; Gordon et al., 2018; Lou et al., 2020; Lu et al., 2018, 2021; Saide et al., 2020). Additionally, models will often include representation of different aerosol aging and removal processes (Konovalov et al., 2019; Lou et al., 2020; Saide et al., 2012; Yu et al., 2019; Zawadowicz et al., 2020). The wide range of parameters and processes implemented plays a role in the uncertainties of their predictions, both of which can be constrained by field campaign data (Johnson et al., 2018).

Valuable observational constraints on these processes come from three field campaigns in this region overlapping in August 2017. ORACLES (ObseRvations of Aerosols above CLouds and their intEractionS) was a NASA aircraft campaign in 2016-2018 that studied biomass-burning smoke and clouds in the southeast Atlantic using remote sensing and in situ instruments (Redemann et al., 2021). CLARIFY-2017 (CLoud–Aerosol–Radiation Interaction and Forcing: Year 2017, Haywood et al., 2021), was a campaign funded by the UK's Natural Environment Research Council (NERC) centered on the UK's Facility for

Airborne Atmospheric Measurements (FAAM). It was based primarily around Ascension Island (ASI) in the southeastern Atlantic, and was also studying physical, chemical, and radiative effects of biomass-burning smoke in this remote region. Finally, LASIC (Layered Atlantic Smoke Interactions with Clouds, (Zuidema et al., 2018a) was a US Department of Energy campaign that installed Atmospheric Radiation Measurement (ARM) Mobile Facility 1 on ASI to observe the remote marine troposphere in both 2016-2017, covering both years' biomass-burning seasons.

Two recent analyses examined multiple models' performance against observations from ORACLES. First, compared to ORACLES observations in September 2016 (Shinozuka et al., 2020), regional WRF-CAM5 was found to perform well among the study cohort (vs. EAM-E3SM, GEOS-5, GEOS-Chem, and UK Unified Model [UM-UKCA], all global) compared to smoke observations. WRF-CAM5 and GEOS-5 had finer horizontal resolution at ~30km, UM-UKCA was 61km by 92km, EAM-E3SM was 100km, and GEOS-Chem was 2.5° by 2°. All were fed by QFED2 fire emissions except UM-UKCA (FEER fires) and E3SM (GFED fires). All models' aerosol schemes also contained the main fire emissions species of interest (black carbon, and organic aerosol), along with other aerosols such as sea salt, sulfate, and dust. WRF-CAM5 had the smallest error in both free-tropospheric OA and BC mass concentration and spatial distribution, although OA mass still varied widely with a root-mean-square error around 40% in the lower free troposphere (FT). Models in this study also consistently exhibited biases towards a lower smoke layer base in the FT compared to lidar observations, and plume top height differences of generally less than a model vertical grid cell. WRF-CAM5 was also found to overestimate BC in the boundary layer offshore. CO was largely underestimated, especially in the lower FT and further offshore.

WRF-CAM5 was also compared to GEOS-5, CNRM-ALADIN, and UM-UKCA with a focus on aerosol extensive and intensive properties important to the direct aerosol radiative effect (Doherty et al., 2022a). This study used model output covering all three ORACLES deployments, in September 2016, August 2017, and October 2018. QFED2 emissions were used in both WRF-CAM5 and GEOS5, FEER was used in UM-UKCA, and GFED in ALADIN. Doherty et al. (2022) found that WRF-CAM5 had a bias towards low CO compared to observations in the core of the smoke plume (median CO bias -32% to -13%). However, WRF-CAM5 outperformed GEOS5 and UM-UKCA in representing both BC and OA concentrations at 1-3 km above the surface in 2017, which is the focus of this study, with a WRF-CAM5 median bias in BC concentration of -20% to +38%, and median bias in OA concentration -8% to +23% in that year compared to observations. OA and BC in WRF-CAM5 were better represented in the 1-3 km height range compared to GEOS5 in 2016 and 2018 as well, and the WRF-CAM5 bias was similar to or lower than those of UM-UKCA in 2016 and 2017. The OA concentrations in the upper FT in both WRF-CAM5 and GEOS5, especially between 4-6 km altitude, were 2-10 times higher than observations. BC from 4-5 km was low in both models by a factor of 2. UM-UKCA showed biases of the same sign and smaller magnitude for both OA and BC in the 4-6 km range. ALADIN biases of these quantities were not reported. In summary, we expect that WRF-CAM5 captures the plausible ranges of major smoke component concentrations in the year and altitudes studied here, where the largest smoke concentration and transport exist.

The first goal of this work is to analyze the performance of a fully online aerosol-resolving model, WRF-CAM5, in representing biomass-burning smoke processes. The model is compared to a wide range of observations from August 2017, when three field campaigns overlapped: ORACLES, CLARIFY-2017, and LASIC. The second goal is to identify significant processes that may be missing or whose model representations cause substantial discrepancies between modeled and observed properties. Section 2.2 discusses the campaigns and data analyzed as well as the configuration of WRF-CAM5, our sampling methods, and meaningful derived quantities. Section 2.3 compares observations with the model simulated smoke extensive properties such as number and mass concentrations, as well as intensive properties such as size, hygroscopicity, and composition in the FT. We then address observations of changing smoke properties that suggest long-term aging, and that are not captured in the model. Simulated smoke in the marine boundary layer (MBL) is also evaluated, especially utilizing observations from an ARM ground station. We further discuss aerosol composition, size distribution, and hygroscopicity and the representation of smoky and clean periods. Finally, in section 2.4 we analyze model cloud activation and what it may reveal about underlying process biases.

2.2. Methods

Here we evaluate a wide array of observations to understand key physical processes and judge model performance. This approach allows us to understand complex coupled processes over a much larger area than single-campaign studies typically cover. First, we introduce the array of instruments and their related data product from across the three campaigns. Second, we describe the important derived quantities from those instruments, including hygroscopicity, turbulent updrafts, BL height, and BL capping inversion strength. Third, we present notes on data usage and validation between comparable instruments. Fourth, we discuss the model build and configuration used here. Finally, we discuss selection of data points for this analysis, including identifying smoky FT segments and cloud vertical profiles.

2.2.1. Observation systems

Model performance was evaluated by comparing model simulations with extensive in situ and remote sensing data from three field campaigns in the SEA that coincided in August 2017—ORACLES, CLARIFY-2017, and LASIC. The model domain and field campaigns are shown in Figure 2.1. The ORACLES campaign consisted of flights during the biomass-burning seasons in Southern Africa in 2016-2018 utilizing a mid-altitude P3 (2016-2018) and high-altitude ER2 (2016 only). The ORACLES base of operation was Walvis Bay, Namibia in 2016, and São Tomé Island, São Tomé, and Príncipe in 2017 and 2018. ORACLES flew various planned and opportunistic transects throughout the SEA (Redemann et al., 2021). This work uses data exclusively from the August 2017 ORACLES deployment. The CLARIFY-2017 campaign in August-September 2017 flew an instrumented Bae146 FAAM aircraft from ASI in an approximately 5-degree radius around the island to sample smoke and clouds (Haywood et al., 2021). The LASIC campaign studied aerosol, clouds, and their radiation interactions from June 2016 to October 2017, covering two biomass-burning seasons (Zuidema et al., 2016, 2018a). The data at ASI are supplemented by measurements from a permanent weather emplacement on the island, ~5 km away from the LASIC ARM station, operated by the UK Met Office. The selected instruments used in this analysis across all three campaigns are detailed in Table 2.1 and are described in detail in the campaign overview papers and references therein (Barrett et al., 2022; Dobracki et al., 2023; Haywood et al., 2021; Redemann et al., 2021; Taylor et al., 2020; Wu et al., 2020; Zuidema et al., 2018a).

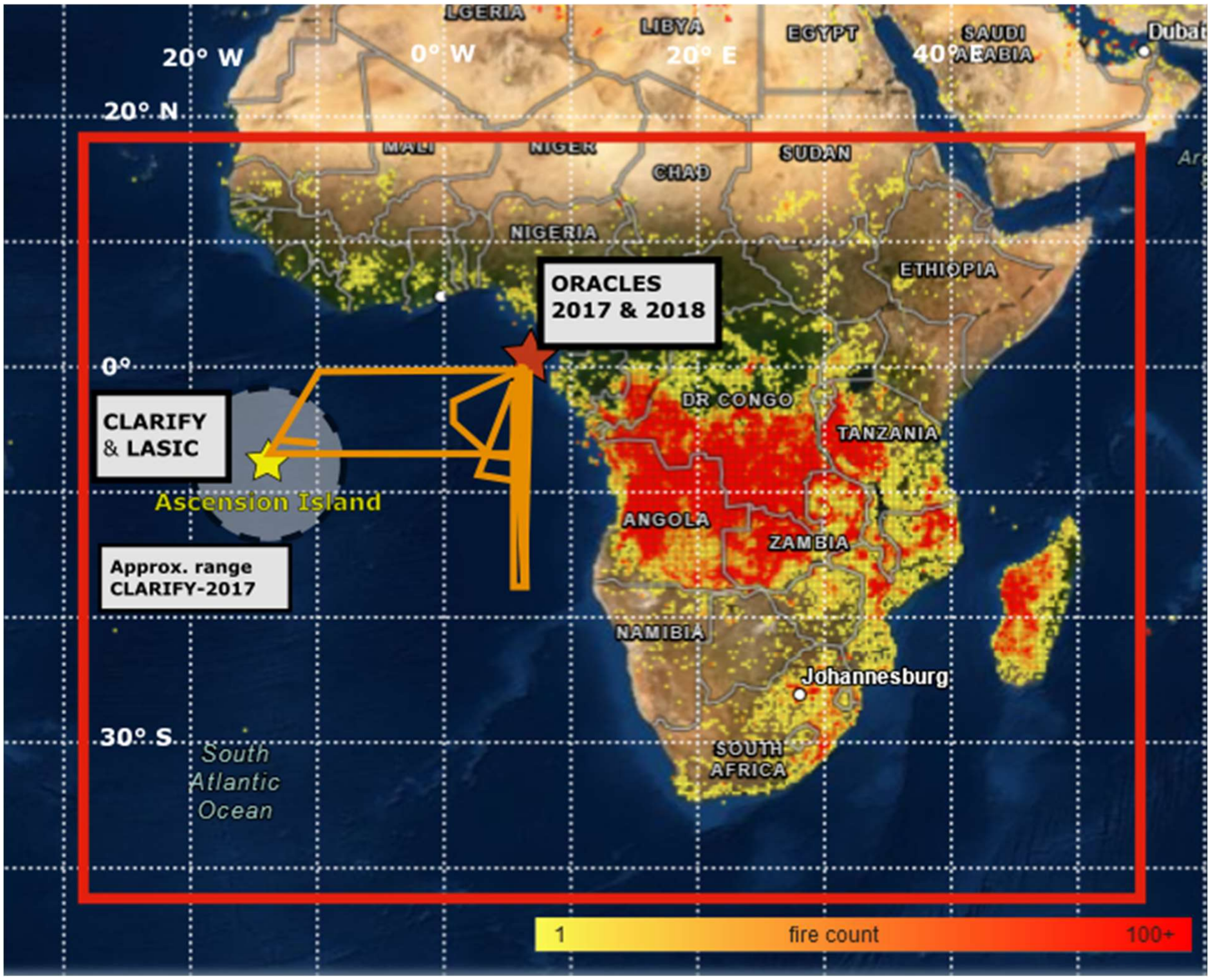

Figure 2.1: Domain of the WRF-CAM5 run for this study (red box) as well as the location of each observational campaign. Orange lines represent the approximate flight tracks of ORACLES 2017 flights. Color points are regridded fire detection counts in August 2017 from VIIRS/S-NPP and map layer obtained from NASA FIRMS.

Table 2.1. Summary of aerosol observations from field campaigns included in this study. Groups providing observations are noted in parenthesis and acronyms correspond to: DoE ARM – US Department of Energy Atmospheric Radiation Measurement; HiGEAR: Hawaii Group for Environmental Aerosol Research; UoM - University of Manchester; FAAM – Facility for Airborne Atmospheric Measurements; GIT – Nenes group at Georgia Institute of Technology; UND - Poellot group at University of North Dakota; BNL – Brookhaven National Lab; LRC - NASA Langley Research Center; UK Met O – UK Met Office. Instrument acronyms correspond to: AMS – High-resolution Time-of-Flight Aerosol Mass Spectrometer; SP2 - Single Particle Soot Photometer; COMA – Carbon mOnoxide Measurement from Ames; VUV – NCAR Vacuum UV fluoromiter; UHSAS - Ultra-High Sensitivity Aerosol Spectrometer; LDMA – Long Differential Mobility Analyzer; SMPS - Scanning Mobility Particle Sizer; PCASP - Passive Cavity Aerosol Spectrometer Probe; CPC – Condensation Particle Counter; CCN - Cloud Condensation Nuclei; TAMMS – P3 Turbulent Air Motion Measurement System; AIMMS – Aircraft Integrated Meteorological Measurement System; CDP – Cloud Droplet Probe.

Observable	**ORACLES**	**CLARIFY / UK Met**	**LASIC** (all instruments operated by DoE ARM)
Mass concentration (submicron, non-refractory)	AMS (HiGEAR)	AMS (UoM)	--
Black carbon mass concentration	SP2 (BNL)	SP2 (UoM)	SP2
Carbon monoxide	COMA (NASA Ames)	VUV (FAAM)	CO ANALYZERs
Aerosol size distribution	UHSAS, LDMA (HiGEAR) UHSAS (GIT), PCASP (UND)	PCASP (FAAM)	SMPS, UHSAS
Total aerosol number concentration	CPC (>3 nm and >10 nm) (HiGEAR)	PCASP (FAAM)	SMPS, CPC, UHSAS
Cloud Condensation Nuclei concentration	CCN (GIT); 0.1%, 0.2%, and 0.3% supersaturation	--	CCN; 0.1%, 0.2%, 1.0% supersaturation
Aerosol hygroscopicity	CCN (GIT), AMS (HiGEAR)	AMS (UoM)	CCN; 0.1%, 0.2%, 1.0% supersaturation
Turbulence	TAMMS (NASA LRC)	AIMMS (UK Met O)	--
Cloud droplet number concentration	CDP (UND)	CDP (FAAM)	--
Ground-based Rain Accumulation	--	Tipping bucket rain gauge (UK Met O)	RAIN non-tipping precipitation gauge

2.2.2. Data processing

Here we outline specific methods of deriving key quantities from observations used to evaluate the model. Single-parameter hygroscopicity is estimated using two independent methods, both of which are widely adopted and described in Petters & Kredenweis (2007). First, we use Aerosol Mass Spectrometer (AMS) chemical mass and assumed density to calculate a simple volume-weighted average hygroscopicity assuming internal mixing. We assume hygroscopicity values and density for each species in AMS/SP2 observations and the corresponding prescribed values in the model, as shown in Table 2.2. Second, we analyze the CCN concentration at 0.1%, 0.2%, and 0.3% in combination with the aerosol size distribution to find the critical dry particle diameter of activation. For a given supersaturation (SS, the relative humidity above 100% where particles begin deliquescing) setting, the number-size distribution is integrated from large bins down to small, and the diameter bin at which the integrated number concentration is first greater than or equal to the CCN concentration is the critical activation diameter D_{crit}. The diameter is used in the approximation formula $\kappa=(24/D_{crit})^3/(SS\%)^2$ (Petters and Kreidenweis, 2007). This equation is based on eq. 10 in Petters & Kreidenweis (2007), takes D_{crit} in nm, substitutes numerical values for the constants suggested, and approximates $\ln(1+SS) \sim SS$, for realistic supersaturation values of 0.1%-1.0%. For ORACLES, we used the GIT UHSAS as it was configured to use the same aerosol sampling line as the CCN, and CCN measurements at 0.1%, 0.2%, and 0.3% SS. UHSAS and CCN data are not used for 15 August 2017, as it was found that CCN counts at 0.3% SS for that day exceeded the UHSAS count, which is not physically realistic. Number concentrations and D_{crit} on the other days are within plausible ranges of count and derived κ. Kacarab et al. (2020) similarly found CCN D_{crit} in the 100-200nm range in ORACLES data, supporting this assessment. For LASIC, we use the SMPS size distribution with the CCN at SS= 0.1%, 0.2%, and 1.0%. To the two UHSAS instruments in ORACLES (GIT and University of Hawaii) and the single UHSAS in LASIC, we apply a size correction based on an observed bias towards under-sizing biomass-burning particles due to their large absorption (Howell et al., 2021).

Vertical turbulence was approximated using vertical wind measurements from a high-resolution anemometer (Morales and Nenes, 2010). This calculation fitted a Gaussian curve to the updraft spectrum integrated over 1024 samples at 20Hz. The characteristic turbulent updraft velocity (m s^{-1}), proportional to the root of turbulent kinetic energy ($TKE^{1/2}$), was taken as 0.79*σ, where σ is the standard deviation of that Gaussian curve. The factor of 0.79 also comes from the derivation in Morales & Nenes (2010). This quantity is also output directly from WRF-CAM5, where it is used with the grid-scale updraft speed to construct a Gaussian updraft spectrum that is then used to calculate activation. Both characteristic updrafts are selected in the vertical range of 100-700m that contained most flat BL flight legs.

Inversion height in observations is calculated using two methods. First, the LASIC ARM value-added product included inversion heights and strengths derived by the Heffter method based on potential temperature gradients (Pesenson, 2003). At ASI, this produced between 3 and 5 height values in each radiosonde dataset. We selected the primary capping inversion height as the one with the largest corresponding inversion strength. The inversion top in WRF-CAM5 was calculated as the local maxima of θ_{es} (effective potential temperature of a saturated parcel) below ~5 km, and within 1 km above the first layer with RH > 85% to denote the boundary layer, as well as the inversion base. We also applied the same algorithm to the raw radiosonde profiles as applied to WRF-CAM5 to account for algorithm performance differences. The ARM data also included similar estimates of PBL depth from the algorithm of Liu and Liang (2010), but didn't report inversion strength so it is not used here. In all methods, inversion strength was calculated at each respective inversion height as a difference in potential temperature θ between inversion base and top.

Two rain gauges were used for LASIC to help account for orographic lifting potentially impacting rain rates at the ARM station (Zuidema et al., 2018b). The ARM station was situated in the more mountainous and elevated eastern half of the island (7.967S, 14.350W). The UK Met Office rain gauge was located at the UK air base and meteorology station approximately 6km to the west, in a relatively flat region of the island (7.967S, 14.4W). Thus, the differences between them are to be expected and are not driven by instrument uncertainty.

2.2.3. Instrument Intercomparison and Selection

To make useful comparisons between models and observations from different field campaigns, we must understand the variability between instruments used in each campaign. To this end, Barrett et al. (2022) compared multiple cloud and aerosol instruments on ORACLES and CLARIFY aircraft as well as the LASIC ARM station and found broadly consistent measurements between similar instruments in each, focusing especially on the joint flight day (18 August 2017) on which both the ORACLES and CLARIFY aircraft flew close together through smoke and clouds near ASI. This comparison showed there was good agreement for BC, aerosol number concentration, and aerosol size distributions. Chemical compositions from the SP2 and ToF-AMS in ORACLES and CLARIFY were also shown by Barrett et al. (Barrett et al., 2022) to be within instrument uncertainty, and within one standard deviation for most species. The ORACLES AMS reported a 40% higher sulfate mass that was not attributable to likely instrument uncertainty or postprocessing. The LASIC Aerosol Chemical Speciation Monitor (ACSM) also measured composition, but resulting OA and SO_4 measurements showed a tendency towards 2-4x lower mass concentrations than either the ORACLES or CLARIFY AMS. Diagnosing the reason for this difference is beyond the scope of this work. For the sake of consistent comparison between instruments without confounding uncertainty, we will focus on the two aircraft-mounted AMS instruments that have been shown to perform similarly.

Additionally, we performed a volume closure assessment between ORACLES mass (AMS) and aerosol size (U. Hawaii UHSAS and PCASP) instruments for measurements in the free-troposphere. WRF-CAM5 prescribes aerosol density per species as shown in Table 2.2, and we assumed values as shown for AMS-measured species. We found well-correlated volume closure with low error between the UHSAS, PCASP and AMS (Fig. A.1). This suggests first that the PCASP, with its higher upper size range around 3 µm, was not capturing aerosols that would have been missed with the UHSAS upper size cutoff of 1 µm. Second, both correlated well with the AMS total volume, given the density assumptions below. This tells us that there was not significant aerosol mass beyond what the AMS was able to capture, such as dust and sea salt. This is also evident in the UHSAS size distributions (see section 2.3.1.1).

Table 2.2. Assumed density and hygroscopicity of aerosol species. In WRF, values are prescribed and used in volume calculations. In AMS, values are taken from literature (Jimenez et al., 2009; Shinozuka et al., 2020; Wu et al., 2020).

	POA	SOA	BC	SO4	NH4	NO3	Chl	Dust
WRF-CAM5 ρ	1.00 g cm^{-3}	1.00 g cm^{-3}	1.70 g cm^{-3}	1.77 g cm^{-3}	N/A	N/A	2.60 g cm^{-3}	1.90 g cm^{-3}
Obs ρ	1.27 g cm^{-3}	N/A	1.77 g cm^{-3}	1.77 g cm^{-3}	1.77 g cm^{-3}	1.77 g cm^{-3}	N/A	N/A
WRF-CAM5 κ	0.10	0.14	1.00E-10	0.507	N/A	N/A	1.16	0.068
Obs κ	0.10	N/A	1.00E-10	0.507	0.5	0.5	1.16	N/A

Chloride mass concentration is not used from the ORACLES AMS data as it provided unrealistically high values in the mid and upper FT. This is consistent with the processing of the public data from the LASIC ACSM and CLARIFY AMS, which have similar issues measuring chloride in biomass smoke. As mentioned above, a volume closure suggests that there is very little chloride by mass in the FT, so we expect little impact on FT smoke properties.

The CLARIFY CCN is not analyzed for this work, as our primary usage of CCN data is to calculate hygroscopicity. PCASP, as the available instrument resolving size distributions in the CLARIFY dataset, has both a lower size resolution and a larger lower-end size cutoff (~100 nm) than the UHSAS that both lead to large uncertainty in deriving κ.

2.2.4. WRF-CAM5 Configuration

This work uses Weather Research and Forecasting with Chemistry (WRF-Chem) model, version 3.4 (Skamarock et al., 2008). We utilize the Community Atmosphere Model (CAM5) aerosol and physics parameterizations (Chen et al., 2015; Ma et al., 2014; Zhang et al.,

2015) which include the Modal Aerosol Module (MAM3) aerosol representation with 3 lognormal size modes (Liu et al., 2012), Fountoukis and Nenes (2005) series cloud droplet activation, Morrison and Gettelman (2008) two-moment cloud microphysics, ice nucleation via Niemand et al. (2012) and Bretherton-Park (UW) boundary layer turbulence scheme (Bretherton and Park, 2009). Note the Fountoukis & Nenes (2005) activation scheme differs from standard CAM5. The aerosol scheme is coupled with gas-phase and aerosol-phase chemistry of the Carbon Bond Mechanism version Z (CBMZ) (Zaveri and Peters, 1999). Natural dust emissions come from the "DustDEAD" emissions algorithm (Zender et al., 2003). This configuration of WRF-CAM5 is used because it resembles the configuration used in global climate models, improvement of which is an extended goal of this research. We also use this model because it contains chemistry, aerosol-cloud feedbacks, and aerosol-radiation feedbacks which are highly relevant for absorbing smoke and aerosol-cloud interactions. The model was configured with a horizontal grid resolution of 36 km with 72 vertical layers at 5hPa spacing, and a domain covering the southern burning region of Africa and the SEA. The National Centers for Environment Prediction-Final (NCEP-FNL) climatology (National Centers for Environmental Prediction, National Weather Service, NOAA, U.S. Department of Commerce, 2000) is used to initialize meteorology and boundary conditions. The anthropogenic emissions and trace gases for this study come from EDGAR-HTAP (Janssens-Maenhout et al., 2012), while fire emissions come from QFED2 (Darmenov et al., 2015). QFED2 is provided at daily time resolution and 0.1° spatial resolution. A superimposed diurnal cycle is applied to resemble real burning trends, such as that applied to an NCAR WRF-Chem build in Ye et al. (2021).

As described in previous work (Diamond et al., 2022), there is no subgrid shallow cumulus scheme enabled as we discovered that it led to significant suppression of the boundary layer height and clouds compared to observations. Also, we use no subgrid scheme for smoke plume injection, and emissions are placed within the 1st model level. This is done as fires in the region tend to be small and the boundary layers over land are deep, so few injections above the boundary layer are expected. This assumption produces reasonable smoke layer heights over the southeast Atlantic (Shinozuka et al., 2020). MAM3 uses 3 predefined lognormal size modes with fixed width and mean diameter at emission, after which the mass and number evolve freely but the width is kept fixed. We also changed emissions to exclude the "other PM2.5" category (i.e., total PM2.5 - OC - BC) in the emissions files. Before our change, this was then added to the accumulation mode aerosol mass in the dust category. With "other PM2.5" classed as dust, the modeled dust concentration in the lower FT was ~8 $\mu g\ m^{-3}$ across ORACLES samples and ~5.5 $\mu g\ m^{-3}$ across CLARIFY samples, or about 30% and 35% of the total accumulation mode mass in those samples, respectively. We consider this dust mass to be unrealistically large when comparing it to observations of low-dust conditions in the FT during ORACLES and CLARIFY. Cloud droplets are activated in the model based on both aerosols at cloud base and further secondary aerosol activation within the cloud.

Following suggestions in recent work (Diamond et al., 2022; Shinozuka et al., 2020) comparing multiple models to ORACLES data, as well as our own calculations in the FT, we adjusted aerosol size parameters of the accumulation mode—applying across all species—to bring the model closer in line with observations. In particular, the geometric mean diameter (i.e., count mean diameter) of the accumulation mode emissions was changed from 110 nm to 150 nm and its standard deviation was changed from 1.8 to 1.5. These changes are consistent with both ORACLES observations and estimates in literature of crop-burning primary emission sizes (Hays et al., 2005; Li et al., 2007; Winijkul et al., 2015; Zhang et al., 2011). The refractive index of organic carbon is set at 1.45 + 0*i*, and that of black carbon is 1.85 + 0.71*i* for optical property calculations.

The model run period starts July 15, 2017, and is run through August 31, 2017. The July portion is discarded as meteorology and emissions spin-up time, but it allows smoke to circulate through the SEA region. Initial aerosol and chemical concentrations come from CAMS (Inness et al., 2019). For the entire run period, the model is reinitialized every five days and runs for seven days at a time, with the first two days used to spin-up the meteorology. The aerosol conditions are carried over from day 5 of the previous seven-day run cycle and the meteorology is reinitialized to NCEP-FNL. This allows aerosols to evolve continuously while meteorology remains relatively close to reanalysis. This setup also allows several days for aerosol-climate feedbacks to manifest, such as smoke heating in the FT, which may substantially alter subsidence and transport (Adebiyi and Zuidema, 2016).

We also uncovered a bug in the diagnostic CCN number calculations within the mixing and activation scheme: the model was not calculating a dynamic mean aerosol diameter based on total mass and number per mode, but instead was using a prescribed value from the MAM aerosol mode definitions. This led to an overestimation of all CCN concentrations in the output, although cloud activation was unaffected as CCN is recalculated separately based on the dynamic particle diameter. This bug was reported to the WRF-Chem development team, who have now released a fix. However, any WRF-Chem builds up to v4.2.1 or model source code obtained before January 15th, 2021, may be affected. This bug may have substantially impacted studies using WRF-Chem that reported on CCN concentrations directly, a not-uncommon practice when reporting on aerosol-cloud interactions. Note that further usage of the term "WRF" or "WRF-CAM5" in this work refers exclusively to the configuration described here.

2.2.5. Analytical Methods

In the FT, our goal was to select smoky periods during relatively level flight legs. We focus on periods of uniform smoke behavior in the FT in particular to eliminate background aerosol signals and reduce in-sample variability. We therefore selected 8-minute segments from 1-minute-merged data that contiguously met the threshold criteria for altitude and smokiness. This 8-minute time interval represents roughly 55-100 km of aircraft travel, which in a straight line would pass through 2 model grid cells on average and was chosen to smooth the observational variability. In ORACLES, we selected data for aircraft height > 1200m, RH < 80%, and CO concentration > 120 ppb. We also limited samples to those segments with average total aerosol mass concentrations > 5 μg m^{-3} and BC > 100 ng m^{-3}. This is similar to the Shinozuka et al. (2020) threshold of BC > 100 ng m^{-3} to identify smoke plumes and we incorporate AMS data availability as a key requirement for our analysis. In CLARIFY, we selected for the same height and RH, CO > 100 ppb, total aerosol mass > 1 μg m^{-3}, and BC > 50 ng m^{-3} to account for further plume dispersion over long distances. In both campaigns we selected flight legs with minimal altitude changes (less than 100m over the sample period) to avoid sampling vertically-stratified distinct smoke layers. We then extracted comparable observations and colocated model quantities for each variable of interest.

We treat the MBL as generally well-mixed for the purposes of smoke comparison. Boundary layer segments were selected in ORACLES by a threshold of altitude Z < 1000m, RH < 95%, and BC concentration > 100 ng m^{-3}. Boundary layer segments were selected in CLARIFY by z < 1200 m, RH < 95%, and CO > 100 ppb. These thresholds were used to maximize data availability and consistency and avoid sampling within clouds. The higher altitude threshold in CLARIFY is to allow more data samples with the typically deeper and decoupled boundary layer near ASI, and the usage of a CO threshold rather than BC for smokiness in CLARIFY is a compromise considering data availability from the SP2.

A different modeling system was used to estimate smoke age, using the WRF Aerosol Aware Microphysics (WRF-AAM) configuration that was used regularly and reliably to forecast smoke transport throughout the ORACLES campaign (Redemann et al., 2021) and as such, we expect it to provide a reasonable estimate of the observed smoke age. To estimate smoke age, biomass burning tracers tracking each day of emissions over the whole African continent were added to WRF-AAM. The concentration of the tracer from each day was used to calculate a weighted average of the emission day at a given point in space and time, thus giving an estimate for the average age of that plume. The age extracted from WRF-AAM is used as an age estimate for WRF-CAM5 and the observations. Given differences in transport between all three of WRF-AAM, WRF-CAM5, and reality, the WRF-AAM age estimation method does not provide a perfectly Lagrangian age estimate following the plume itself. However, it still gives insight into bulk property changes in the smoke over time.

Clouds are analyzed by comparing the vertical profile of droplet number concentration (CDNC or N_C) to below-cloud aerosol concentration. Cloud droplet data points are based on averaging 1-second resolution CDP data as the P-3 and Bae146 FAAM aircraft profiled a cloud layer. These passes occurred over a relatively short horizontal distance (approx. 3 km) relative to the size of stratocumulus cloud decks, thus they are treated as vertical cloud profiles. When sawtooths were flown (diving up and down through a cloud layer multiple times in close succession), the profile-mean values from each single cloud profile were then averaged together. The selection of cloud profiles from the ORACLES datasets followed the same criteria as Gupta et al. (2021) and CLARIFY cloud selection used similar methods. Following the methods of Diamond et al. (Diamond et al., 2018), we report droplet-mass-weighted N_C recorded by the same probe. This de-emphasizes regions of extremely thin clouds and emphasizes regions with high liquid water.

For WRF, we calculate below-cloud aerosol by averaging across the two grid cells immediately below the cloud base, which were defined by a weighted droplet concentration threshold of 0.1 cm^{-3}. For observations, the below-cloud aerosol was calculated as an average over the roughly 100 m sampled below the cloud base. To account for differences in vertical placement of clouds and MBL heights in the model vs. observations, all model cells below 3 km with weighted N_C above the 0.1 cm^{-3} threshold were considered regardless of vertical structure. The model grid cells were co-located using the average latitude and longitude of the transect.

2.3. Results

Here we present the findings of our model-observation comparison, commenting on both direct performance and indications of missing or inadequate smoke- and cloud-related processes in the model. We analyze first the free troposphere, and then the boundary layer. These regions are meaningfully distinct in many ways. For example, the free troposphere has very low background aerosol generation, minimal precipitation during this study, and strong winds driving advection with limited vertical mixing. Thus, smoke is primarily driven from the continent in the free troposphere before entraining into the MBL. In the boundary layer, on the other hand, smoke is subject to strong turbulent mixing, cloud processing and deposition, and the ocean as a very strong source of sea spray aerosols and sulfate precursor gases. Aerosol behavior in both regions is important to constrain overall smoke and cloud evolution, but they must each be considered in their own context.

2.3.1. Free Troposphere

The free troposphere is where biomass-burning smoke in the SEA advects the furthest, and with the least disturbance from clouds and other aerosol formation processes. We evaluate it first, both to understand WRF-CAM5 performance in representing BBA as it exists and evolves on its own, and as a prerequisite to interpret aerosol properties and processes when the smoke has mixed with background aerosols and clouds. This section will first analyze representation of total smoke amount and size, moving on to composition, and then hygroscopicity. Finally, we evaluate evidence of significant chemical aging in smoke on timescales of several days, especially through losses of OA.

2.3.1.1. Smoke concentrations and size distributions

The FT is the logical starting point to evaluate model representation of biomass-burning smoke aerosols. In August and September, the smoke from the continent travels throughout most of the southeast Atlantic (SEA) region in the FT, with occasional entrainment into the boundary layer (Diamond et al., 2018). As a result, the lower FT (cloud-top up to roughly 3km) has a much higher and more consistent concentration of smoke than the boundary layer. Additionally, the boundary layer is itself a source of new aerosol particles that confound the smoke signal—primarily sulfates, salts, and organic particles from sea spray (Meskhidze et al., 2013; Zorn et al., 2008). The capping inversion frequently keeps this aerosol population from mixing heavily into the FT, and so it can constitute a large fraction of the BL aerosol mass even in smoky conditions.

Our analytical framework here supports and expands earlier conclusions about WRF-CAM5 performance. We find that the model FT accumulation-mode mean number concentration is biased high by 28% compared to ORACLES observations (Fig. 2.2a) and by 38% compared to CLARIFY (Fig. 2.2b). WRF-CAM5 volume concentration is comparable to ORACLES (Fig. 2.2c, WRF-CAM5 mean bias=+36% vs. UHSAS, -16% vs. PCASP) and relatively high compared to CLARIFY (Fig. 2.2d, WRF-CAM5 mean bias=+111% vs. PCASP). Total aerosol mass concentration simulated by WRF-CAM5 has a mean bias of -10% compared to ORACLES and +108% compared to CLARIFY (Fig. 2.2e-f), tracking the trend in volume. These larger relative discrepancies with CLARIFY may be explained by a lack of mass loss through aging in WRF-CAM5 or insufficient scavenging, which will be discussed later. WRF-CAM5 underestimates CO in the FT by 31% compared to ORACLES and 32% compared to CLARIFY (Fig. 2.2g-h).

WRF-CAM5 represents the range of geometric mean diameters well and is closest to the U. Hawaii UHSAS (Fig. 2.3a). The 25th-75th percentiles of samples of geometric mean diameter are as follows: WRF, 186-208 nm; UHSAS, 176-196 nm; PCASP, 220-244 nm; LDMA, 208-231 nm. The model lognormal distribution also closely follows the spread and mean of observations on a representative sampling day (24 Aug 2017), despite a bias towards high model number (Figs. 2.3b-c). The variability between instruments is not unexpected and we conclude that, after observationally-constraining smoke aerosol size at the point of emission, WRF-CAM5 can successfully represent the mean particle diameters after transport to the SEA to within instrument uncertainty.

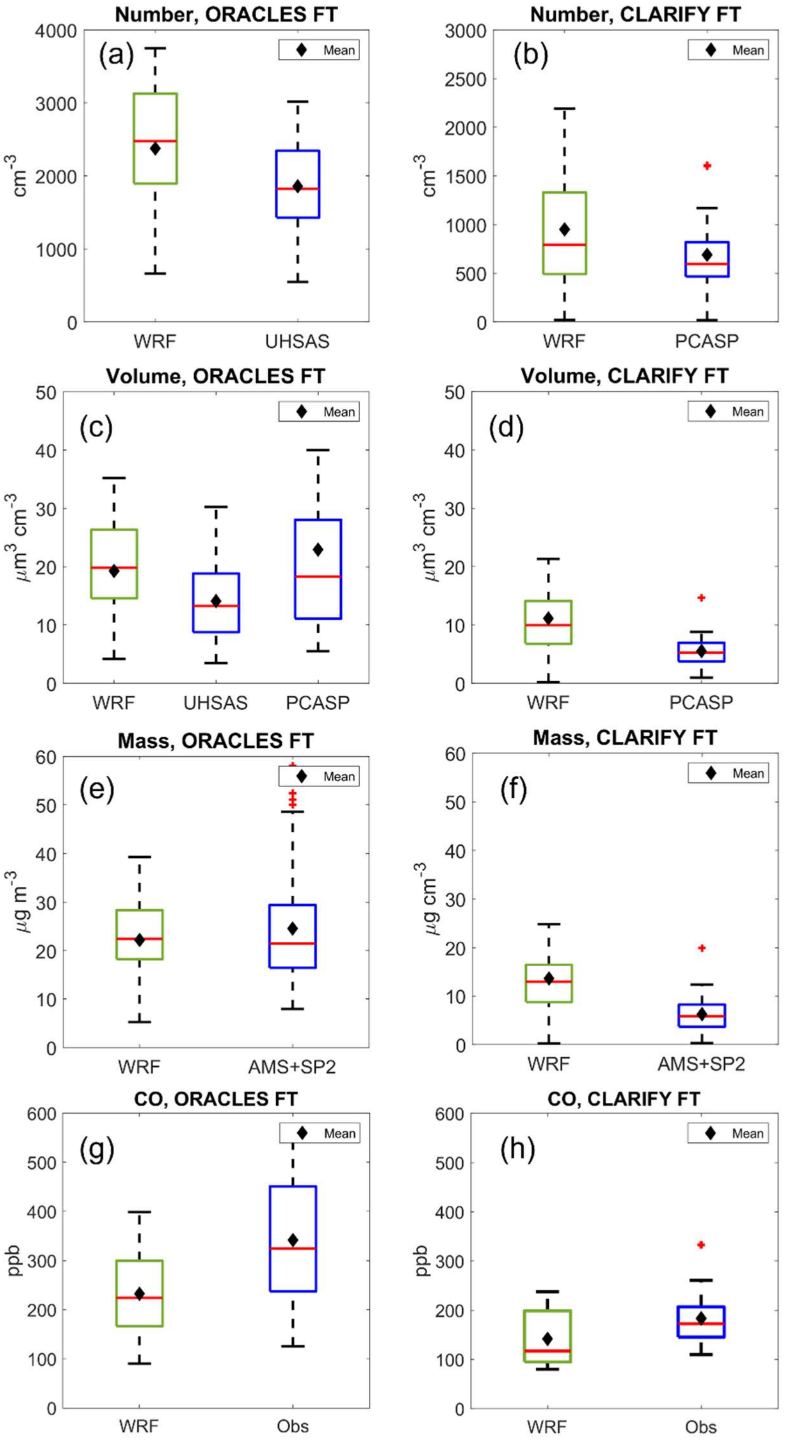

Figure 2.2: Extensive properties of smoke in the free troposphere (FT), comparing WRF-CAM5 and appropriate instruments from both ORACLES and CLARIFY in 2017. Red line represents sample median, black diamond represents mean, and small red crosses are outliers (greater than 1.5 times the interquartile range beyond the box). a-b) Number concentration; c-d) Volume concentration; e-f) Mass concentration, compared to combined AMS and SP2 mass measurements; g-h) CO concentration.

Two other important features are visible in the number and volume distributions of free-tropospheric smoke from ORACLES. In the number size distributions (Fig. 2.3b), there is a dominant accumulation mode (50-440 nm in WRF-CAM5) and extremely small number concentration of coarse mode (>1 μm) or Aitken mode (<40 nm) particles. This holds across >90% of smoky ORACLES samples in the FT on other days (not shown). The lack of coarse mode is supported by the volume size distribution from PCASP, (Fig. 2.3c, green) showing that in the great majority (~95%) of our ORACLES cases there is not a substantial volume of coarse particles such as mineral dust or sea spray. The volume closure between the AMS, PCASP, and UHSAS supports this. The smoke sampled here is days old, and any new particle formation that would generate an Aitken mode was likely in the past near the source in Africa. The LDMA, with its lower size range of around 10 nm, supports this notion.

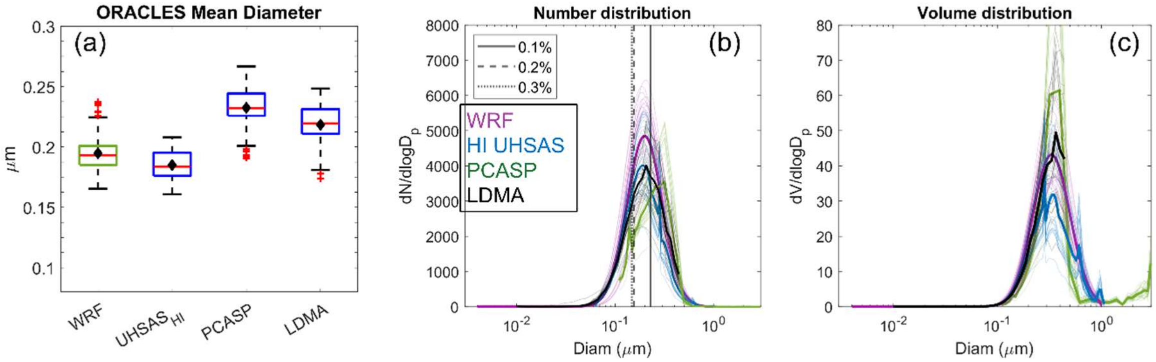

Figure 2.3: Size properties in the free troposphere, from both WRF-CAM5 and ORACLES instruments. CLARIFY data is excluded here for lack of available instruments with a comparable size range. a) Geometric mean diameter across all FT samples deemed smoky and flat enough. Figure features are defined in the caption for Fig. 2. B-c) Number and volume size distributions of same instruments from 31 Aug 2017, showing both WRF-CAM5 nucleation and accumulation mode. Mean distribution from each data source is represented with a thicker line, with each underlying distribution as a thinner curve. Superimposed on fig. 3b are the calculated D_{crit} based on the CCN and GIT UHSAS at the three primary supersaturation settings.

2.3.1.2. Chemical Composition and Hygroscopicity

The average composition fractions across the FT samples in ORACLES and CLARIFY are shown in Fig. 2.4. The mass fraction of OA, by far the dominant chemical species, is well-captured in the FT across campaigns (Figs. 2.4b-c, h-i). Mass fractions of BC and SO_4 are also comparable in the FT. As noted above, AMS analysis does not include chloride salts or mineral dust, but these are likely a very small component of FT aerosols regardless. WRF-CAM5 also lacks aerosol nitrate and ammonia in its implementation of MAM3. WRF-CAM5 also treats aerosol modes as internally mixed, similar to calculations based on the AMS.

The single-parameter hygroscopicity factor κ is biased low in the FT against AMS (-0.042 bias in ORACLES, -0.059 in CLARIFY) and against CCN (-0.046 bias in ORACLES) (Figs. 2.4a, g). When excluding dust and chloride to match the AMS, model bias tends to improve against observations in the FT (median +0.075 in ORACLES and +0.011 in CLARIFY). The CCN and UHSAS from ORACLES had irregular availability and discontinuous SS% sampling in the BL compared to the FT and are unable to be separated by SS% as done in the FT. Thus, MBL κ calculations based on CCN are not included in this comparison.

We suggest a few potential explanations for the low model κ bias. First, in our configuration WRF-CAM5 lacks nitrate or ammonia aerosols, both of which increase the bulk hygroscopicity since κ_{NO3} and κ_{NH4} are both roughly assumed to be 0.5. Second, WRF-CAM5 retains around 10% of total aerosol mass as dust, which in the model has very low

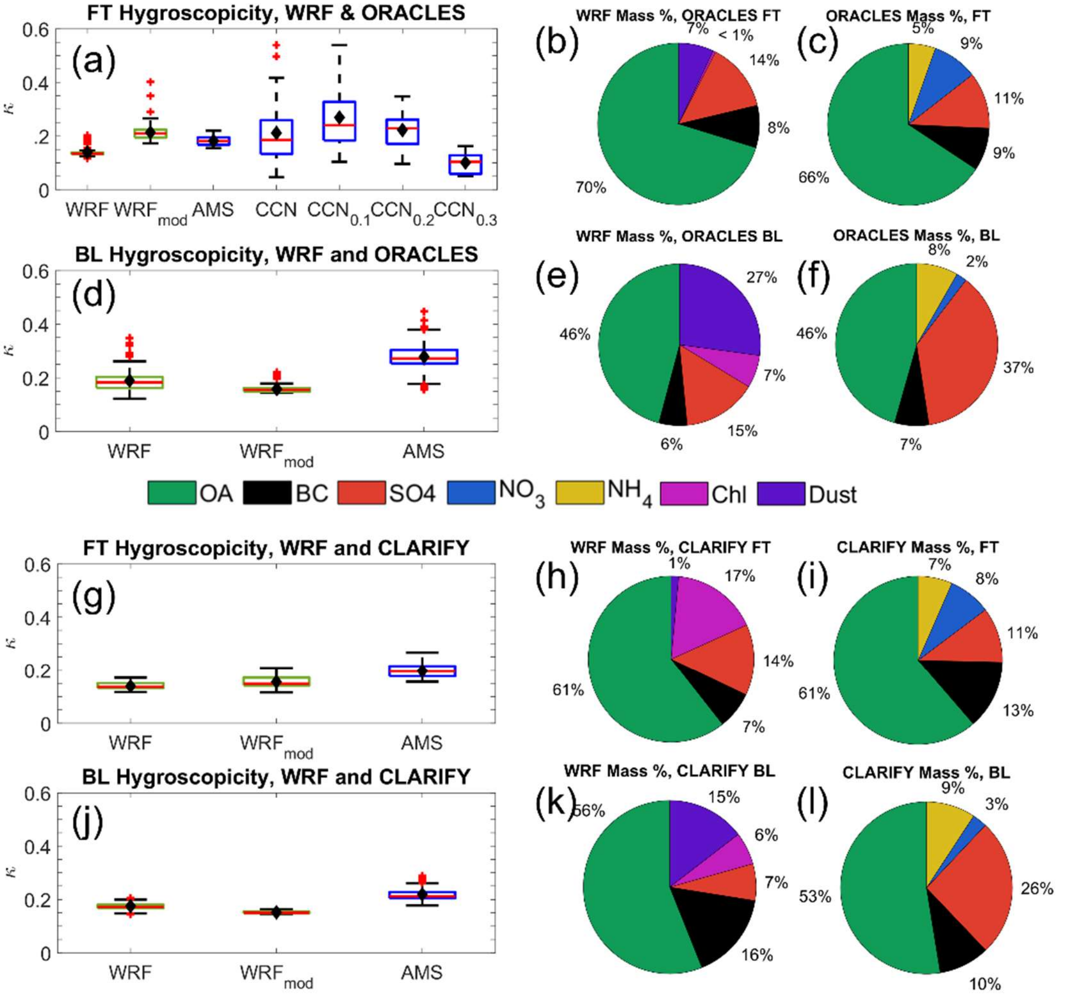

Figure 2.4: Hygroscopicity and the corresponding properties of smoke in the FT+BL between model and observations. (a) Hygroscopicity from WRF-CAM5 (green), first with all species then excluding dust and chloride to match AMS ('mod' subscript), AMS-based, and data from the Nenes group, grouped and then disambiguated by CCN supersaturation setting. Calculations were made with the CCN and GIT UHSAS together; (d, g, f) Hygroscopicity from WRF-CAM5 and AMS for each campaign and atmosphere level. (b, c, e, f, h, i, k, l) average composition by mass fraction of smoke in ORACLES and CLARIFY FT and BL, and colocated WRF-CAM5 samples. Model OA here includes secondary OA, a distinct model variable. WRF-CAM5 SOA was generally less than 3% of total mass.

hygroscopicity at 0.068. This dust comes from the natural dust emission scheme and is not related to fire emissions. Third, the prescribed properties for OA in the model may not be physically accurate. WRF-CAM5 uses a prescribed κ_{OA}=0.1 and density of 1.0 g cm^{-3}. The set density of 1.0 g c m^{-3} for OA in WRF-CAM5 is low compared to both lab studies (Kuwata et al., 2011) and campaign-wide assumptions used in other studies, such as 1.27 g c m^{-3} (Wu et al., 2020). An erroneously low model density leads to a larger volume, which decreases κ since it is a volume-weighted mass average. An OA density of 1.27 g m^{-3} also produces the best volume agreement between the ORACLES AMS, UHSAS, and PCASP. Existing literature measuring the density of biomass-burning aerosol (BBA) organics over long aging periods is generally limited, but there is evidence that OA density is increased by at least 30%--and up to 90%--over the course of a few days (Dinar et al., 2006; Kuwata et al., 2011). K_{OA} may realistically have values ranging from 0 to 0.2, with nonlinear dependence on age and oxidation level (Duplissy et al., 2011; Kacarab et al., 2020; Kuang et al., 2020; Wonaschütz et al., 2013).

WRF-CAM5 and AMS show a similarly narrow range in κ, despite the bias in mean. This indicates that the average bulk composition fractions of observed BBAs vary little, as far as the AMS is capable of measuring. The hygroscopicity based on CCN shows a notably large spread, however. This is partially a result of convoluted instrument uncertainties (combining CCN and UHSAS instrument variability) and partially a result of the κ estimation strategy. The AMS measures bulk chemical mass while the κ based on UHSAS + CCN critical diameter (D_{crit}) depends upon the properties of the aerosol population around that size. At 0.1% CCN SS, D_{crit} fell in the range of 100-250 nm, near the middle of the accumulation mode in most cases. At 0.2% and 0.3%, D_{crit} was in the range of 60-180 nm, with D_{crit} at 0.3% ~10nm lower on average than at 0.2%. Values of κ tend to be higher at 0.1% SS (mean κ=0.27) than at 0.2% (mean κ=0.22) and at 0.3% (mean κ=0.10). As larger particles were less likely to contain rBC or a lower rBC mass fraction in ORACLES (Dobracki et al., 2023; Sedlacek et al., 2022), this may reflect a composition dominated by more hydrophilic species such as sulfuric acid. This variability overall supports existing findings that the accumulation mode is at least partially externally mixed, especially at lower sizes (Dahlkötter et al., 2014; Denjean et al., 2020; Dobracki et al., 2023; Sedlacek et al., 2022; Taylor et al., 2020), which results in measurable differences in hygroscopicity. Imagery of ORACLES and CLARIFY particles also suggests that large BB particles very often mix with hygroscopic salts (Dang et al., 2022). This will be supported further by examining hygroscopicity using LASIC data in section 2.3.2.3. The internal mixing assumption in WRF-CAM5 renders it unable to capture these observed features.

2.3.1.3. Aging Processes

Biomass-burning aerosols emitted in Southern Africa take roughly 4-14 days to be advected to the remote marine FT, leading to optically thick smoke layers reaching as far west as ASI and beyond (Chand et al., 2009; Zuidema et al., 2016). Over time, particles may undergo drastic physical and chemical changes such as heterogeneous oxidation, fragmentation, coagulation, and photolysis—impacting mass, density, optical properties, or hygroscopicity (Che et al., 2021; Dang et al., 2022; Dinar et al., 2006; Dobracki et al., 2023). There is consistent observational evidence for a loss of organics with increasing smoke age and oxidation markers in ORACLES and CLARIFY observations (Che et al., 2022; Dang et al., 2022; Dobracki et al., 2023). Lab studies have suggested that, on the ~3-14 day timescales relevant to these observations, this loss may be caused by heterogeneous oxidation—especially fragmentation—that functions to re-volatilize and evaporate organics (Che et al., 2021; Kroll et al., 2009; O'Brien and Kroll, 2019). This configuration of WRF-CAM5 forms SOA by predefined conversion factors applied to various organic gases such as isoprene and xylene. The density and hygroscopicity of each separate aerosol chemical species involved is constant.

The aerosol size distribution also evolves through new particle formation, coagulation, and evaporation. Here, we analyze the evidence of some aging processes in ORACLES observations and their representation, or lack thereof, in WRF-CAM5.

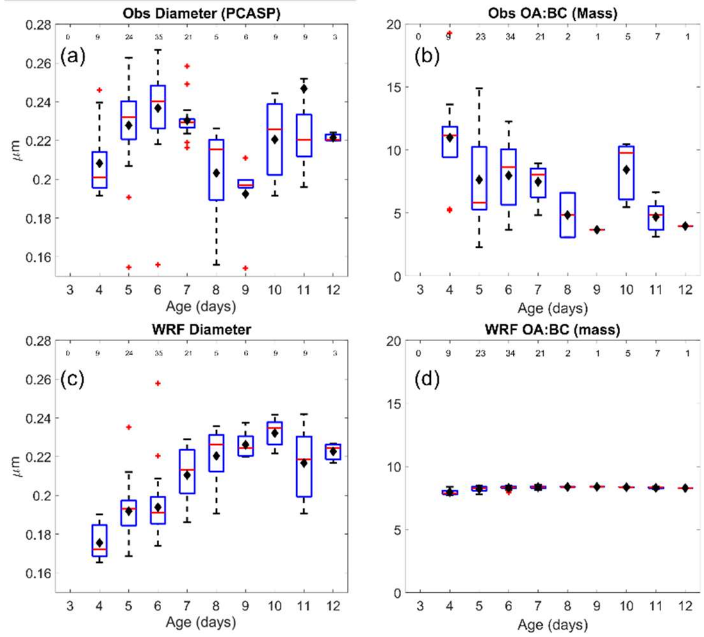

Figure 2.5: Aging trends in FT for mean diameter (a, c) and OA:BC mass ratio (b, d). Sample sizes for each box-whisker are listed at top of each figure. Observational data are filtered for total aerosol mass>10 μg m^{-3} and rBC mass>0.1μg m^{-3}, and same subset is then sampled in WRF-CAM5. Black diamonds represent mean, red lines represent median.

Mean particle diameter is a useful indicator of both particle evolution and CCN activity (Kuang et al., 2020). Mean diameter calculated using ORACLES and CLARIFY PCASP instruments shows a non-monotonic change with age, with a general trend towards growth over the 4-6 day range, and then a flattening or decreasing diameter thereafter (Fig. 2.5a). The PCASP is used here because it was the only available sizing instrument across both ORACLES and CLARIFY campaigns and therefore illuminates longer-term trends than ORACLES alone. The trend of mean diameter growth in the first ~3-7 days is also captured by the ORACLES LDMA and UHSAS (Fig. A.2). However, as ORACLES has very few samples aged beyond ~7 days, the flattening or decreasing diameter trend cannot be corroborated by the more highly size-resolved instruments here. WRF-CAM5 shows an overall positive trend (Fig. 2.5c)—the mean diameter grows steadily from approximately 185 nm to 230 nm between 4 and 12 days. This is expected as the model lacks a mechanism to lose OA particle mass over time, while particles can grow through coagulation and secondary aerosol condensation. There is no evidence of wet scavenging in the FT—either in the model or observations—that might otherwise allow new-particle formation to assert itself in a previously smoky FT air parcel.

Additionally, observations show a noisy downward trend in the OA:BC mass ratio over time (Fig. 2.5b), while in the model the ratio is nearly completely flat (Fig. 2.5d) which implies negligible SOA formation in the model. Further, the mass ratio of OA:CO decreases by 54% between ORACLES and CLARIFY FT samples, but only decreases by 30% in WRF-CAM5 (not shown). This decrease is to be expected as the smoke dilutes and approaches the background CO concentration in the region, roughly ~60ppb measured during clean periods at ASI in Aug 2017 (Pennypacker et al., 2020). In contrast, BC:CO decreases very similarly in both observations and the model (14% and 17% decrease respectively). Taken together, OA is likely selectively lost over time in a way that the model does not represent. Quantification of this loss rate and specific causal mechanisms, such as fragmentation or photolysis, have been explored in other field, modeling, and lab studies (Che et al., 2021; Dobracki et al., 2023; Konovalov et al., 2019; Lou et al., 2020; O'Brien and Kroll, 2019;

Sedlacek et al., 2022) and could be implemented and tested in the SEA and compared to these observations to assess improvements and impacts.

2.3.2. Marine Boundary Layer

The MBL in the SEA region presents new observational and modeling challenges that are not present in the FT. The MBL represents a new source of primary and secondary aerosols, in the form of sea spray and dimethyl sulfide (DMS) emissions. Smoke is entrained into the MBL at sporadic spatial and temporal scales and is removed by precipitation in similarly irregular ways that complicate 1:1 comparison (Diamond et al., 2018). The MBL has convective turbulence that leads to stratocumulus formation at the capping inversion, and the MBL close to ASI can transition to being frequently thermodynamically decoupled between the surface layer and cloudy layer (Zhang and Zuidema, 2019). All these processes can have strong impacts on the composition and size distribution of aerosols and change how they may interact with clouds.

This section focuses primarily on the LASIC campaign. First, it is worth noting some substantial differences between LASIC observations and the airborne ones used so far (ORACLES and CLARIFY). The LASIC campaign's static nature on ASI means its observations are subject to the whims of meteorology and cannot seek out smoke parcels, as aircraft can. Smoke also only reaches ASI when it has been entrained—either locally or upwind—into the BL.

Second, as ASI is approximately 3,000 km west of Angola, smoke is substantially more aged and diluted in both CLARIFY and LASIC data than the smoke measured during ORACLES. For the purposes of this work, LASIC analysis will be limited to August 2017 since that is when it overlapped with both ORACLES and CLARIFY. It is also worth noting that at 36 km resolution, WRF-CAM5 treated the cells containing ASI as ocean uniformly and so the model includes no meteorological features related to land or topography.

Figures 2.6a-e show the time series of smoke properties and rain at ground level at ASI. We have identified and labeled periods considered smoky, medium, and clean for the sake of separating smoke properties during this month by regime, based upon tercile concentrations of black carbon similar to Zhang & Zuidema (2019). This section compares WRF-CAM5 modeled properties to observations of the BL aerosol properties, size distribution, hygroscopicity, and mixing state, and concludes with an analysis of boundary layer dynamics and rain in observations and WRF-CAM5 ASI through the month.

We first analyze the physical properties of smoke measured in the BL, especially as its size distribution and hygroscopicity vary under different smoke loading conditions. We then discuss model trends in smoke entrainment and wet scavenging at ASI. Finally, we evaluate the aerosol-cloud activation tendencies in BL aircraft measurement and WRF-CAM5, as well as the TKE captured in both.

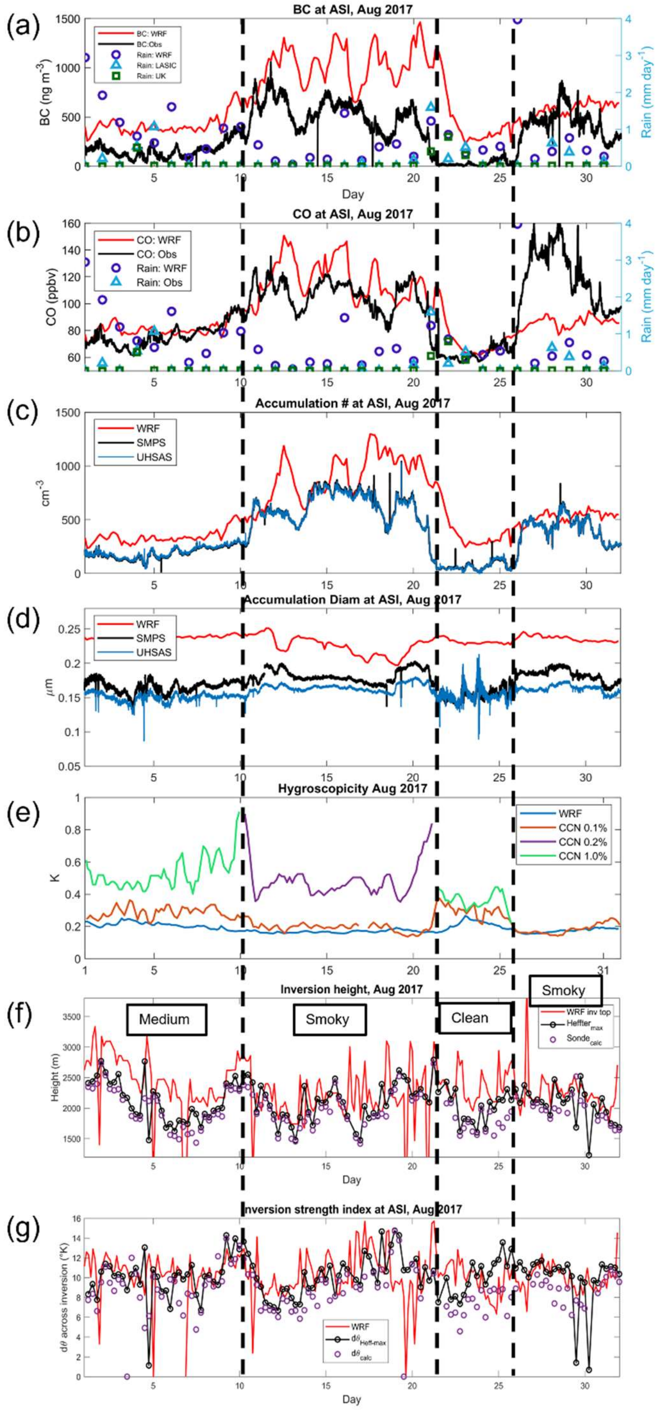

Figure 2.6: Time series of smoke properties at ASI in August 2017. Vertical dashed lines delineate periods of smoky, medium, and clean conditions. a-b) refractory BC and CO concentration, respectively. Overlaid on both are rainfall accumulation from WRF-CAM5, LASIC, and UK Met devices summed on each day; c) Accumulation mode number concentration; d) Accumulation mode geometric mean diameter; e) Hygroscopicity from the CCN and SMPS from LASIC, and bulk composition in the accumulation mode in WRF-CAM5; f) PBL inversion height from WRF-CAM5, from the LASIC radiosonde VAP, and recalculated from radiosonde matching the algorithm applied to WRF-CAM5; g) inversion strength from WRF, from the LASIC radiosonde VAP, and recalculated from radiosonde profiles using the same algorithm as applied to WRF-CAM5.

2.3.2.1. Smoke Concentrations and Size Distributions

While WRF-CAM5 shows reasonable representation of FT mean diameters of smoke aerosols, it broadly overestimates the mean diameter of smoke at ASI (WRF: ~200-240 nm; LASIC: 150-190 nm; WRF-CAM5 mean bias of +35% vs. SMPS and +47% vs. UHSAS, Fig. 6d). This is likely due to a lack of particle losses from multiple sources. First, there are potential chemical losses in single particles (see section 2.3.1.2). Second, there may be a shrinking mean diameter of the aerosol size distribution following aerosol activation into cloud droplets and wet scavenging, in which larger particles are activated and collected more easily. This process leads to a 10% decrease in diameter near ASI at the end of August 2017 (Wu et al., 2020) and heavy precipitation has been observed in northern continental America to potentially be very efficient at removing large smoke particles (Taylor et al., 2014). These occur over long distances, as particles in WRF-CAM5 continue to coagulate and grow.

The accumulation-mode number concentrations are overpredicted in WRF-CAM5 by 60% on average (Fig. 6c), excluding the clean period, and by over 1,000% during the clean period. The bias is the lowest during the smokiest period, with a median bias of 45% and interquartile range of 14-80%. The overestimation bias is far larger during the clean period, over 1,000%. Some of the bias is attributable to the number concentration bias in the FT, as this smoke with high N_{AER} entrains into the BL (WRF-CAM5 bias above ORACLES and CLARIFY by ~28-38%), and the remainder may be explained by either over-entrainment or removal issues, as discussed below.

The observed number size distribution shows a consistent accumulation mode centered around 180 nm through both smoky and medium periods (Figs. 2.7a-c) that corresponds to the smoke transferred from the FT (Fig. 2.3b). During clean periods, observations show a dominant Aitken mode with a mean diameter of 30-50 nm (Fig. 2.7c), which remains comparable in number to the Aitken mode during medium loading conditions and is almost nonexistent during smoky periods. As the smoky FT showed nearly no Aitken mode, the BL particles below ~40 nm are likely coming from new particle formation driven by marine or smoke SO_2 precursors during clean conditions (Zheng et al., 2021). We hypothesize that the observed Aitken mode particles observed during clean conditions are gradually lost through either coagulation with the accumulation-mode smoke after it entrains or through cloud processing that combines the Aitken and accumulation modes. This could explain why the Aitken mode is present for clean and medium-level smoke but not observed for smoky conditions. In WRF-CAM5, the Aitken mode tends to be very small in number and broader than observations. This could be due to new particle formation in the model being suppressed by the constant presence of smoke, but also due to potential inability of models to properly represent new particle formation in pristine marine conditions as found by previous work (Tang et al., 2022a).

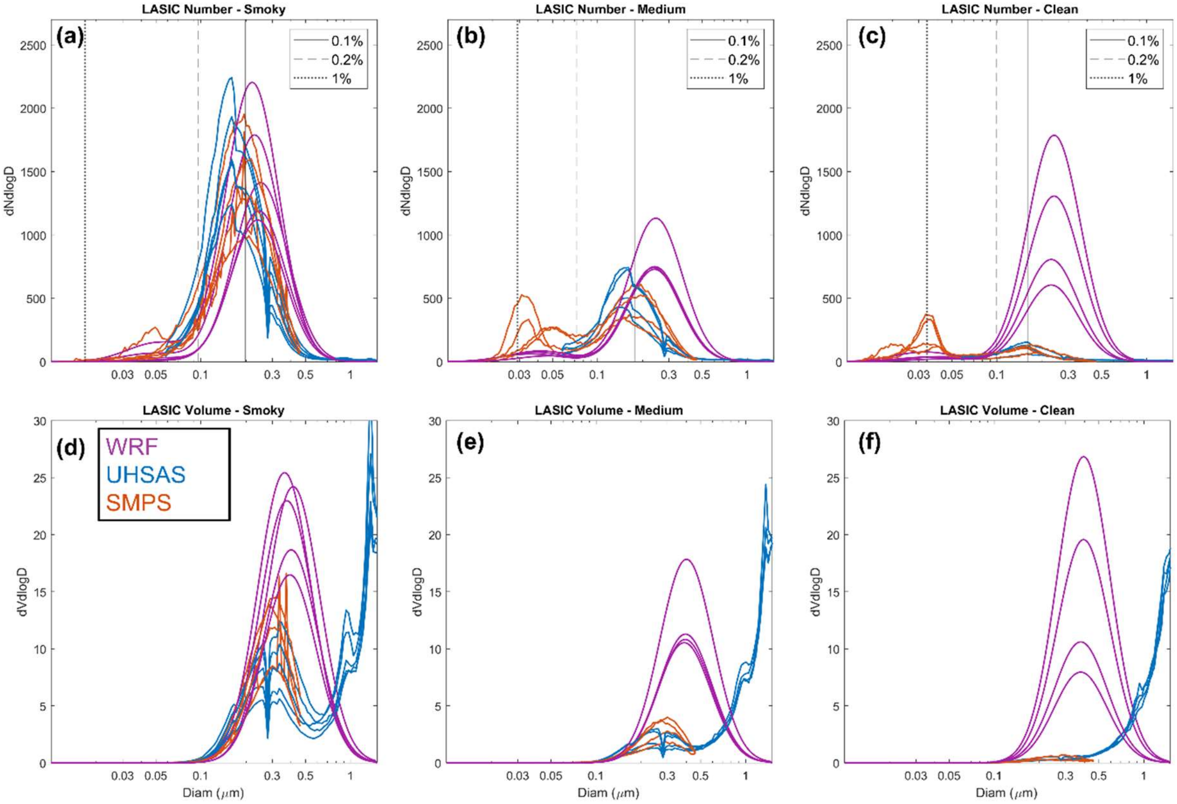

Figure 2.7: Number and volume distributions from LASIC selected to be representative of the range of conditions during smoky, medium, and clean conditions at ASI. WRF-CAM5 plots show the sum of the accumulation and nucleation mode lognormals.

There is also a persistent population of coarse aerosols through this period as well, predominantly impacting volume. The UHSAS volume distributions at ASI show a large coarse mode above 1 μm regardless of smokiness (Figs. 2.7d-f). This coarse mode also does not appear in most ORACLES FT data (Fig. 2.3b-c), suggesting that its emergence at ASI is driven not by smoke. The likely source is sea spray in the MBL (Clarke et al., 1998; Dedrick et al., 2022; Saliba et al., 2019). A caveat in this dataset is that the LASIC ARM emplacement was within ~500 meters of a sea cliff, where winds and breaking waves may represent a large, localized particle source that is much less influential elsewhere in the SEA BL.

2.3.2.2. Chemical Composition and Hygroscopicity

Observations from both ORACLES and CLARIFY AMS show a large difference in particle composition between the FT and the boundary layer (e.g., Fig. 2.4c vs. 2.4f) that is generally not captured in WRF-CAM5. Although the OA mass fraction is still comparable in the OA between the model and observations, the BC and especially SO_4 fraction are inconsistent. In particular, WRF-CAM5 does not reproduce the large increase in sulfate fraction in the BL compared to the FT. By mass fraction, sulfate in observations is enhanced from 11% to 26% in the CLARIFY FT to BL and from 11% to 37% in the ORACLES FT to BL. Since free tropospheric smoke is chemically similar between observations and the model, this discrepancy in the BL is unlikely to be related to a model misrepresentation of smoke aerosol composition itself. It could instead be a combination of WRF-CAM5 having weaker sulfate aerosol formation in the MBL—with this WRF-Chem build not including DMS emissions—as well as a lack OA removal. SO_2 is also co-emitted with smoke and tends to only weakly condense into sulfate aerosol in the FT, but aqueous chemistry drives more efficient condensation in the BL (Bianco et al., 2020; Fiedler et al., 2011; Rickly et al., 2022). Therefore, there may be a low model bias in either source emissions of SO_2 or in their aqueous chemical processing that limits model representation of the FT-to-MBL SO_4 gradient. There is also observational evidence of regular and frequent occurrences of new particle formation in the upper part of the remote MBL (Abel et al., 2020; Zheng et al., 2021) that have been hypothesized to be driven by DMS and thus contain sulfate. These could then subside into the BL and may be a locally dominant source of sulfate and new particles (Clarke et al., 1998). WRF-CAM5 also retains a large dust fraction in the ORACLES-sampling BL that does not appear in observations as described above. This suggests a model bias towards high fine-mode dust generation rates in the natural dust emission scheme, which is an issue previously identified in dust parameterizations (Kok, 2011).

Estimates of κ based on chemical composition rely on total volume, so the accumulation mode and the coarse mode are the dominant populations impacting chemical κ. Compared to BL observations from ORACLES and CLARIFY AMS, WRF-CAM5 κ remains biased low against the AMS (-.089 bias in ORACLES, -.084 in CLARIFY) (Figs. 2.4d, j). If chloride and dust are excluded to mimic the AMS, the model bias grows (to median bias -0.117 in ORACLES and -0.105 in CLARIFY). The higher sulfate fraction in the BL compared to the FT drives the corresponding higher BL κ, as seen by comparing the FT and BL composition in each sample set (e.g., Fig. 2.4b vs. 2.4e and 2.4c vs. 2.4f).

However, the number distribution is most relevant to CCN-based κ because it is used to determine D_{crit} at a given SS. Across all conditions, the D_{crit} at 0.1% SS generally falls in the middle of the accumulation mode, around 170-200 nm (Fig. 7a-c), and thus we expect that mode to be more representative of bulk smoke κ. D_{crit} at 0.2% SS falls in the range of 75-95 nm, which is in the lower tail of the accumulation mode for smoky periods and tends to be in the overlap region of the nucleation and accumulation mode for clean and medium smoke periods. D_{crit} at 1.0% SS is centered in the Aitken mode (15-35 nm). κ at 0.2% SS has been excluded from Fig. 6e during clean and medium-smoke periods, and 1.0% excluded from Fig. 6e during smoky periods, as the very low number concentration around their respective D_{crit} in these periods leads to highly unreliable κ estimates and eclipses meaningful analysis.

Focusing on the smoky period, LASIC κ at 0.2% CCN supersaturation is larger by a factor of 2 than at 0.1% SS (κ ~ 0.2 at 0.1% SS vs. κ ~ 0.45 at 0.2%). Based on these estimates of κ, the most hygroscopic particles are those near the lower tail of the accumulation mode. Therefore, during smoky periods it may be supposed that these are predominantly sulfate, nitrate, or ammonium particles, or a combination of coagulation and condensation of the same onto the less-hygroscopic BBAs. This is broadly in line with the hygroscopicity of Aitken-mode particles during clean and medium smoke periods, with a similar range of κ. However, it contrasts with FT κ values discussed in section 2.3.1.2, where κ in the 40-150 nm range is ~0.13, which is lower than κ in the bulk of the accumulation mode. This suggests processes in the MBL impact hygroscopicity of the lower tail of the accumulation mode, even in periods of high smoke loading.

WRF-CAM5 closely approximates the CCN-based κ from LASIC at 0.1% supersaturation (SS) and diverges greatly at 0.2% SS. (Fig. 2.6e). The narrow model variability in κ is explained by the consistent smoky conditions in WRF-CAM5 at ASI through this period, echoing the comparison to ORACLES. WRF-CAM5 also considers particles to be totally internally mixed within each mode, negating the possibility of compositional differences at different size ranges within one mode. With limited chemical evolution and no size-based differentiation possible in each mode, it is reasonable that the model does not produce large hygroscopicity changes. A deeper analysis of observed coating thicknesses and size-resolved particle composition is beyond the scope of this work.

2.3.2.3. Smoke Entrainment, Removal, and Rain at Ascension Island

The period of extremely low BC concentration (< 50 ng m^{-3}) observed by the LASIC SP2 between August 20th and 25th is generally not matched by WRF-CAM5. The model shows a median BC concentration bias of +1080% (+280 ng m^{-3}) during the same period when shifting by 1 day to account for the time lag vs. observations, and +1950% (+310 ng m^{-3}) if matched to observed times directly. However, during medium and smoky periods the BC timing is well-captured, matching the September 2016 findings of Shinozuka et al. (2020). WRF-CAM5 showed a median BC bias of +66% (+330 ng m^{-3}) during the smoky periods and +190% (250 ng m^{-3}) during the medium period. This contrasts with the FT, where WRF-CAM5 does not show a strong bias in smoke BC by either mass (Shinozuka et al., 2020) or mass-fraction (Fig. 2.4b, h). Therefore, the high model bias in BC amount at ASI suggests that the model overestimates smoke entrainment, underestimates smoke removal in the boundary layer, or both. We analyze evidence for both possibilities here.

CO is broadly considered a passive smoke tracer on timescales of weeks that is not removed by wet or dry scavenging of aerosols (Avey et al., 2007; Freitas et al., 2005; Garrett et al., 2010). After a smoke plume is processed by clouds and the aerosols are largely removed by coalescence and precipitation, the CO co-emitted with BBAs is expected to remain as a tracer of smoke presence. Thus, CO is a good tracer to isolate smoke entrainment. Figures 6a-b show a time series of both BC and CO at ASI, overlaid with rain measurements. We find that BC remains significantly higher in WRF-CAM5 than observations through most of August, while for CO the model tracks observations more closely. This points towards the model likely having unrealistically weak aerosol removal in the BL. If the main issue was overestimation of smoke entrainment, then CO would show similar overprediction to BC during the clean period because they entrain together.

Another piece of evidence supporting weak modeled aerosol removal on the BL can be seen by comparing the first (Aug 10-21) and the second (Aug 26-31) smoky periods (Figs. 2.6a,b). Observed BC and CO enhancements in these periods are significantly different (e.g., CO in period 2 is larger than in period 1, while BC is slightly less), while the model shows closer BC and CO enhancements for both periods. Subtracting a conservative estimate of 50 ppb background CO concentration, the first and second smoky periods have an observed median BC:ΔCO ratio of 0.0092 and 0.0064 (units μg m^{-3} : ppbv) respectively. A higher assumed background CO of 60 ppb—as seen in a fire-off run of WRF-CAM5 over this same period (Fig. A.3)—would only amplify this discrepancy. The model has a BC:ΔCO of 0.0146 and 0.0160 for the first and second periods, respectively. With no consideration of background concentration, the first and second periods showed BC:CO ratios of .0049 and .0037 in observations and .0085 and .0067 in WRF-CAM5, respectively. A likely explanation for the observed behavior is the different degrees of BL aerosol removal in the air masses reaching ASI in these two periods. A lack of this strong aerosol removal can explain the low degree of BC:CO variability in the model. These two pieces of evidence, together with the model overprediction of mean diameters in the BL (section 2.3.2.1), make a compelling case for concluding that aerosol removal in the BL is likely too weak compared to reality. Of note, the observed clean period from 21-25 Aug is likely caused by advection of clean air parcels to the island rather than removal, as evidenced by the very low CO concentration for the season (Pennypacker et al., 2020).

To better understand potential wet aerosol removal, we evaluate the model's ability to represent precipitation (Fig. 2.6a). We find that rain is far more frequent overall in the model than in the two observational datasets. The distribution of 3-hour rain accumulation in the model, on the other hand, skews towards lower rainfall volume in each period than in observations, even when limiting the model rain samples to only include those above the LASIC rain bucket detection threshold of 0.05mm h^{-1}. (Fig. 2.8). This is consistent with the well-known "drizzling problem" of global climate models (Chen et al., 2021; Stephens et al., 2010; Trenberth et al., 2003; Trenberth and Zhang, 2018). The underprediction of heavy rain events could be one of the reasons explaining weak aerosol removal, if they are more efficient than light drizzle at removing aerosols, although future work is needed to implement parameterizations that may tackle this issue (e.g., Chiu et al., 2021) and evaluate it in the context of aerosol removal.

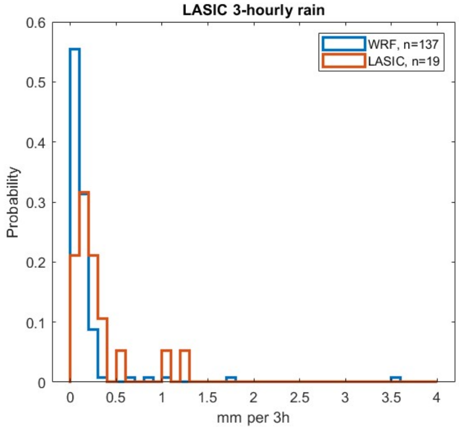

Figure 2.8: Histogram of 3-hourly rain rate measured by LASIC. In the legend, n represents the total number of rain events sampled over the detection threshold of 0.05mm per hr. Note UK Met rain data is only archived daily and is not included here.

Entrainment can be modulated by BL height and inversion strength (Karlsson et al., 2010; Wilcox, 2010), and thus are included in this evaluation (Figs. 2.6f-g). WRF-CAM5 shows reasonably good correlation with LASIC radiosonde observations of these two metrics. The model BL is slightly higher than observations, with a median bias of +220 m (+10%) during this month compared to the Heffter BLH, and +400m (+21%) compared to the recalculated BLH values based on the model algorithm. When only analyzing the clean and medium smoke loading periods, the bias is higher at +330m or +15% median bias compared to Heffter, and +510m or +27% compared to the recalculation. A deeper BL can result in enhanced smoke entrainment as smoke doesn't have to subside as much to reach the BL top, increasing the availability of smoke to entrain. On the other hand, WRF-CAM5 inversion strength is well represented or slightly overestimated depending on the calculation used, with a median bias of +0.14°K (+1.1%) compared to Heffter and +1.7°K (+21%) compared to the recalculation. A stronger inversion would be expected to lead to less mixing across this boundary and thus less entrainment, opposing potential effects due to a deeper BL (Karlsson et al., 2010; Wilcox, 2010). Thus, given that BL height and inversion strength biases are low and might result in opposite behavior, these don't support a persistent overprediction of entrainment. This is consistent with the timeseries of CO (Fig. 2.6b), which show a range of behaviors from CO overprediction (e.g., 1st smoky period) to underprediction (e.g., 2nd smoky period), implying a mixed behavior of model entrainment and not necessarily a persistent bias.

2.3.2.4. Aerosol Activation and Turbulence

ORACLES and CLARIFY took measurements of aerosols and cloud properties at fine scales, in close proximity to both, and with strong controls on sampling location. This avoids some of the assumptions and screening algorithms that add uncertainty to assessments based on remote sensing measurements, as well as provides better vertical resolution and sampling within clouds.

Aerosol activation into cloud droplets is analyzed here by comparing observed and modeled values of both mass-weighted cloud droplet number concentration (N_C) and average aerosol number concentration (N_A) immediately below that cloud, sampled across CLARIFY and ORACLES. A bias visible in WRF-CAM5 that does not appear in either ORACLES (Fig. 2.9a) or CLARIFY (Fig. 2.9b) observations is that the modeled clouds have a much higher upper limit of N_C. Observations show an upper range of 400-500 cm^{-3} across both campaigns, while WRF-CAM5 attains nearly 1000 cm^{-3}. This may be driven by strong updraft turbulence driving high activation as described below.

CLARIFY observations also capture a cloud population with both $N_C < 150$ cm^{-3} and $N_A <$ 300 cm^{-3} that was not seen in ORACLES or in WRF-CAM5. This difference between campaigns may be due to the more scattered clouds and more diluted smoke sampled in CLARIFY than in ORACLES. It may also represent a cloud population that is not substantially impacted by smoke, considering the low number concentration. As mentioned in the previous section, WRF-CAM5 has consistently high (> 400 cm^{-3}) smoke concentrations around ASI throughout August, so it fails to represent the low-smoke cloud interactions observed there.

The ratio of N_C to N_A, representing a rough aerosol activation efficiency, is shown in Figs. 2.9c-d. Median activation efficiency is 0.77 for ORACLES and 0.50 for CLARIFY observations, and 0.66 and 0.64 in the respective WRF-CAM5 samples. The shift in activation efficiency spectra between ORACLES and CLARIFY, as well as aerosol and cloud number concentration spectra, may reflect a change in predominant cloud domain, such as that from stratocumulus to cellular cumulus, that is not well captured in the model (Abel et al., 2020; Diamond et al., 2022; Zuidema et al., 2018b).

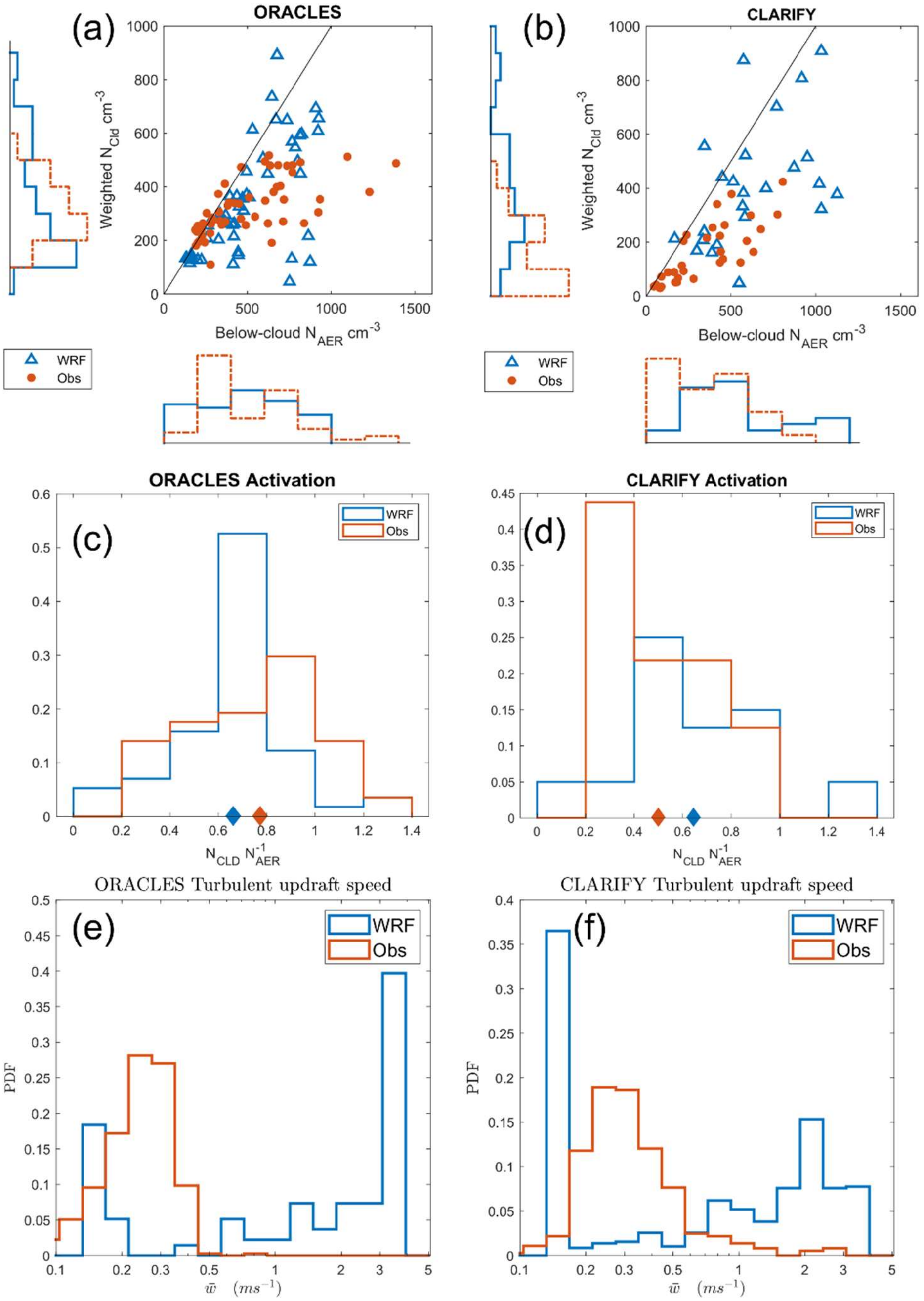

Figure 2.9: Observed and modeled cloud properties and BL turbulence. (a-b) Cloud droplet number (weighted by LWC) compared against below-cloud aerosol concentration from observations and WRF-CAM5 in (a) ORACLES and (b) CLARIFY cloud transects. Axes of (a) and (b) show kernel PDFs of each distribution, on the same scale. c-d) Normalized PDFs of activation efficiency, the ratio N_{CLD}/N_{AER} for each campaign and WRF-CAM5. Diamonds on the x-axes represent the median of the like-colored population. (e-f) Spectra of BL turbulent updrafts from each campaign WRF-CAM5 between 100m and 700m. Note: aerosol number concentration in observations is taken from PCASP for consistency across campaigns, which has a lower size limit of ~110nm. This cutoff was virtually imposed on the WRF-CAM5 size distribution as well for this figure.

Turbulent updraft strength is a main driver of the water vapor supersaturation within a lifted parcel, and thus the activation tendency of an aerosol population (Ditas et al., 2012; Prabhakaran et al., 2020). Compared to both ORACLES and CLARIFY BL measurements, WRF-CAM5 substantially overestimates the updraft strength (Fig. 2.9e-f) and has a bimodal TKE distribution, rather than the unimodal character of observations. The large peak in TKE distribution near 0.15 m s^{-1} in WRF-CAM5 comes from a coded lower-limit on TKE. These strong updrafts could generate a population of erroneously high N_C if conditions were suitable, which could explain why the model does not capture the observed N_C upper limit. We also note that the spread of N_C in the model is much larger than the observations (N_C standard deviation in observations=101 cm^{-3}; in WRF=219 cm^{-3}) while this is not the case for N_A (observed standard deviation=227 cm^{-3}; in WRF=236 cm^{-3}), which can also be explained by overpredicted spread in model TKE. If the model is under-mixing ambient air into clouds, despite the high TKE, it would also be underestimating dilution of N_c. Testing this would require further aircraft observations beyond the scope of this work. The observed probability distributions of TKE are consistent between the ORACLES and CLARIFY anemometers despite the large spatial separation and are consistent with values for ORACLES reported by Kacarab et al. (2020).

2.4. Conclusions

This work has analyzed the performance of WRF-CAM5 against the ORACLES, CLARIFY, and LASIC field campaigns. The goal has been to assess model representation of biomass-burning smoke and aerosol-cloud interactions in the SEA, especially focused on diagnosing process differences. Previous work, as well as our analyses, show that different instruments on the same aircraft platform and across platforms are often sufficiently consistent to compare jointly with the model, expanding our analysis and conclusions.

In the FT, WRF-CAM5 captures the average physical and chemical properties of the younger smoke measured by ORACLES but shows larger and consistent positive biases for the older smoke measured by CLARIFY. This implies issues with model representation of smoke aging. Mean diameter is captured within variability in the ORACLES observations after increasing the initial diameter in model emissions to be more consistent with literature and observed values. Although smoke composition in the FT is represented well in the model, especially the fractions of OA, sulfate, and BC, we find that WRF-CAM5 underpredicts hygroscopicity by ~25-35% in the smoky FT. This κ bias could be caused by a lack of NH_4 and NO_3 in the model, overprediction of dust, and misrepresentation of OA properties (e.g., low prescribed density and kappa, as well as the change in those values with age).

Notably, in both ORACLES and LASIC observations, we find that CCN-estimated κ exhibits a large range for smoky conditions across different particle sizes in the 20 nm-300 nm range. FT (ORACLES) smoke shows a lower κ in the lower tail of the accumulation mode compared to the center (κ ~0.1 vs. ~0.3 respectively) likely due to a larger fraction of black carbon at lower sizes. This suggests a large variance in mixing state across the accumulation mode that WRF-CAM5 is not able to capture, as it assumes total internal mixing per mode.

By comparing mean smoke properties using modeled age estimates in the FT, we find that WRF-CAM5 is likely missing significant aging processes impacting smoke mean diameter and composition. The OA:BC mass ratio as well as the OA:CO and BC:CO ratios compared across 4-12 days of transport show that OA is selectively being removed and therefore limiting particle growth, which is not represented by the model. This process is a valuable target for future work since current literature studying smoke aging beyond several hours is limited, and because simulated particle size can impact aerosol-cloud interactions and estimates of cloud radiative effects in the region.

Model evaluation in the boundary layer introduces processes such as DMS emissions, cloud processing, wet scavenging, and strong vertical mixing that strongly impact smoke evolution and properties and that have no consistent analog in the FT, leading to a new smoke evaluation regime. Our BL comparison focuses mostly on data from LASIC. First, we found that WRF-CAM5 is significantly overpredicting smoke amount (by mass and number) and diameter compared to LASIC. Some of this bias is likely tied to biases in the FT smoke that entrains, but a large part of the model discrepancy is likely due to scavenging differences. We also find that observations from LASIC show a substantial Aitken mode present during medium- and low-smoke conditions that is always lacking in the model. This is likely a combination of weak model scavenging and low model BL sulfate precursors contributing to weak new-particle formation. Observations also show a consistent coarse mode throughout August that is not apparent in WRF-CAM5.

Observations of aerosol composition in the boundary layer show a 2.5-3x relative enhancement of SO_4 in the MBL compared to the FT in both ORACLES and CLARIFY, that is not represented by the model. This suggests WRF-CAM5 has missing or weak processes that lead to sulfate aerosol in the MBL, such as BL ocean DMS emissions (not included in this model build), potentially insufficient BL SO2 from smoke, and smoke removal, all of which allow for periods of sulfate particle formation. During clean and medium-smoke loading periods, the LASIC SMPS also shows an Aitken mode that is likely driven by new particle formation and has hygroscopicity values similar to sulfate.

Hygroscopicity in MBL (LASIC) smoke, similar but opposite the trend in the FT, varies between the lower tail of the accumulation mode and its center (κ ~0.5 vs. ~0.2). This is likely caused by sulfate uptake of smaller particles through coagulation of the Aitken mode or precursor condensation. This suggests significantly different chemical composition at different sizes and thus some external mixing within the accumulation mode. The fact that this trend is apparent at very different smoke ages and locations suggests that it is a consistent feature of smoke aerosols, and one which WRF-CAM5 is not able to simulate due to its modes being internally mixed. This should be considered as a mitigating factor in future studies of BBA hygroscopicity and composition, as both are highly size-dependent. A future sensitivity study using newer κ values for the AMS and the model—such as from Schmale et al. (2020), generally significantly higher than those used here—could provide further insight into the importance of κ and chemical composition in cloud activation.

The substantial overprediction of aerosol concentration in the MBL at ASI could be explained by either too-strong smoke entrainment or too-weak aerosol removal in the MBL, but multiple pieces of evidence point to the latter being the primary factor. First, mean aerosol diameter substantially decreases in observations from 180-240nm FT in the CLARIFY and ORACLES FT to 140-180 nm in the LASIC MBL. The model shows little change in mean diameter. This points to cloud processing of aerosol rather than a smoke process on its own. Comparing the behavior of BL CO and BC concentrations can further provide insights. Also, observed BC to ΔCO ratios, assuming a background of 50 ppb CO, change substantially between the two heavily smoky periods (BC/ΔCO=0.0092 in the first, and 0.0064 in the second), which can be explained by differences in BC removal across the history of these airmasses. This variation is weaker in the model (BC/ΔCO =.0146 in the first smoky period, 0.0160 in the second). We also find that WRF-CAM5 has rain that is far more frequent, though lighter, than observations support—in line with the known "drizzle problem" of ESMs—which could contribute to a weak aerosol removal. Finally, model evaluation of inversion height, inversion strength, and MBL CO show modest biases (+10-21%, +1.1%, +0.5% mean biases respectively) that also oppose each other in illustrating entrainment tendency, and overall do not support a persistent overestimation of entrainment. During clean conditions, aerosols may have the largest relative impact on cloud droplet number (Kacarab et al., 2020) and are especially important to constraining aerosol-cloud radiative forcing (Gryspeerdt et al., 2023). An inaccurate representation of aerosol removal and smoke-free conditions should therefore be taken into account for future modeling analyses of aerosol-cloud-radiation interactions.

The activation ratio for below-cloud aerosols (0.1-3 μm) into liquid droplets is relatively constant in WRF-CAM5 samples in both ORACLES and CLARIFY at N_{CLD}/N_{AER} ~0.65. However, observations show a higher activation tendency in ORACLES (N_{CLD}/N_{AER} ~0.78) and lower in CLARIFY (N_{CLD}/N_{AER} ~0.5). Observed N_C in both aircraft campaigns shows an upper limit of ~400-500 cm^{-3}, which is exceeded occasionally by WRF-CAM5 by 300-500 cm^{-3} across both campaigns and leads to a wider modeled spectrum of N_{CLD}. Vertical TKE was analyzed using both ORACLES and CLARIFY anemometers. WRF-CAM5 is found to overestimate TKE by up to a factor of 10 in the boundary layer compared to both campaigns, as well as showing a bimodal distribution rather than the observed unimodal distribution. The strong model turbulence may contribute to the model exceeding the upper limit of observed N_{CLD} and overpredicting the N_{CLD} spread.

The performance of WRF-CAM5, despite its biases and missing processes, represents a useful tool for the study of smoke aerosols. LASIC, CLARIFY, and ORACLES present an especially rich suite of observations against which to compare model representations of major atmospheric processes such as boundary layer turbulence, smoke composition and size changes over long aging periods, and aerosol-cloud interactions (Shinozuka et al., 2020). Schemes allowing OA removal over aging timescales of ~14 days may substantially improve composition and bulk optical properties in models and thus need to be tested in future work. Sulfate representation in the MBL may also be improved by improving DMS emission schema, validating SO2 emissions and processing in smoke, and through improvements in scavenging schemes that allow for ultra-clean regions to emerge and lead to significant new particle formation.

The impact of smoke evolution on cloud droplet nucleation is highly variable and remains difficult to model in ESMs, which commonly have simple aerosol evolution schemes and aerosol mixing state assumptions, as well as frequently coarse resolutions of ~0.25-1 degree. If TKE spectra may be improved, then a more accurate aerosol chemistry and mixing state schema and better representation of aerosol removal in the MBL may improve cloud microphysical properties, which could help reduce uncertainties in modeled aerosol-cloud radiation interactions. Future work could use similar methodology presented in this work to evaluate other modeling systems to assess if similar biases are present and implement model improvements. Finally, an assessment of how these improvements modify effective radiative forcings and climate impacts of smoke should be performed.

Dataset Availability

VIIRS map available at: NRT VIIRS 375 m Active Fire product VNP14IMGT distributed from NASA FIRMS. Available on-line https://earthdata.nasa.gov/firms. doi:10.5067/FIRMS/VIIRS/VNP14IMGT_NRT.002

Observational datasets for ORACLES 2017, as well as colocated WRF-AAM plume age estimates, are available through the NASA ESPO data archive: https://espo.nasa.gov/ORACLES/archive/browse/oracles/id14/P3.

Observational datasets for CLARIFY-2017 are available at through the CEDA data archive: https://catalogue.ceda.ac.uk/uuid/38ab7089781a4560b067dd6c20af3769

Datasets for LASIC are available individually as follows on the ARM data archive. Data accessed between 01 Aug 2018 and 02 Feb 2022:

Weighing Bucket Precipitation Gauge: http://dx.doi.org/10.5439/1338194

Ultra-High Sensitivity Aerosol Spectrometer: http://dx.doi.org/10.5439/1333828

Scanning mobility particle sizer: http://dx.doi.org/10.5439/1225453

Cloud Condensation Nuclei Particle Counter (Column A):

http://dx.doi.org/10.5439/1323892

Cloud Condensation Nuclei Particle Counter (Column B):

http://dx.doi.org/10.5439/1323893

Condensation Particle Counter (CPCF): http://dx.doi.org/10.5439/1352536

Radiosonde Planetary Boundary Layer Height: http://dx.doi.org/10.5439/1150253

Author contributions

CH and PS designed the model–observation comparison. PS acquired the resources to support this research. AN, AND, SF, GM, HC, JMH, SGH, CK, SG, MK, AN, JR, AJS, KLT, RW, JZ, JU, and PZ provided data from instruments during the ORACLES, LASIC, and CLARIFY observation periods. CK, HW, JMH, JZ, PZ, SF, SG, SGH, and JU assisted with further analysis of observational data. CH led the model and observational data processing for this comparison with scripting assistance from PS. PS and CH ran the model and implemented configuration changes. CK, JPSW, JU, LRL, and YZ provided substantial components of model configuration. CH wrote the first draft. PS provided major input throughout writing and AJS, AND, GM, JR, JZ, LRL, PZ, RW, SF, SG, SGH, YZ provided further editing and feedback.

Competing interests

PZ and JH are guest editors for the ACP Special Issue: “ACP special issue: New observations and related modelling studies of the aerosol–cloud–climate system in the Southeast Atlantic and southern Africa regions.” The remaining authors declare that they have no conflict of interest.

Acknowledgements

ORACLES is a NASA Earth Venture Suborbital-2 investigation, funded by the US National Aeronautics and Space Administration (NASA)’s Earth Sciences Division and managed through the Earth System Science Pathfinder Program Office.

Financial Support

Financial support for this work was provided by NASA ORACLES grant 80NSSC19K1463 and funds from The Anthony and Jeanne Pritzker Family Foundation to PS, DOE LASIC grant DE-SC0018272 to PZ and PS, and the NERC CLARIFY-2017 Large Grant NE/L01358 to JH and HC. JZ was supported by DOE LASIC grant DE-SC0021250. SG was supported under the NASA Earth and Space Science Fellowship (grant nos. NNX15AF93G and NNX16A018H). GM and SG were supported by NASA (grant no. 80NSSC18K0222). YZ is supported by the U.S. NOAA Office of Climate AC4 Program (NA20OAR4310293). LRL is supported by Office of Science, U.S. Department of Energy Biological and Environmental Research as part of the Regional and Global Model Analysis program area. Pacific Northwest National Laboratory is operated for U.S. Department of Energy by Battelle Memorial Institute under Contract DE-AC05-76RL01830.

Chapter 3

Model sensitivities of biomass-burning aerosol photolytic aging, sulfate formation, and cloud droplet activation in the Southeastern Atlantic

Abstract

Biomass-burning smoke represents a complicated and important aspect of uncertainty in climate projections of radiative balance. It is subject to many chemical and microphysical processes that modify its properties including particle size, mixing state, composition, and optics. Smoke aerosols also have varied interactions with the atmosphere, especially liquid marine clouds, which may lead to drastic changes in cloud optical properties and lifetime. Here we focus on the southeastern Atlantic region and its outflow of African biomass-burning smoke. We evaluate smoke properties and processes in two state-of-the-art coupled earth-system models, the Energy Exascale Earth System Model (E3SM) and Community Earth System Model (CESM). These are compared against in situ aircraft observations from two field campaigns, ORACLES and CLARIFY-2017. Both models exhibit skill in representing smoke properties (e.g., smoke mean diameter, number concentration, and placement) compared to observations but multiple uncertainties remain. Observations show two major trends in smoke properties with age over 4-12 days: the nonmonotonic increase and subsequent decrease in smoke mean diameter, and a strict decrease in the mass ratio of organic aerosol (OA) to black carbon aerosol (BC) (OA:BC).

Both trends are generally not captured by the base configurations of the models despite the CESM base configuration including photolytic secondary organic aerosol (SOA) losses. E3SM representation is significantly improved by implementing the same photolytic loss scheme for SOA as CESM uses, likely due to having higher baseline SOA concentrations than CESM does in the region. E3SM OA:BC decreases with age are enhanced further with a parameterization that converts POA to SOA mass on a ~1-day timescale. The composition also changes moving into the boundary layer, despite the large smoke concentration, with a large observed increase in sulfate mass fraction compared to the smoky free troposphere. In order to accurately model this sulfate enhancement, the models require both emissions of dimethyl sulfide and photolytic/oxidative losses of OA. Both aerosol diameter and composition have an impact on cloud droplet activation, but in this region cloud droplet number concentration is predominantly sensitive to updraft strength. Both models show a large improvement in representation of CCN to N_{CLD} relationships when turbulent updrafts better match observed values. This study shows the value of integrating multiple campaigns' observations and expanding scope to understand multiple key processes and improving them in aerosol-cloud-radiation interactions in climate models.

3.1. Introduction

The uncertainty in modeled global effective radiative forcing remains dominated by aerosols and their interactions with radiation and clouds (Bellouin et al., 2020; Boucher et al., 2013; Myhre et al., 2013; Painemal, 2018; Szopa et al., 2021). Warm, bright, liquid clouds that form over ocean scenes, such as shallow cumulus, and regions with high aerosol loading are especially uncertain as there are many overlapping uncertain phenomena (Bellouin et al., 2020). There are overlapping uncertainties in aerosol composition, mixing state, location, optical properties, cloud extent and response to those aerosols, and dynamic processes such as large-scale subsidence and boundary layer (BL) turbulence. Aerosol-cloud interactions over the ocean drive huge differences in regional albedo, as the albedo difference between bright clouds and the dark ocean surface is nearly binary. Therefore, constraint on modeled aerosol properties, processes, and aerosol-cloud interactions is important to reducing model uncertainty (Doherty et al., 2022b).

A region with enormous aerosol emissions, the grassy savanna in the Southern Africa (roughly 5°S to 20°S) experiences widespread burning annually from July through September. These fires are for both agricultural clearing in the dry season and as a restorative and regular component of the regional ecosystem extending back far before global industrialization (Andela and Van Der Werf, 2014). This represents one of the largest sources of biomass-burning aerosols (BBAs) in the world over an average year and the largest during the burning season (Earl et al., 2015; Giglio et al., 2013). The smoke from these fires usually lofts into the free troposphere (FT) and is advected by the easterly jet to the west where it mixes into the large, semi-permanent stratocumulus cloud deck off the western African coast (Adebiyi and Zuidema, 2016). These regional features create a natural laboratory to improve understanding of aerosol-radiation and aerosol-cloud interactions.

With this goal in mind, among others, this work examines modeling performance against two large field campaigns that were deployed in the southeast Atlantic Ocean area overlapping in August of 2017. All of these campaigns studied various aspects of biomass-burning smoke, clouds, radiation, and the vital dynamics of this region. ORACLES (ObseRvations of Aerosols above CLouds and their intEractionS) was a NASA aircraft-based campaign deploying during periods of the burning seasons of 2016, 2017, and 2018 (Redemann et al., 2021). CLARIFY-2017 (CLoud–Aerosol–Radiation Interaction and Forcing: Year 2017, (Haywood et al., 2021), was a campaign by the UK's Natural Environment Research Council (NERC) utilizing the UK Facility for Airborne Atmospheric Measurements (FAAM) aircraft. It was based primarily around Ascension Island (ASI) in the remote southern Atlantic.

Previous analyses against ORACLES observations have shown that E3SM and WRF-Chem demonstrate skill at representing smoke plume concentration and vertical placement in this region (Shinozuka et al., 2020). WRF-Chem, among other models, has also been evaluated to understand the direct aerosol radiative effect from smoke (Doherty et al., 2022b) and more broadly cross-campaign regional aerosol physical and chemical processes (Howes et al., 2023). CESM version 2 has shown realistic AOD in the continental African burning region in June-July-August when evaluated for air quality (Tang et al., 2023) and regional smoke distribution and gradients compared with previous field campaign data (Wyant et al., 2015). While these studies have variously shown these models to be up to the task of broadly studying BBAs in this region, there are large independent process uncertainties.

To better constrain these uncertainties, we focus analysis here on a few key processes and their sensitivities in CESM and E3SM. In section 3.2, we overview the model configurations as well as campaigns and instrumentation systems used from ORACLES and CLARIFY and outline our analytical methods. Section 3.3 is divided into three parts, aligning with the three major processes under study here that all impact aerosol properties and aerosol-cloud-radiation interactions. These are also all key process gaps identified previously in a state-of-the-art climate model in Howes et al. (Howes et al., 2023). Section 3.3.1 focuses on the FT, where smoke advects and evolves mostly independent of other aerosols and clouds for long periods in thick plumes. We first review overall model performance in representing smoke aerosol size, quantity, and composition compared to observations. Then we discuss the evidence for the loss of organic aerosol driving changes in particle size and composition over multiple weeks. In section 3.3.2, we analyze model performance in the boundary layer, where smoke entrains and is subject to processes such as scavenging, mixing with sea spray, and sulfate particle formation. We discuss an observed large increase in sulfate mass fraction in the BL compared to the free troposphere and the effect of model precursor gas emissions and organic aerosol losses in representing this chemical shift. In section 3.3.3, we scrutinize the sensitivity of cloud droplet number concentration to BL aerosol loading, the chemical sensitivities previously described, and turbulent updraft strength.

3.2. Methods

This work utilizes a wide range of simultaneous observations to understand aerosol properties. We also incorporate observations from multiple campaigns across the region in order to better understand the processes over time and to control intra-campaign instrument uncertainties. In this section, we first briefly discuss the observational platforms used for this study and notes on analytical methods. Second, we describe the models used here.

3.2.1. Observation Systems and Analytical Methods

The observational datasets, analytical methods, and derived quantities closely follow the methods of Howes et al. (2023). We will summarize these here in brief and expand on new analyses.

This work uses observations from two field campaigns in the SEA that overlapped in August of 2017, ORACLES and CLARIFY-2017. We use various instrumentation from across both campaigns to measure aerosol number and size distribution, cloud nucleation ability, chemical composition including black carbon, cloud droplet number, liquid water, CO, and thermodynamic properties such as temperature, pressure, winds, and relative humidity~~,~~ through the BL and FT from ORACLES and CLARIFY. We use a subset of the instruments analyzed and attributed in Table 1 of Howes et al. (2023).

Aircraft samples of FT smoke were selected to focus on short, contiguous samples of high smoke concentration taken during level legs of the flight. This allowed for each sample to represent smoke with relatively consistent properties and time of emission, while still sampling across the observed space of smoke properties. The BL was assumed to be far better vertically mixed than the FT, as well as having aerosol emission and scavenging processes that did not occur in the FT, and samples were aggregated between 100 and 700m above sea level. We use the same filtering thresholds and sample selection as in Howes et al. (2023). Samples of low clouds in both observations and models are taken based on thresholds of N_{CLD} and liquid water content as described by Howes et al. (2023), matching continuous flight segments that passed entirely through a low cloud layer.

From observations and model data, we calculate the following quantities: mean cloud droplet number concentration weighted by liquid water content, geometric mean particle diameter, activation efficiency (N_{CLD} / N_{AER}), and characteristic turbulent updraft speed. Mathematical details and theoretical bases for each are found in Howes et al. (2023). Age was calculated based on average concentrations of age tracers in a forecasting simulation of WRF-AAM used during ORACLES and calculated along the flight track of each campaign. Figure 3.2 shows aerosol properties binned by the age of each sample point. Due to instrument availability limiting the sample size, aging days 8-9 and 10-12 have each been aggregated for the OA:BC mass ratio in figures 3.2b and 3.2d. In addition, an outlier of three datapoints—all coming from the same ORACLES flight at adjacent times—were removed from the 9 days' aging bin in the OA:BC dataset. These anomalous points are a result of the WRF-AAM model forecasting a much weaker smoke plume than observed, resulting in unrealistic age estimates, and which is otherwise not a systemic issue. This results in all ORACLES measurements having ages of 7 days or younger and CLARIFY measurements having ages of 8 days or older, which is consistent with the locations where these campaigns happened with respect to the easterly smoke transport.

In order to illustrate various aerosol and cloud trends over the sampling region (Figs. 3.5 and 3.6) we calculate the per-column averages for each quantity. For clouds, these are filtered to a cloud droplet number concentration (N_{CLD}) above 1 cm^{-3} and liquid water content above 0.1 mg cm^{-3}. These thresholds are adjusted to maximize low cloud sample number but based first on values of 10 cm^{-3} and 0.05 g m^{-3} used by Gupta et al. (Gupta et al., 2021). For smoke, the filter was smoke mass (OA + BC + SO_4) > 1 μg cm^{-3}, BC > 0.1 μg cm^{-3}, and limited to the FT by altitude (z) 1200 m < z < 6000m and RH < 80%. The BL aerosol was filtered by 100 m < z < 1000 m, aerosol total mass > 1 μg cm^{-3}, and avoided clouds with RH < 95%. These thresholds are similar to those used by Howes et al. for similar SEA smoke analysis (Howes et al., 2023). Cloud fraction is calculated per column with the maximum overlap assumption (XiaoCong et al., 2016) from the surface up to ~350hPa at a given time. The goal of this approach is to show the average properties of FT smoke, clouds, and BL aerosols, across the region, when those aerosols and clouds are present.

Both E3SM and CESM aerosol parameterizations resolve accumulation-mode dust, NaCl, BC, and differentiated POA and SOA, as well as separating primary (emission)-mode and accumulation-mode for both POA and BC. The AMS instruments in ORACLES and CLARIFY-2017, in addition to OA and SO_4, measured mass concentration of aerosol nitrate and ammonium. For this study, we show only the species that are available from both observations and the models for an apples-to-apples comparison. Species such as dust and chloride are both infrequent in the FT and are either not observed or present unique observational challenges. The relative FT mass fractions of all available species in models and observations are shown in appendix figure A.4.

3.2.2. Model Configurations

The first of the two Earth-system models used in this work is the US Department of Energy's Energy Exascale Earth System Model (E3SM), version 2 with the E3SM Atmospheric Model version 2 (EAMv2) (Golaz et al., 2022) including the Modal Aerosol

Module (MAM4, (Liu et al., 2016) four-mode aerosol microphysics and an updated version of the CLUBB boundary layer physics and yield-based SOA formation based on precursor gas emissions calculated offline. The model is run globally at 1-degree resolution and 72 vertical levels. This research simulation is initialized starting 1 July, 2017 and model winds are nudged to the Modern-Era Retrospective analysis for Research and Applications, Version 2 (MERRA-2, (Gelaro et al., 2017; Tang et al., 2022b). We use daily fire emissions from the Global Fire Emissions Database (Randerson et al., 2017). DMS emissions are 2010 climatology from the Parallel Ocean Program model (Le Clainche et al., 2010). This specific configuration is referred to as $\text{E3SM}_{\text{BASE}}$ in the remainder of this study.

The second model in this study is the Community Earth System Model version 2 (CESMv2) developed by the University Corporation for Atmospheric Research (UCAR). We use the CESM configuration built as part of the NCAR Multi-Scale Infrastructure for Chemistry Modeling (MUSICA) project as of January 2023, as described in Tang et al. (2023). This includes the Community Atmosphere Model version 6 (CAM6) atmospheric physics including MAM4 aerosols (Liu et al., 2016), CAM-Chem tropospheric and stratospheric chemistry (Lamarque et al., 2011), Cloud Layers Unified by Binormals (CLUBB) boundary layer physics (Bogenschutz et al., 2012; Golaz et al., 2002), and DOCN prescribed ocean model. SOA is represented with a Volatility Basis Set (VBS) that includes adjustments for SOA loss, including photolytic removal (Tilmes et al., 2019). The model was run at global 1-degree resolution, refined to ~28km over the entirety of Africa and the SEA region. The model was initialized 1 December 2016 and ran through August 2017 with nudging of temperature and winds to MERRA2 (Gelaro et al., 2017). Fire emissions come from the Quick Fire Emissions Dataset, version 2 (QFED2, (Darmenov et al., 2015) with a superimposed diurnal cycle and fixed vertical distribution at the time of emission to resemble real smoke trends (Tang et al., 2022b). The base configuration used here does not have DMS emissions. This specific configuration is referred to as $\mathrm{CESM_{BASE}}$ in the remainder of this study.

This work also involves testing sensitivity of both E3SM and CESM. First, as will be discussed in section 3.3.1.2, the impact of photolysis on SOA losses was added to E3SM, matching that in $\mathrm{CESM_{BASE}}$. BBAs emitted from fires in Southern Africa take between ~4-14 days to travel in the FT to Ascension Island during which it ages and can undergo significant changes to particle mass, composition, mixing state, optical properties, and hygroscopicity (Chang et al., 2010; Che et al., 2022; Kuwata et al., 2011; Sedlacek et al., 2022). There is significant evidence from observations and lab studies that organics in biomass-burning smoke are evaporated on timescales of several days after emission due to heterogeneous oxidation, fragmentation, and photolysis of organic molecules that lead OA to re-volatilize and evaporate (Hodzic et al., 2016). The photolytic oxidation scheme used here is described and has been evaluated in Lou et al.(2020) and Zawadowicz et al. (2020), showing improvement in representing SOA sinks in the troposphere, and is being included in the newest version of E3SM (version 3). The scheme removes SOA at a rate of 0.04% of the NO_2 photolysis rate, lowering mean SOA lifetime from 10 days to ~3 days. The photolysis functions to simply remove secondary organic aerosol (SOA) mass from the aerosol phase over time. This serves as a proxy for both the photolytic chemistry and the heterogeneous oxidation/fragmentation that have been suggested to explain the observed evaporation of organics in BB smoke over several days (Che et al., 2022; Dobracki et al., 2023; Konovalov et al., 2019; Kroll et al., 2009; Lou et al., 2020; O'Brien and Kroll, 2019; Sedlacek et al., 2022). We refer to the build of E3SM with photolysis as E3SM_{PH} (E3SM-photolysis).

Second, we implement a scheme in E3SM that converts primary organic aerosol (POA) to secondary (SOA) on a ~1-day characteristic timescale (Lou et al., 2020; Shrivastava et al., 2017). This was initially developed for E3SM to simplify the chemistry of forming SOA from precursors gases but serves well to evolve primary organics into the secondary mode as they oxidize. As a result, when combined with the photolytic oxidation scheme, it exposes most of the BB OA in the model to possible losses. We refer to this modification of base E3SM as $\text{E3SM}_{\text{PH-CON}}$ (E3SM-photolysis-conversion).

Third, we analyze the impact of DMS emissions on sulfate formation in both models by zeroing out all oceanic DMS flux in E3SM ($\text{E3SM}_{\text{NODMS}}$) and, conversely, by adding the same DMS emissions into CESM as what $\text{E3SM}_{\text{BASE}}$ uses to create CESM_{DMS}.

Finally, we examine sensitivity of the relationship between cloud droplet number concentration and aerosol number concentration by adjusting the sub-cloud updraft velocity, W, in the cloud activation schemes of both CESM and E3SM. This quantity corresponds directly with the updraft spectrum width derived from aircraft observations (Howes et al., 2023; Kacarab et al., 2020; Morales and Nenes, 2010). Of note, this changes were not made in the planetary boundary scheme, but solely in the calculation of cloud droplet number. The changed updraft strength itself creates no dynamical changes to the modeled atmosphere, although the resulting changes in cloud droplet number create dynamical feedbacks in a fully coupled atmosphere such as this. We refer to these modifications of base E3SM and CESM respectively as E3SM$_{2W}$ and CESM$_{2W}$.

3.3. Results

We discuss here our findings on major processes related to smoke evolution through the SEA as well as efforts to realign the models or otherwise sensitivity-test for factors driving model biases. We first discuss the properties and aging of smoke in the FT, then the contrast between FT and BL aerosol composition, and finally properties and sensitivity of the low marine clouds throughout the SEA.

3.3.1. FT Properties and Aging

The strong easterly mid-tropospheric winds in the FT are the primary force driving smoke advection through the SEA (Adebiyi and Zuidema, 2016). Smoke in the region is relatively undisturbed in the FT, with very little cloud processing or influence from other aerosol populations during the burning season, such as exist in the BL. Thus, it is a good location in which to evaluate model representation of biomass-burning smoke, as well as to closely examine smoke evolution over time periods of days to weeks in relatively controlled conditions.

3.3.1.1. Base Model Performance

During the burning season, smoke transported from the African mainland entrains into the BL periodically (Diamond et al., 2018) although the stability of the MBL capping inversion often keeps the FT aerosol population from mixing into the BL (Gordon et al., 2018; Herbert et al., 2020). Smoke in the FT through this region generally stays in the lower

FT (from roughly cloud-top to 3km) (Shinozuka et al., 2020). In this section, we analyze the performance of the base configurations—E3SM$_{\text{BASE}}$ and CESM$_{\text{BASE}}$—against observed smoke properties. This provides a starting point for understanding model sensitivities and processes.

Figure 3.1 shows the performance and spread of the models against observations of smoke mean diameter, number concentration, and mass concentration in ORACLES (Figs. 3.1a-c) and CLARIFY (Figs. 3.1d-f). The mean values of each quantity are shown in Table 3.1. E3SM$_{\text{BASE}}$ and CESM$_{\text{BASE}}$ generally have underestimate mean diameter from both ORACLES and CLARIFY with low biases of 6-30% depending on model and observation chosen. Both models' fire emissions inputs specify both mass and number per size mode, which necessarily assumes particle diameters. Thus, there is likely a bias in these assumptions towards low diameters at the time of emission, which persists through the long-distance advection despite the size distribution evolving freely in MAM4 after emission. Another possibility is that BBAs at the point of emission in the model are treated as dispersed over the entire grid cell in which they are located, making early particle coagulation inefficient when in reality the plume is very concentrated in a small area close to the fire. Our previous work (Howes et al., 2023) found a similar bias in fire emission sizes in WRF-Chem, and an update to bring the assumed emission diameter closer to both ORACLES-observed and previously reported values around ~160nm improved diameter representation. We have not made this adjustment in CESM and E3SM for this work. Figures 3.5g and 3.5k show maps of base modeled mean particle diameters in the smoky FT, with a general trend towards growth as the smoke travels westward from the mainland.

The average number concentration (Figs. 3.1b, e) of smoke in E3SM$_{BASE}$ and CESM$_{BASE}$ is within the central observed ranges, although the modeled spread is much broader than CLARIFY observations suggest. Number concentration bias is -11 to +12% in E3SM$_{BASE}$ and +2-32% in CESM$_{BASE}$. Mass concentration is biased high and low in E3SM$_{BASE}$ (+24-61%) and CESM$_{BASE}$ (-12% to -29%), respectively (Figs. 3.1c, d). The mass difference is likely not driven by differences in the fire emissions inventories between the two models, as other analyses have shown GFED to generally underestimate fire particulate emissions, and QFED to overestimate them (Bilgiç et al., 2023; Liu et al., 2020). E3SM$_{BASE}$ also appears to have more SOA than CESM$_{BASE}$ (Fig. A.4), with SOA comprising 52% of total aerosol mass and 62% of OA mass in E3SM$_{BASE}$ while CESM$_{BASE}$ shows 25% total BBA mass made up of SOA, and 32% of OA mass.

The observed model composition of FT BBA averaged across ORACLES and CLARIFY FT samples is shown in Figure 3.2. Focusing on the FT composition in observations and the base models (Figs. 3.2a-c), the models do well in representing the mass fraction of OA and especially SO_4, although the models show a bias towards low BC fraction, especially E3SM$_{BASE}$. BL aerosol representation and the impact of other model configurations on composition will be discussed further in section 3.3.1.2 and 3.3.2.

Both base models show a strong ability to capture the range of observed mean smoke size, amount, and chemical properties in both SEA field campaigns. Since the model samples are selected to collocate with each observation, this indicates that the models are placing BB smoke in the right place and with the right properties.

3.3.1.2. Aging

Observations from ORACLES and CLARIFY support a very dynamic particle diameter and OA:BC mass ratio through this region over ~12 days of aging. Figure 3.3a depicts the observed PCASP diameter increasing up to ~240nm by 6 days, then decreasing and plateauing to ~215 nm through 6-12 days. The models largely do not capture this trend. Diameter over time in E3SM$_{\text{BASE}}$ and CESM$_{\text{BASE}}$ is noisy, but both show a mean trend of increasing diameter from 4-12 days when collocating with aircraft observations, which is more broadly evident in larger regional maps (Fig. 3.5). The observed trend may be partially explained by the steady decrease in the observed OA:BC mass ratio across this time range (Fig. 3.3b), showing that OA is getting selectively lost during this period. Comparing the maximum and minimum day-averaged OA:BC values, observations show a ~55% loss rate over this interval. This also suggests that the decreasing diameter is likely not a result of other microphysical processes already represented in the models, such as aerosol evaporation as the plume dilutes or influxes of large quantities of smaller particles shifting the size distribution down. Both E3SM$_{\text{BASE}}$ and CESM$_{\text{BASE}}$ have only slight modest in OA:BC profiles through this time range that do not match observed losses. E3SM OA:BC decreases by ~8% and CESM decreases by ~25%, with both showing a notable non-monotonicity over this interval. The PCASP, as an optical instrument, is sensitive to changing composition and optical properties in smoke over time. For example, an increasing absorptivity of smoke would decrease its scattering signal in the PCASP and result in a reduction in reported size. However, this is likely a relatively small effect here. The PCASP compares well with the UHSAS and LDMA in ORACLES, the latter of which does not rely on optical properties. Another UHSAS and SMPS—the latter being a mobility-based aerosol sizer similar to the LDMA—at LASIC also report consistently similar mean diameters through the month and with various smoke loadings (Howes et al., 2023). Thus, potential optical changes and uncertainties are likely a small on diameter trends, although may have larger impacts on regional radiative balance.

We implement the SOA photolysis and POA-SOA conversion schemes to E3SM$_{\mathrm{BASE}}$ as described in section 3.2 to check the model sensitivity. We find that E3SM$_{\mathrm{PH}}$ and E3SM$_{\mathrm{PH\text{-}CON}}$ both improved the shape of the trend in diameter, bending the slope downwards. The absolute decrease in diameter across the entire aging range is not unexpected considering the oxidative SOA loss amounted to a large per-particle loss of aerosol mass over time. OA:BC evolution is much better captured in E3SM$_{\mathrm{PH}}$ than E3SM$_{\mathrm{BASE}}$ (OA:BC decrease of ~38%), with an aging trend line that follows observations well despite a remaining bias. The addition of the POA-SOA conversion scheme further decreases the bias against observations by shifting more POA into SOA and thus making it subject to the same photolytic losses (decrease of ~60%). Correlation of the time-series of OA:BC with observations improves from E3SM$_{\mathrm{BASE}}$ (r = 0.84) to E3SM$_{\mathrm{PH}}$ (r = 0.95) and E3SM$_{\mathrm{PH\text{-}CON}}$ (r = 0.93).

CESM$_{\mathrm{BASE}}$ correlation with OA:BC observations is poor (r = 0.38). This is a notable inter-model difference, as CESM$_{\mathrm{BASE}}$ already contains the photolytic removal scheme being added to E3SM. While the magnitude of the of OA:BC decrease in CESM$_{\mathrm{BASE}}$ is weaker than observations, it is still significantly stronger than E3SM$_{\mathrm{BASE}}$. This decrease is more clearly visible across the region in figure 3.5e, where CESM shows a consistent decrease of OA fraction from ~90% near the fires to ~75% much further west. The shallower decrease compared to E3SM$_{\mathrm{PH}}$ could be explained by a higher base rate of SOA formation in E3SM$_{\mathrm{BASE}}$

than $\mathrm{CESM_{BASE}}$, exposing more of the OA mass to losses (visible in the high SOA fraction of $\mathrm{E3SM_{BASE}}$ in Fig. A.4). The yield-based SOA formation in E3SM is significantly simpler than the VBS in CESM so differences may be unexpected. A deeper look into SOA formation and loss rates and their sensitivities between model configurations is a useful target for future work.

The photolysis and POA-SOA schemes also impact the average composition (Figs. 3.2g-h). The average mass fraction of OA in the FT decreases from 86% in $\mathrm{E3SM_{BASE}}$ to 81% in $\mathrm{E3SM_{PH}}$ and to 74% in $\mathrm{E3SM_{PH\text{-}CON}}$. This end result is very close to the observed OA fraction of 76% averaged across both aircraft campaigns. This decrease in OA with little change in SO_4 and BC results in an increase of these fractions, and therefore an improved representation of BC compared to $\mathrm{E3SM_{BASE}}$ and a high bias in FT SO_4 in $\mathrm{E3SM_{PH}}$ and $\mathrm{E3SM_{PH\text{-}CON}}$. The OA decrease also has implications for the fraction of BL sulfate, as will be discussed in section 3.3.2.

This trend in observations is also illustrated over the entire region in figures 3.5a-g. There is a large and widespread change in E3SM FT smoke OA fraction and diameter between $\mathrm{E3SM_{BASE}}$ (row 1) and updated configurations (rows 2-4). As the smoke is advecting westward, $\mathrm{E3SM_{PH}}$ and $\mathrm{E3SM_{PH\text{-}CON}}$ show a clear gradient of decreasing FT smoke OA mass fraction and decreasing diameter compared to the base run. Near 15°W—near Ascension Island—OA mass percentage is reduced by ~15% and diameter is reduced by ~30 nm in $\mathrm{E3SM_{PH}}$, and by ~30% and ~45nm respectively in $\mathrm{E3SM_{PH\text{-}CON}}$. We expect this to have significant implications for accurate modeling of the radiative effects of smoke through the region, on top of the existing uncertainties in entrainment and scavenging.

Changing DMS results in a very small increase in FT OA fraction and diameter in E3SM$_{NODMS}$, and negligible changes for either in CESM$_{DMS}$.

3.3.2. Boundary Layer Sulfate

As the MBL has significant processes impacting aerosol properties, such as emissions of new particles, cloud processing, and wet scavenging, it cannot be assumed to have similar aerosol properties as the FT smoke entraining into it. Figure 3.2 illustrates the FT and BL compositions side-by-side from observations as well as each model simulation. The strongest discrepancy across base models and observations is the inaccurate ratio of OA to SO_4 mass. Observations show that there is a large increase in the mass fraction of sulfate in the BL compared to the FT, growing from 13% to 37% of aerosol mass. This increase is partially captured in the base models (Figs. 3.2e, f) but the increase is weak. E3SM$_{BASE}$ has an increase of SO_4 fraction from 11% to 22%, and CESM$_{BASE}$ shows an increase from 11% to 19%. One plausible cause of this difference is oceanic emissions of DMS as a sulfate precursor. By adding monthly-average DMS climatology to CESM, we see a stronger sulfate increase from FT to BL of 11% to 24% in CESM$_{DMS}$. Similarly, by removing the DMS emissions in E3SM, we see a reduced enhancement of 10% to 16% in E3SM$_{NODMS}$. The oxidative loss of SOA also plays a part by reducing the fraction of total OA, necessarily increasing the fraction of SO_4. E3SM$_{PH}$ shows an increase from 15% to 35%, while E3SM$_{PH-CON}$ increases SO_4 from 19% to 44%, even surpassing the observed SO_4 fraction in the MBL.

The model sensitivity to DMS emissions in the SEA more broadly is shown in figures 3.5p and 3.5r. The sign of the change in SO_4 fraction tracks with the change in DMS emissions (addition or removal), with the strongest impact south of 10°S latitude. Both models show a similar sensitivity to the change in DMS emissions.

In summary, BL SO_4 fraction is best represented when there are both realistic DMS emissions and long-term SOA removal. The resulting changes are important to representing particle optical properties, chemical activity, and hygroscopicity. DMS may also have a significant microphysical impact on N_{CLD} by impacting number concentrations. Cloud droplet number is sensitive to these microphysical and chemical changes as well as turbulence, another critical variable in cloud droplet activation, especially in low-latitude clouds (Ditas et al., 2012; Ogura et al., 2017; Prabhakaran et al., 2020). All of these processes and their sensitivities are crucial to accurate model representation of cloud bulk properties and evolution.

3.3.3. Clouds and Updrafts

Cloud droplet number is strongly tied to cloud albedo and optical thickness, precipitation, lifetime, and the stratocumulus-to-cumulus transition (Painemal, 2018; Yamaguchi et al., 2017). With huge aerosol loading from BB smoke entraining into the BL, the SEA during the burning season has a very high loading of particles that may act as CCN. The result is that the cloud droplet activation of aerosols is often most sensitive to the attainable supersaturation, which itself is driven by turbulent updrafts (Kacarab et al., 2020; Karydis et al., 2012). In this section we analyze observations of cloud vertical profiles to understand the cloud droplet response to aerosols and apply a sensitivity test to both CESM and E3SM to examine the impact of a bias in modeled turbulent updrafts.

Figures 3.4a-b and 3.4i-j show the spread of cloud droplet number concentration against the corresponding below-cloud aerosol concentrations for each sample. $\mathrm{CESM}_{\mathrm{BASE}}$ and $\mathrm{E3SM}_{\mathrm{BASE}}$ both significantly underpredict ORACLES N_{C} through the whole range of below-cloud aerosol number concentrations. Observations from ORACLES have a mean activation ratio of N_{CLD}/N_{AER} of 0.76, while the fraction in $\mathrm{E3SM}_{\mathrm{BASE}}$ is 0.37and in $\mathrm{CESM}_{\mathrm{BASE}}$ is 0.47. CLARIFY shows an activation ratio of 0.51, $\mathrm{E3SM}_{\mathrm{BASE}}$ is close at 0.54—but with a wider spread than observations—and $\mathrm{CESM}_{\mathrm{BASE}}$ is again low at 0.18. Both models fail to represent the population of low-concentration aerosols seen in the lower-left corner of each subfigure.

This under-activation trend follows a bias in both $\mathrm{E3SM}_{\mathrm{BASE}}$ and $\mathrm{CESM}_{\mathrm{BASE}}$ towards underestimated mean and maximum updraft speeds from the models' boundary layer schemes (Figs 3.4e-f, m-n). This bias persists clearly in both ORACLES and CLARIFY. This evaluation is also supported by previous work (Howes et al., 2023) which found an extremely wide updraft spectrum and resulting N_{CLD} spectrum. Therefore, we tested the sensitivity of N_{CLD} to a doubling of the updraft speed within the aerosol-cloud activation scheme. We choose a factor of 2 to roughly account for the initial bias of modeled turbulence against ORACLES observations. The resulting updraft spectra are shown in the second and fourth columns of figure 4 for $\mathrm{E3SM}_{\mathrm{2W}}$ and $\mathrm{CESM}_{\mathrm{2W}}$ respectively. The doubled updraft speed does not translate directly to shifting the spectra up by a factor of 2, likely because the resulting change to N_{CLD} creates boundary layer feedbacks, such as through enhanced cloud-top radiative cooling and convection with a higher droplet number. In both models, the doubling of turbulence ends up shifting the mode of the distribution higher than that of observations, and in the case of $E3SM_{2W}$ also interestingly generates a bimodal updraft distribution. The doubled updrafts result in an increase of the mean activation ratio in $E3SM_{2W}$ from 0.37 to 0.50 in ORACLES and from 0.54 to 0.60 in CLARIFY. Similarly, $CESM_{2W}$ shows an increase in mean activation ratio from 0.47 to 0.68 in ORACLES, and from 0.18 to 0.35 in CLARIFY. Mean N_{CLD} is increased by 72 cm^{-3} for CESM in ORACLES and CLARIFY (a 46% and 87% increase respectively), and by 49-103 cm^{-3} for E3SM in ORACLES and CLARIFY (a 60% and 21% increase respectively).

The large resulting increase in cloud droplet number for both models, with relatively unchanged aerosol number, shows that modeled N_{CLD} in both ORACLES and CLARIFY sampling is highly sensitive to this increase, possibly even dominated by it as a model sensitivity under these conditions, as has been suggested in other work (Eidhammer et al., 2024; Ogura et al., 2017). Further, this result suggests that the modeled spectrum of updraft turbulence may have a large impact on whether stratocumulus cloud properties are realistic over a region, rather than simply the mean value. This expands the findings in our earlier work (Howes et al., 2023), using this observational dataset with WRF-CAM5, wherein an unrealistically high and bimodal modeled spectrum of updraft strength correlated with an unrealistically high and bimodal N_{CLD}.

Increasing turbulence results in a marked increase in N_{CLD} over the SEA region as a whole (Fig. 3.6f, h). Mean cloud droplet number increases by 75-200 cm^{-3} in both $E3SM_{2W}$ and $CESM_{2W}$, with the spatial pattern of enhancement closely following the smoke plume. Cloud fraction does not show a clear increase over most of the SEA (Fig. 3.6b, d), as there are potentially buffering feedbacks and cloud adjustments from precipitation and cloud development after an increase in N_{CLD}. Turbulence thus presents the dominant sensitivity of N_{CLD} in this region, although N_{CLD} is also impacted by particle size and composition.

Photolytic aging, as discussed in section 3.3.1.2., strictly decreases diameter in $E3SM_{PH}$ and $E3SM_{PH\text{-}CON}$ compared to $E3SM_{BASE}$. Smaller particles require a larger supersaturation to activate into droplets, resulting in a decrease in N_{CLD} (Fig. A.5h, i). Particle hygroscopicity is also impacted by both the losses of OA and changes in sulfate formation. OA loss increases hygroscopicity of smoke particles, all else held equal, since it increases the fraction of the highly hygroscopic SO_4. Adding DMS may theoretically be expected to increase sulfate condensation and coagulation onto existing particles, and therefore hygroscopicity and N_{CLD} (and vice-versa with removing DMS), but both $E3SM_{NODMS}$ and $CESM_{DMS}$ show the opposite trends. Removing DMS tends to increase N_{CLD} significantly in $E3SM_{NODMS}$, and adding DMS slightly decreases N_{CLD} in $CESM_{DMS}$, primarily over the continent.

In E3SM, removing DMS reduces aerosol number concentration from the accumulation and Aitken modes in the BL by ~15% (not pictured). With a much smaller impact on total aerosol mass, the result is an increased mean diameter that then facilitates stronger activation into cloud droplets. This increased mean diameter is also seen to a smaller degree in the $E3SM_{NODMS}$ FT (Fig. 3.5j). The effect is not present in $CESM_{DMS}$, which shares MAM4 aerosol microphysics, suggesting the key difference is in the sulfate formation and chemical mechanisms of E3SM. This effect is nearly as large as that of turbulence, and merits closer examination in future work.

3.4. Conclusions

Biomass-burning smoke is evaluated in two prominent earth-system models, E3SM and CESM, against a broad range of in situ observations from the NASA ORACLES and CLARIFY-2017 aircraft deployments in the southeastern Atlantic Ocean. We separate the comparison by three physical regimes: the free troposphere, which can be thought of as a 'freely evolving' environment for smoke, absent of most other aerosol sources or cloud processing; the boundary marine layer, which contains significant new aerosol and precursor emissions as well as vastly more scavenging processes; and the warm clouds capping the boundary layer. The models are evaluated for baseline performance, as well as sensitivity tests to probe some of the processes evidenced by observations.

In the free troposphere, comparison was made by collocating aircraft flight paths with model cells. Both models show reasonable skill at representing the smoke number and mass concentration and exhibit a modest negative bias geometric mean diameter, likely driven by assumptions underlying the fire emissions inputs. Average regional FT smoke composition in both models overestimates OA and underestimates BC and SO_4 fractions.

By combining observations from both ORACLES and CLARIFY and using modeled age estimates, we were able to examine major trends in aging of FT smoke over a range of 4-12 days. Observations show a steadily decreasing mass ratio OA:BC from 10 to 5 over this time range that neither $CESM_{BASE}$ nor $E3SM_{BASE}$ capture. Mean diameter from observations, meanwhile, increases up to about 240 nm by 6 days' age, then decreases and plateaus near 215 nm from 8 days onward. Neither model represents this trend accurately, with both $E3SM_{BASE}$ and $CESM_{BASE}$ showing a noisy diameter increase over this time range when collocating with observations, and more clearly increasing with time as we zoom out to the whole region. The relative loss of OA over time is likely explaining some of this size change, combined with other aerosol microphysical processes such as coagulation and condensation. We examined the impact of photolytic losses of SOA, which has been suggested but irregularly studied in previous literature as a mechanism to explain some of these losses. We find that when including photolytic losses of SOA, especially when combined with a POA-SOA conversion scheme, E3SM is able to substantially replicate the observed aging trend in OA:BC. The photolysis also shifts the slope of the E3SM diameter trend towards stabilizing or decreasing with time, although the modeled age trend remains noisy. CESM$_{BASE}$ also contains the same photolytic SOA removal scheme but shows much less steep decreases in OA:BC over time, despite still showing stronger removal than E3SM$_{BASE}$. This is plausibly due to higher baseline SOA formation in E3SM than CESM. The photolytic mechanism tends to decrease both diameter and OA:BC going westward from Africa in both CESM$_{BASE}$ and E3SM$_{PH}$. The photolytic aging also brings the FT OA fraction in E3SM in line with observations, although there is a remaining underestimate of BC fraction. To our knowledge this is the first direct comparison of a model sensitivity study with this mechanism to in-situ observations and it provides promise for the inclusion of this photolytic mechanism in the upcoming version 3 of E3SM and understanding of SOA sources and sinks more broadly in BBA research. Composition and especially particle size have a large impact on the optical properties and radiative effects of smoke in the region and these provide promise for future work (Shinozuka et al., 2020).

Compared to the smoky FT, average aerosol composition in the BL has a sulfate fraction nearly 3 times higher across both ORACLES and CLARIFY observations. This emphasizes that even with enormous regional BBA emissions, the boundary layer aerosol cannot be assumed to simply be dominated by smoke. Sulfate in the marine BL is heavily influenced by precursor DMS emissions from the ocean. $CESM_{BASE}$, lacking DMS emissions, shows a lesser increase in the FT-to-BL SO_4 fraction (1.7 times) than does $E3SM_{BASE}$ (2 times), which does have DMS. Testing for sensitivity to DMS emissions, we removed DMS emissions from E3SM and added them to CESM. $CESM_{DMS}$ showed a stronger enhancement (2.2 times) and $E3SM_{NODMS}$ a weaker one (1.6 times) than their respective base models, a comparable magnitude of change for both. The FT photolytic scheme in $E3SM_{PH}$ also increased both the FT smoke SO_4 fraction as well as the enhancement factor in the BL, with $E3SM_{PH}$ showing an FT-to-BL increase of 2.1 times, and the POA-SOA conversion scheme increasing further to 2.3 times. Aside from salts, sulfate is the most hygroscopic species in marine BL aerosol in this region, and therefore it reinforces the need to represent aerosol chemical evolution for both sulfate and other species to reproduce hygroscopicity well.

The tendency for aerosols to activate into cloud droplets was largely underpredicted in both $E3SM_{BASE}$ and $CESM_{BASE}$, and across both ORACLES and CLARIFY observations. The activation ratio of N_{CLD}/N_{AER}, relating cloud droplet number to the aerosol number immediately below it, is 0.51-0.73 in observations, 0.37-0.55 in $E3SM_{BASE}$, and 0.18-0.47 in $CESM_{BASE}$. The observed turbulent updraft spectrum—especially in ORACLES—was substantially higher on average, and with a higher upper range, than either model. We doubled the updraft speed used in the cloud activation scheme in order to understand this sensitivity. We found that in both models, compared to both campaigns, there was a significant improvement in the number of below-cloud aerosols able to activate into cloud droplets, significantly reducing the bias in N_{CLD}. The E3SM$_{2W}$ ratio increased to 0.50-0.60, and CESM$_{2W}$ increased to 0.35-0.68. Cloud droplet number plays a large role in cloud albedo, lifetime, and rain rate, and therefore this is a crucial sensitivity in cloud modeling when the boundary layer has as large an aerosol loading as the SEA. We recommend that future modeling studies covering stratocumulus cloud properties, especially in heavily polluted regions, re-examine turbulence spectra in boundary layer schemes to reduce biases in cloud properties.

CESM and E3SM show themselves quite capable of accurately representing the large-scale horizontal transport of smoke and marine aerosols in the southeastern Atlantic, although there remains space for key process improvements, especially in the evolution of aerosol composition and the sensitivity of cloud droplet activation to updrafts. ORACLES and CLARIFY field campaigns combined provide an excellent opportunity to examine long-term smoke aging trends that are highly relevant to radiative effect uncertainties. Aging and turbulence schemes are a useful target for significant future work in efforts to accurately model aerosol-cloud-radiation interactions, especially in regions with historically high uncertainty in net radiative effects.

Acknowledgements

ORACLES is a NASA Earth Venture Suborbital-2 investigation funded by the US National Aeronautics and Space Administration (NASA) Earth Sciences Division and managed through the Earth System Science Pathfinder Program Office. Financial support for this work was provided by NASA ORACLES grant no. 80NSSC19K1463 and funds from the

Anthony and Jeanne Pritzker Family Foundation to Pablo E. Saide and DOE LASIC grant no. DE-SC0018272 to Pablo E. Saide. Pacific Northwest National Laboratory is operated for the U.S. Department of Energy by Battelle Memorial Institute under contract no. DE-AC05-76RL01830. The CESM project is supported primarily by the National Science Foundation. Computing and data storage resources, including the Cheyenne supercomputer (doi:10.5065/D6RX99HX), were provided by the Computational and Information Systems Laboratory (CISL) at NCAR which is a major facility sponsored by the National Science Foundation under Cooperative Agreement No. 1852977. We thank all the scientists, software engineers, and administrators who contributed to the development of CESM2.

Data Access

Observational datasets for ORACLES 2017 and co-located WRF-AAM plume age estimates are available through the NASA ESPO data archive: https://espo.nasa.gov/ORACLES/archive/browse/oracles/id14/P3 (last access: 10 March 2020; ORACLES Science team, 2020).

Observational datasets for CLARIFY-2017 are available through the CEDA data archive: https://catalogue.ceda.ac.uk/ uuid/38ab7089781a4560b067dd6c20af3769 (Facility for Airborne Atmospheric Measurements et al., 2017).

3.5. Figures for chapter 3

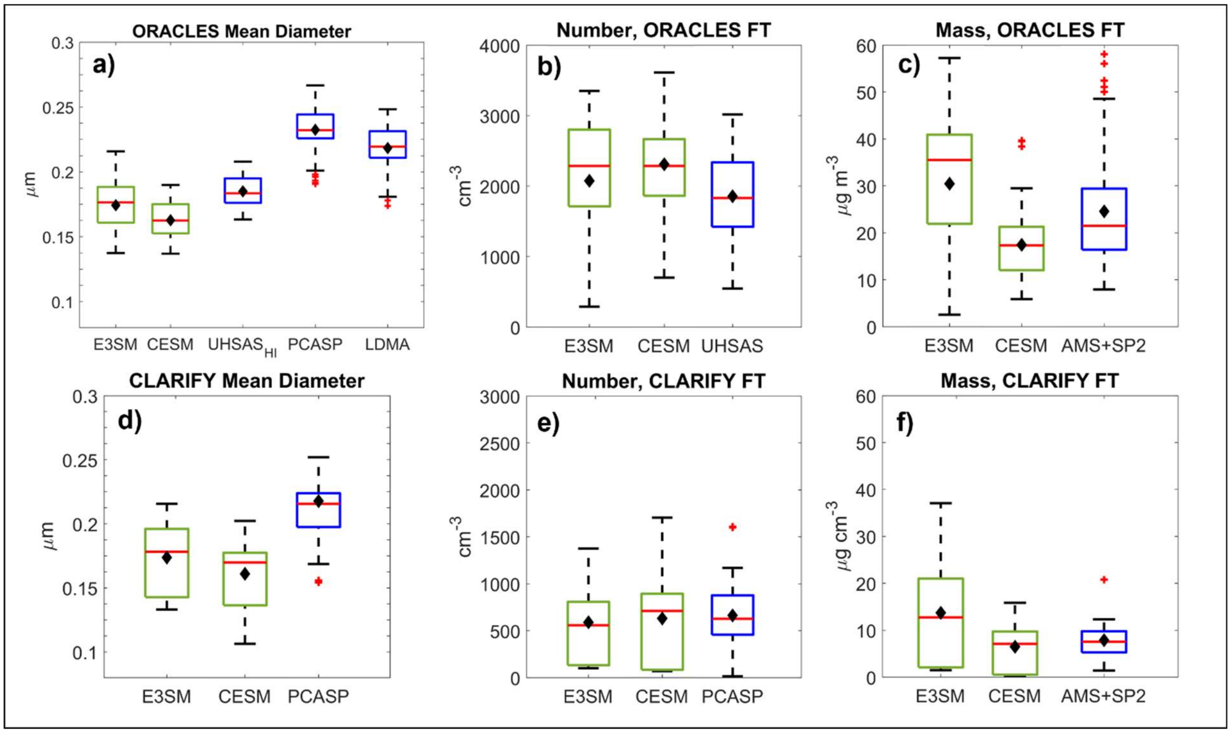

Figure 3.1: Smoke properties from models and corresponding observations in ORACLES and CLARIFY campaigns. (a, d) geometric-mean particle diameter in the accumulation mode; (b, e) number concentration, (c, f) mass concentration. Distribution means are given by black diamonds, medians are red horizontal lines, and red crosses are outliers (greater than 1.5 times the interquartile range beyond the box). Note the CLARIFY campaign only provided sizing data from the PCASP instrument.

	ORACLES	CLARIFY	E3SM - ORA	E3SM - CLR	CESM - ORA	CESM - CLR
Mean Diameter (nm)	185-232	218	174	174	163	161
Number (μm cm^{-3})	1860	663	2080	589	2450	678
Mass (μg cm^{-3})	24.6	7.87	30.4	13.7	17.4	6.95

Table 3.1: Medians of count-mean particle diameter, number concentration, and mass concentration in observations and base models, and the relative bias of the model values against the respective observations. Model columns are labeled according to the observation dataset they're being co-located with (e.g., E3SM – ORA denotes samples from E3SM$_{\text{BASE}}$ co-located with the ORACLES flight tracks, and E3SM – CLR is similar for CLARIFY data). Ranges are shown for ORACLES diameter because multiple instruments provided plausible measurements (UHSAS, LDMA, and PCASP). Note the CLARIFY campaign only provided sizing data from the PCASP instrument.

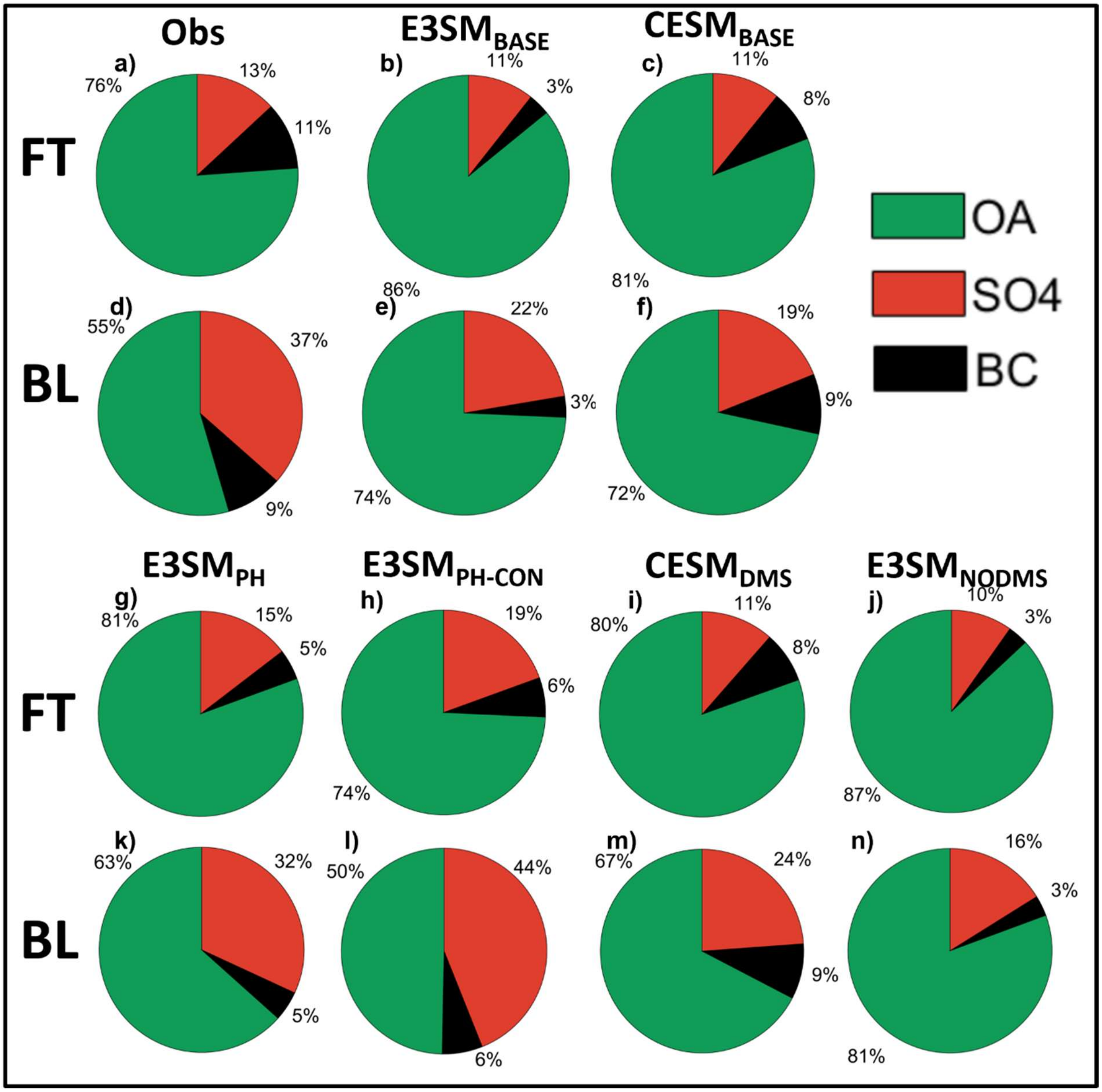

Figure 3.2: Aerosol composition breakdown in the FT and BL. FT figures (a-c, g-j) are selected from a minimum smoke concentration, while BL figures (d-f, k-n) are selected based on altitude. All figures combine samples from both ORACLES and CLARIFY campaigns. Species shown here are only the ones directly represented in both observations and models. Dust and chloride are excluded from model composition, while NO_3 and NH_4 are excluded from AMS observations.

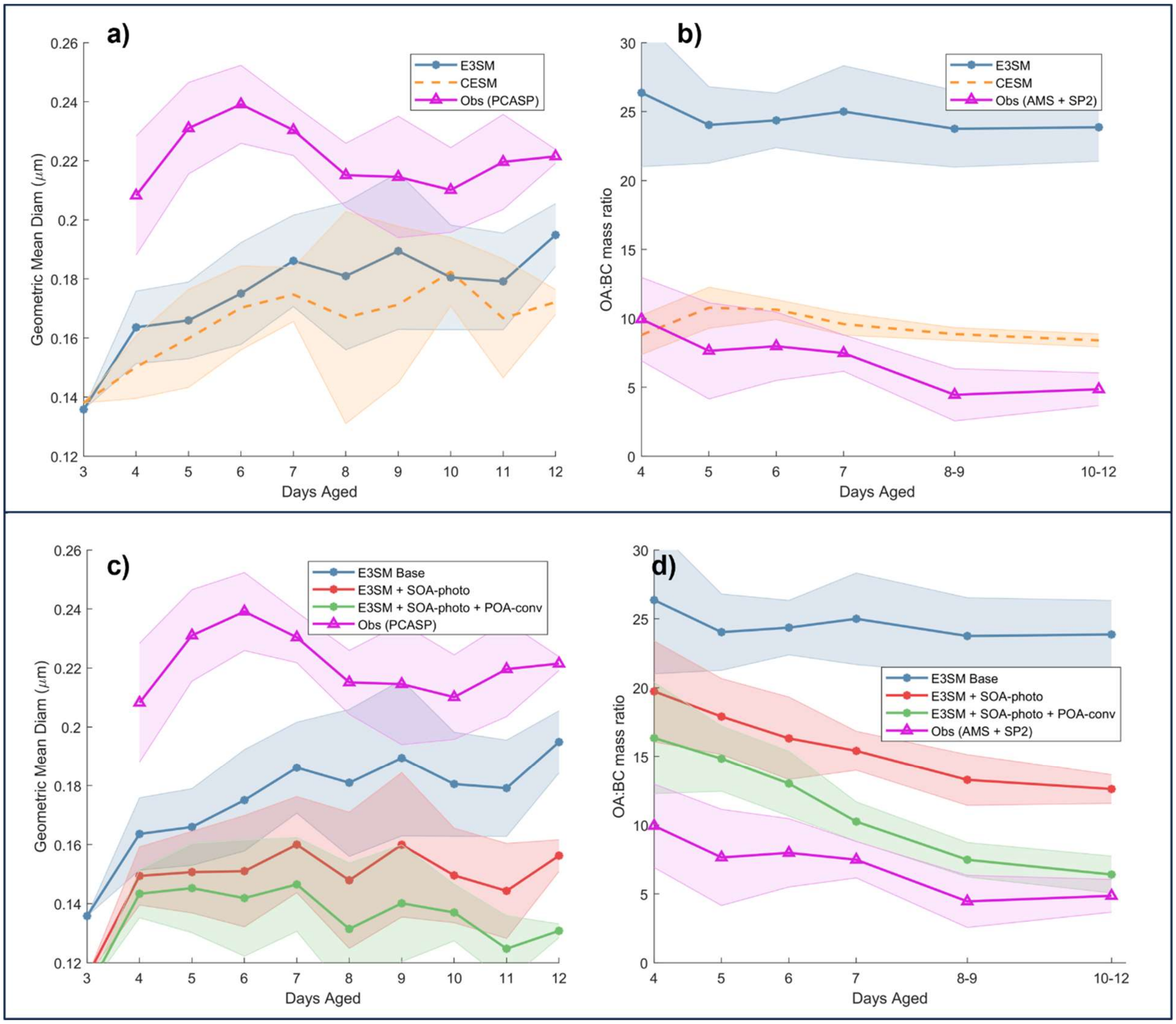

Figure 3.3: Aging trends in particle mean diameter (a, c) and organic aerosol to black carbon (OA:BC) mass ratio (b, d). Figures a-b compare trends $\text{E3SM}_{\text{BASE}}$ and $\text{CESM}_{\text{BASE}}$ against observations, while figures (c-d) show $\text{E3SM}_{\text{BASE}}$ and its sensitivities to changes in the photolysis scheme. Solid lines are the mean of values binned into each day or range, and the shaded region represents the standard deviation.

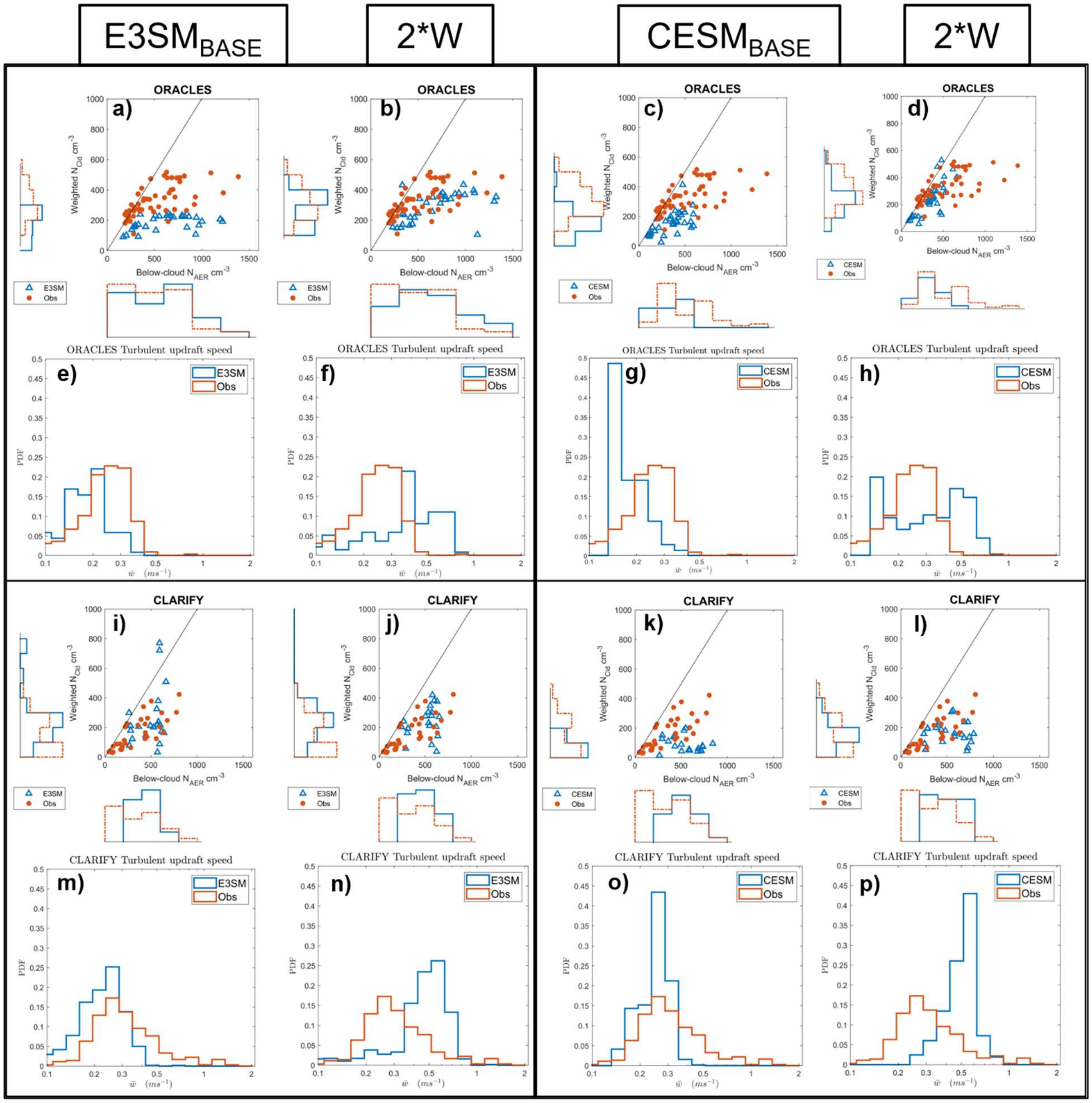

Figure 3.4: Aerosol-cloud activation efficiency and turbulence in ORACLES (top) and CLARIFY (bottom) in both observations (orange) and colocated models (blue). Columns 1 and 3 show baseline model performance in E3SM and CESM, respectively, for each quantity. Columns 2 and 4 show performance in the builds with doubled updraft strength in the cloud activation scheme, E3SM$_{2W}$ and CESM$_{2W}$ respectively.

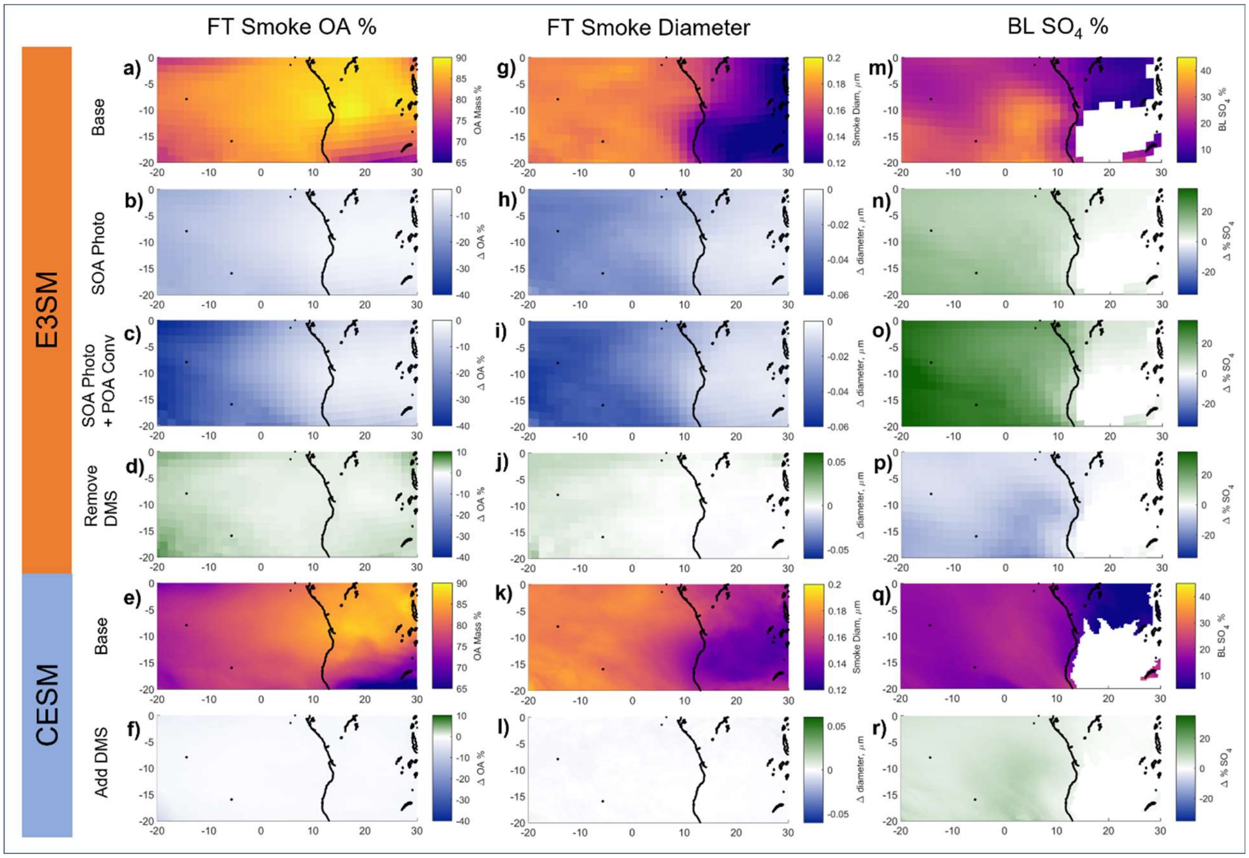

Figure 3.5: Maps of average smoke and aerosol properties through the SEA region during August 2017, showing both the base model values and the difference from the modified builds. Figs. a-f show OA mass fraction in the smoky FT. Base performance is shown for E3SM (a) and CESM (e), and differences against the base configuration for each model in (b-d, f). The same layout follows for geometric mean diameter of FT smoke (g-l) and boundary layer SO_4 mass fraction (m-r).

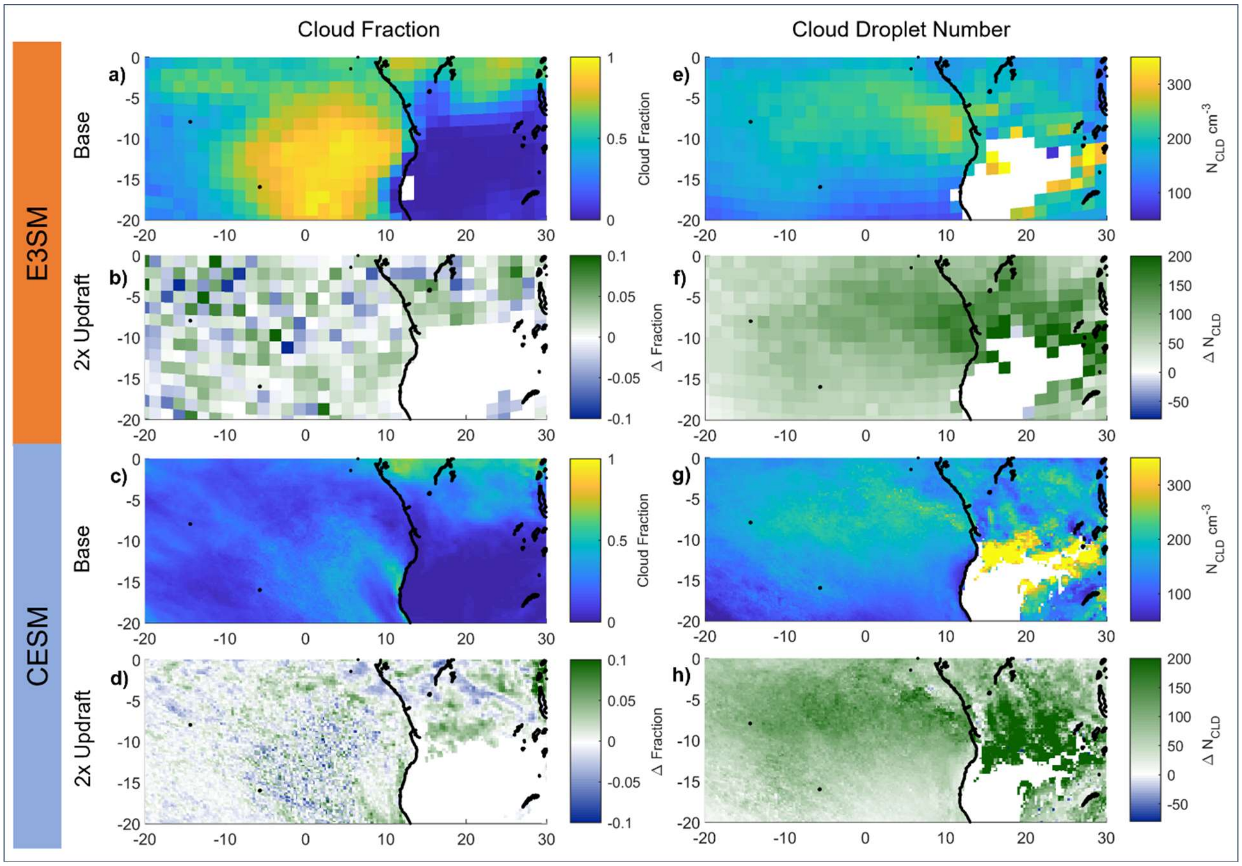

Figure 3.6: Maps of average cloud properties through the SEA region during August 2017, showing both the base model values and the difference from the modified builds. (a-d) show average low cloud fraction. Base performance is shown for E3SM (a) and CESM (c), and differences when increasing turbulence for each model in (b, d). The same layout follows for cloud droplet number concentration (N_{CLD}) (e-h).

Chapter 4

Application of weather radar to improve air quality modeling of wildfire smoke during the extreme 2020 US wildfire season

Abstract

Satellite measurements of fire radiative power (FRP) and fire radiative energy (FRE) are strongly correlated to emissions fluxes from wildfires. These measurements, however, are subject to signal errors due to fire obscuration from clouds or heavy smoke, pixel saturation or lack of non-burning references for very large fires, cloud-edge scattering false signals, and nighttime measurement uncertainties. In this work, we study the application of NOAA's NEXRAD Doppler weather radar observations of pyrometeors as a complimentary observation that also correlates with FRP. We compare radar-based FRP to that from the Regional ABI and VIIRS fire Emissions (RAVE) dataset to scale fire emissions in the record-breaking wildfire season of the western United States in September 2020, finding satellite-based emissions may be underestimated by a factor of up to 20 for the largest fires during the strongest burning. We use the WRF-Chem air quality model to analyze the impact of updated emissions on regional smoke transport. The initial large model underestimation of AOD against MAIAC is significantly reduced by the updated emissions, with the resulting regional AOD bias and normalized mean error against MAIAC AOD reduced by 14%, and mean bias reduced by over 50% during the peak burning period of 4-9 September. Surface $PM_{2.5}$, which threatens human health at elevated concentrations, are also better-represented with the scaled emissions. The model underestimation bias over most of the

run domain by 4 to 25%, depending on transport dynamics. Differences in smoke plume injection and transport in the model account for significant remaining model discrepancies. The broad extent and high quality of Doppler weather radar observations may significantly address underestimations in emissions from wildfires, with implications for modeling of historical aerosol-climate interactions, atmospheric composition, and especially air quality studies and early-warning systems during megafires.

4.1. Introduction

Smoke from wildfires presents a clear and ongoing concern to human health (Li et al., 2021b; Reid et al., 2016), and strongly influences earth's radiative balance (Das et al., 2021; Heinold et al., 2022) and atmospheric composition (Spracklen et al., 2007). The fundamentally chaotic nature of fires means they are difficult to predict and constrain, while the continuing increase in fire weather, frequency, and/or size of wildfires under a warming climate (Abatzoglou et al., 2019; Brown et al., 2023; Halofsky et al., 2020; Weber and Yadav, 2020) makes this understanding increasingly vital.

Emissions of smoke and gases from fires are often estimated by taking advantage of their correlation with measured of fire radiative energy (FRE) and fire radiative power (FRP) (Freeborn et al., 2008; Kaiser et al., 2012; Wiggins et al., 2020; Wooster, 2002). This is highly useful because satellite radiometers are able to accurately measure the relevant infrared emissions over huge swaths of land and on consistent time intervals (Freeborn et al., 2014; Xu et al., 2021). This precision and consistency allows researchers to construct emissions inventories for wildfires. Examples of these FRP-based emissions inventories include the Quick Fire Emissions Dataset (Darmenov et al., 2015) and the Regional ABI and

VIIRS fire Emissions (RAVE) (Li et al., 2022) among many others (French and Hudak, 2023). These emissions are then necessary inputs for modeling applications such as air quality forecasting (Ye et al., 2021) and assessment of regional and global climatic impacts of smoke (Howes et al., 2023).

Despite the great and ongoing advances in satellite sensing of fires, there remain currently unavoidable uncertainties and gaps in the emissions data, especially when dealing with very large, fast-changing, and dynamic wildfires. Clouds, including those generated by the fires themselves (Peterson et al., 2021), obscure the fires and may present false fire signals, and indeed are a major subject of research in active fire detection algorithm development (Giglio et al., 2006; Xu et al., 2010). The satellite sensor's pixels may also be saturated at a given intensity of radiation, so that FRP data may be filtered out entirely out of quality-assurance concerns or otherwise capped at the saturation intensity and temperature (Li et al., 2022; Xu et al., 2021). There are also uncertainties when a sensor is unable to locate a non-burning pixel as a reference, or during nighttime burning (Freeborn et al., 2022). These issues result in large underpredictions of smoke emissions during major fire events (Saide et al., 2015; van der Velde et al., 2021). While work on new and improved satellite radiometers is ongoing, there remains a fundamental gap in our ability to constrain fire emissions with existing satellite FRP data.

Considering these challenges, it is fruitful to consider complementary data sources to constrain fire activity and emissions, especially those which may constrain the hourly variability of large wildfires. Doppler weather radar, typically designed to observe weather phenomena, is one such example. Doppler stations cover most of the continental US and provide consistent, highly time- and spatially-resolved data, and are heavily quality-checked for their function in operational weather monitoring. Doppler radar's ability to sense clouds and rain droplets applies also to large ash particles around ~1 mm, also called pyrometeors (McCarthy et al., 2019). The fundamental sensing principle of Doppler radar for these large particles is not hindered by many of the issues presented to satellites, such as top-down cloud obscuration, signal saturation, or assumptions about land cover and fuel properties, although it presents unique challenges of its own (for example, ground clutter and topography, viewing angle, mixing of smoke from multiple sources, radar echoes, anomalous propagation, and unavailability in some regions). Previous work has shown that integrating radar reflectivity over a fire's pyrometeor plume correlates relatively well with its FRP (Saide et al., 2023). This opens up the possibility of using weather radar data as a supplement to satellite-based FRP sensing and emissions inventories to improve data gaps and especially to address underestimation of smoke emissions.

The 2020 wildfire season in the western US was one of the worst in recorded history, with a record-setting total burn area of at least 10 million acres (41,000 km^2), causing direct damages over $USD 19 billion and killing 37 people (Annual 2020 Wildfires Report | National Centers for Environmental Information (NCEI), 2024) as well as counterbalancing decades' worth of particulate emissions reduction and causing around $USD 7 billion in further climate damages (Jerrett et al., 2022). Many of these fires were extremely large and fast-growing, vulnerable to some of the satellite-based emissions gaps mentioned above. An ongoing drought coupled with summer weather in the region to create conditions ripe for fires (Keeley and Syphard, 2021). Many of the largest and most destructive fires in 2020 started within the week of September 4th-11th alone, while others such as the August Complex ignited in August and continued burning through September. This provides an excellent test case to apply weather radar analyses to improve emissions and resulting air quality modeling skill. In this work we estimate FRP from the weather radar observations of smoke from 18 of the largest fires in the western US in 2020 occurring in September. The extrapolated FRP is then compared with satellite FRP to scale up emissions, an attempt to account for this ‘missing’ FRP and resulting missing emissions. These emissions are then used in an air quality prediction system to assess potential improvements. In section 4.2 we first outline the processing and analytical principles used to generate the new emissions, as well as the modeling system used. We present preliminary results in section 4.3. We conclude by discussing the promise of this approach, including possible future research to discern the impacts of weather radar fire scaling in this run period and potential to expand its practicability.

4.2. Methods

4.2.1. Emissions Data and Processing

All weather radar data used in this study comes from the Next Generation Weather Radar (NEXRAD) network, a service operated jointly by the US National Weather Service, the Federal Aviation Administration, and the US Air Force (NOAA National Centers for Environmental Information, 1991).

Fires were selected for the largest burn area based on the Monitoring Trends in Burn Severity tool (MTBS) administered by the US Geological Survey, US Forest Service, and US

Department of the Interior. Fires chosen included those that burned at least 85,000 acres and with large satellite-observed fire activity in September of 2020. This resulted in the following 18 fires and fire-complex candidates: August Complex; Creek; North Complex; Pearl Hill/Cold Springs; Cameron Peak; Lionshead; Beachie Creek; Holiday Farm; Slater/Devil; Red Salmon Complex; Riverside; Archie Creek; Whitney; Dolan; Bobcat; East Fork; P515. For each fire, we selected the closest weather radar station that isn't substantially blocked by topography. Most nearby stations had clear lines-of-sight to the smoke plume at 6,000 ft above ground level, with one and two fires respectively at 10,000 or 3,000 ft above ground level. We use radar data for reflectivity, correlation coefficient (measuring particle sphericity), horizontal velocity, and spectrum width.

For each fire, weather radar data is filtered following the methods in Saide et al. (Saide et al., 2023). We manually examine the time- and space-resolved radar data, as well as GOES FRP for the given fire, to identify smoky and non-smoky periods and regions in a given interval. The non-smoke signals are mostly ground clutter and anomalous propagation. The partially-labeled data for each radar station is then run through a multiple-linear-regression machine learning model in order to remove non-smoke signals. The remaining signal is used to estimate "equivalent" composite rain (R) by using the maximum reflectivity (Z) over each column and applying the Marshall and Palmer (1948) relationship ($Z = 200\ R^{1.6}$). Composite rain is then integrated over the pyrometeor plume and used to estimate a timeseries of FRP following the power-law relationship in figure 2d of (Saide et al., 2023): $FRP=aX^b$ where X is the time-resolved integrated composite equivalent rain over the fire scene [$m^3\ h^{-1}$], and a and b are empirical coefficients with a=1.5, b=0.77.

We then compare the extrapolated FRP with RAVE FRP. RAVE is a recently developed high-resolution hourly emissions inventory based on combined satellite FRP products across low-earth orbiting and geostationary satellites (Li et al., 2022). We derive an hourly timeseries of scaling factors (e.g., Fig. 4.1) to apply to RAVE emissions based on the following: when RAVE FRP > radar FRP, the scaling factor is equal to 1 (i.e., use unadjusted RAVE FRP); when radar FRP < 500MW, the scaling factor is equal to 1; when radar FRP > RAVE FRP, the scaling factor is the ratio of Doppler / RAVE FRP. The first rule is applied because RAVE FRP is not expected to be overestimated, while weather radar FRP could be underpredicted in certain cases of topography blocking. The second is because weather radar FRP below 500 MW shows low correlation with satellite FRP, and satellite FRP is not subject to some of the issues associated with large fires mentioned earlier.

The emissions from each fire are scaled hourly based on this time series. The FRP scaling applies directly to emissions because emissions themselves are derived as the product of FRP with emissions factors such as in (Andreae, 2019). Of note, QFED (Darmenov et al., 2015) increased baseline emissions based on underestimated emissions factors per land type. The scaling factors by biome were as follows: 2.5 for Tropical Forest; 4.5 for Extratropical Forest; 1.8 for Savanna; and 1.8 for Grassland. Following this approach, our Doppler FRP scaling factor is applied multiplicatively on top of the land-based emissions factor increases. The result of this was per-fire, per-hour scaled emissions files that are used as inputs to our model. Some demonstrative time series are included in figure 4.8 for the two largest fires, the August Complex and Creek fires, showing the baseline RAVE FRP, GOES FRP, and the resulting FRP from radar scaling.

4.2.2. Description of Model

The model used in this study is WRF-Chem (Weather Research and Forecasting – Chemistry) version 4.2. This is a coupled atmospheric chemical transport model with a domain focused on the western US. WRF-Chem uses 4km horizontal resolution and 52 vertical layers covering an area from latitude 31 to 51N, and longitude 135 to 100W. The model uses RACM Chemistry including a VBS (volatility basis set) for secondary organic aerosols and heterogenous reactions. The model uses initial and boundary conditions from CAMS (Inness et al., 2019), anthropogenic emissions from the US National Emissions Inventory (NEI) version 2017 (US EPA, 2017), and biogenic emissions from MEGAN (Guenther et al., 2020). The model horizontal winds are nudged to the NCEP North American Regional Reanalysis at 32km (Mesinger et al., 2006). The analysis runs from 24 August 2020 through 22 September 2020, with the week of August runtime used as spinup. Plume rise dynamics were adjusted from the baseline Freitas scheme (Freitas et al., 2007) by limiting the fire radiative heat flux to 0.55 kWm^{-2} for all fuel types, in line with observations (Thapa et al., 2022) and increasing the fraction of emissions that are placed at the injection height to 85% (Ye et al., 2022). The output from this run is compared against a reference model run (labeled ‘reference’ in our results) using RAVE emissions with the same land cover type adjustment applied. Both runs are identical in configuration except for the Doppler-scaled fire emissions, providing a controlled sensitivity test. The run with scaled FRP from the weather radar is labeled ‘Doppler’ in the body of this text.

4.2.3. Observations Used for Model Evaluation

In training the machine learning algorithm for radar data, we referenced the Advanced Baseline Imager (ABI) on the Geostationary Operational Environmental Satellites – R Series (GOES-R) geostationary satellite FRP to identify most fire periods (GOES-R Series Program, 2019). Model AOD is compared observations from the Moderate Resolution Imaging Spectroradiometer (MODIS) (Justice et al., 2002) aboard the polar-orbiting Aqua satellite with the MAIAC aerosol processing algorithm (Qin et al., 2021) available at daily, 1 km resolution. Ground-level $PM_{2.5}$ from the model is compared against the OpenAQ dataset (Hasenkopf et al., 2015).

4.3. Results

We compile Statistics comparing AOD between the Doppler-scaled WRF-Chem run and the reference run for the 20-day period from September 1-21. Results show that there was generally an increase in modeled AOD with the Doppler-updated emissions averaged across the entire model domain, and over the entire evaluation period (Fig. 4.2). The increase was largest during the periods of highest AOD, without leading to significant overestimation in any period.

The reduction in bias and normalized mean bias (NMB) across the study range is large in the whole domain and is especially pronounced over California, where the largest fires took place (Fig. 4.3). The breakdown of statistics in figures 4.4-4.5 reflects this strong bias reduction. The regions of the state with the strongest bias—and the largest correction in the radar-scaled emissions simulation—correlate to mountainous areas with large fires, such as the Creek Fire and August Complex. The absolute mean bias in AOD was reduced by 0.05 averaged over the run period (range of AOD change: -0.12 to +0.37). Normalized mean bias is reduced by 16% on average (range 4 to 46) and normalized mean error of AOD is reduced by 14% on average (range: 0% to 38%). The period of 5 to 9 Sept, where ignitions of enormous fires across the entire west coast caused a huge spike in whole-domain AOD, exhibits a more than 50% reduction in mean bias.

It is informative to examine the emissions scaling for the a few of the largest fires in this study, the August Complex, Creek, and Red Salmon fires (Fig. 4.1). The factors driving satellite FRP underestimation are large for the largest fires, and they emit the most smoke overall, therefore these represent the most useful examples for improvement of total emissions. There are periods of several days in both the August and Creek fires where FRP (and therefore emissions) are underestimated by a factor of 5-10, and several intervals underestimated by a factor of ~20 or more. Based on FRP in figure 4.1, the August Complex has strong sustained emissions through the entire period of 4-18 September, while the Creek fire is mostly burning from 4-8 September. The Red Salmon fire represents another case, where emissions are generally highest from RAVE throughout the burning period, with little correction impact from the radar.

When comparing the Doppler run with the reference run, Pearson correlation (r) between the daily timeseries MAIAC AOD and model AOD increased from 0.87 to 0.92 in the whole domain, along with an improved coefficient of determination (R^2) from 0.03 to 0.52 (Fig. 4.2b). However, correlation between modeled and observed AOD is not uniformly improved by the updated emissions. The level of statistical improvement varies by region, with the CA/NV region showing an improved correlation but reduced R^2, and the inverse being true in PNW (Figs. 4.6-4.7). The Intermountain West (IMW) doesn't show large improvement, but this region had few large fires compared to the west coast (Fig. 4.8).

This is related to the highly spatially-heterogeneous nature of the fire trends, as well as relevant model processes and structural biases. For example, AOD in PNW in particular shows a sharp divergence between observed and modeled AOD in both model configurations around 14 September and a reduced correlation in the Doppler run. Several mitigating factors make it difficult to definitively attribute this feature to biases in our model or emissions calculations. First, smoke from the PNW during this period of 10-14 September was partially advected north and west over the ocean, and later recirculated back over the west coast. The model domain was expanded further to the west during preliminary design to accommodate this possibility, but a segment of the smoke plume still ran into the model boundary. Model boundary conditions from CAMS do not include updated smoke emissions, only reanalysis, so this excess smoke is permanently lost in the model. Another important factor is that three large fires in Oregon, the Slater/Devil, Holiday Farm, and Archie Creek fires, were all being covered by the KMAX Doppler station. Due to unknown issues, no data from this radar is available from 14 to 23 September 2020. As a result, we simply used unscaled RAVE emissions from the 14th onwards and there is little change in AOD in the Doppler run after that point. As the model sensitivity tested here is also focused on fire emissions, a reduction of bias near fires with little impact on bias downwind would result in decreasing correlation. There is also evidence of smoke optical properties changing significantly with age to become more efficient at extinction (Saide et al., 2022), which our model does not represent. This divergence of smoke properties over time would tend to decrease correlation between modeled and observed smoke AOD. Estimates of correlation and variability on small time scales are also subject to meteorological differences and smoke plume injections altering transport behavior, which are ongoing research targets in other work.

In the cases of the two largest fires, the August Complex and Creek, it is useful to examine the per-fire AOD differences. For the August Complex, the Doppler run drove a large increase in AOD over most of the run period, especially during the strong burning of 9-14 September (Fig. 4.9a). The Doppler run has a high AOD compared to MAIAC before the 8th, and biases low afterwards. The overestimate correlates with the peak radar-based FRP around 4 September in the Doppler run (Fig. 4.1a) and may necessitate further filtering in the emissions scaling if this jump is not realistic. In the Creek fire (Fig. 4.9b), the high AOD through 18 Sept is disconnected from the relatively modest burning from the 9th onwards (Fig. 4.1b). In combination with the nearly identical reference and Doppler model runs from the 12th onwards, this suggests that most of the smoke present is being advected from other fires, such as the nearby August Complex, rather than emitted locally. The remaining low bias could be attributed to low smoke injection and advection biases in the model. Of note, the large drop in AOD around 8-9 September in the August Complex fire is likely due to missing MAIAC data, as the smoke was so thick (AOD > 5) that it is removed during data processing. The model AOD is sample collocated with available observations, so this drop appears in the models as well regardless of their emissions.

We also analyze ground-level $PM_{2.5}$, which is a common quantity used to analyze threats to human health from poor air quality. The mean daily bias decreases over the domain from -18 μg m^{-3} in the reference run to -10 μg m^{-3} with Doppler scaling (-25% to +2% normalized mean bias). In CA/NV and PNW, surface $PM_{2.5}$ is increased in both across the study period as expected (Fig. 4.9).

The Doppler run has an increased absolute bias in CA/NV from +0.22 μg m^{-3} to 1.44 μg m^{-3} (but normalized mean bias decreasing in magnitude from -22.5% to +18.0%). The Doppler run both increases early overprediction $PM_{2.5}$ until 10 September and decreases the underestimate from then onwards. This is reflected in a reduced Pearson correlation r=0.36 in the Doppler run compared to 0.58 in the reference run. During peak loading 10-18 September, the normalized mean bias is reduced from 49% to 32%. The overprediction in the first week or so may be attributed to underestimated injection fraction again; if smoke emitted nearby remains in the boundary layer, it would both increase local $PM_{2.5}$ concentrations during the burning period, and would underestimate smoke being advected to the region from elsewhere through the FT. There is also evidence that smoke $PM_{2.5}$ formation may be more volatile than the model represents, and that organics remain in vapor form until the smoke rises and cools higher in the troposphere (Pagonis et al., 2023). This would serve to reduce surface PM loading without changing overall emissions mass or column AOD, on average.

In the PNW, the surface $PM_{2.5}$ follows a similar pattern as the PNW AOD. Doppler emissions sharply reduce bias in $PM_{2.5}$ in the region from -36.8 μg m^{-3} to -28.2 μg m^{-3} (-25.5% -10.1%). During peak loading over 10-18 September, the normalized mean bias is reduced from 55% to 40%. The improved modeled $PM_{2.5}$ still largely retains the plateauing $PM_{2.5}$ and large underprediction past 12 September. The resulting correlation with observations improves from 0.79 in the reference run to 0.83 in the Doppler run. The aforementioned smoke losses at the model boundary and especially the outage of the KMAX radar station both limit modeled smoke in the PNW. Underestimates of smoke FT injection elsewhere could also lead to underpredicting smoke transported northwards from other burning regions when the fires have died down locally.

4.4. Conclusions

These results show promise for significant improvement in smoke emissions modeling. This stands to benefit several applications of high-resolution atmospheric and fire modeling efforts. Air quality forecasting and attribution studies on human health and exposure rates may be improved since actual emissions amounts have wide uncertainty and vary substantially between emissions datasets. More accurate fire emissions will also assist in isolating other model uncertainties and concerns, such as plume injection height and transport. Radiation budget and climate sensitivity studies will also be improved by more accurate emission estimates of biomass-burning species. With superb spatial and temporal resolution compared to satellites, weather radar data is a helpful complementary dataset to help cross-validate observations of FRP between different platforms. Such cross-validation between platforms is a necessary and important feature of emissions inventory development.

When applying hourly Doppler-based emissions scaling, AOD bias is strictly reduced over the model domain, with an average reduction in bias of ~15% and up to ~50% reduction during the strongest total burning period of 4-9 September. In the CA/NV and PNW regions, there is also a smaller negative AOD bias during the highest burning periods, with much of the remaining bias suggesting insufficient transport from other burning regions as well or underestimated model smoke extinction.

We also analyze the model performance differences on a fire-by-fire basis. Large fires especially have large potential for improvement, as a similar linear scaling over a larger burning region will result in a larger increase in total smoke mass emissions. The August Complex fire region showed an increased AOD over the entire run period of ~0.5, reducing absolute error for most of the burning. The largest reduction in error was during the peak AOD of 9-14 September, which is a promising sign for this method as applied to large fires. The Creek fire also had improved AOD during most of its strongest burning period (6-12 September), with minimal improvements after that period correlating with limited actual burning. Thus, smoke transport from other fires (such as August, nearby) may again explain the ongoing high AOD through 17 September, rather than Creek smoke emissions.

We analyze $PM_{2.5}$ to understand a quantity more relevant to human exposure and health risks as well as to aid in understanding smoke plume injection and transport. The scaled emissions reduce the average underestimation bias of modeled surface $PM_{2.5}$ by 33% in CA/NV and by 27% in PNW during the highest loading periods that are most harmful to human health (10-18 September). The Doppler run overestimates $PM_{2.5}$ in early September in CA/NV, possibly driven by a low injection rate keeping smoke near the burning regions or temperature-sensitive OA volatility decreasing surface $PM_{2.5}$ concentrations in the real world but not the model. In PNW, the Doppler run is a strict improvement over the reference run, reducing the negative bias, but still exhibits a large negative bias for most of the highest loading period. This is likely related to both Doppler data outages limiting the fire scaling and, as the fires decreased past 15 September in the region, model underestimates of smoke transport from fires further away.

Analysis of smoke transport and timing in WRF-Chem is ongoing, although scaling the emissions using Doppler radar has led to large improvements in model skill. WRF-Chem has been shown to variously underestimate and overestimate the frequency of smoke injections into the free troposphere from wildfires (Thapa et al., 2022; Ye et al., 2022), a factor which may explain much of the remaining model biases. An overpredicted fraction of smoke in the BL would lead to an overprediction of surface-level $PM_{2.5}$ in the model, even if emissions levels were perfect. This is a key analysis for future work, as a focus exclusively on injection rates or emissions in order to match observations may address the bias without addressing an underlying issue. The models used in this work are adjusted for this, but a bias remains and expanded combined analysis would benefit the field.

Automating much of the radar FRP derivation process will also greatly improve practicability of our radar scaling methods. Most of the steps outlined here require manual identification and best-judgment of fire locations, boundaries for Doppler data extraction, processing, and supervision of the machine learning training process, as well as calculating and applying scaling factors on a fire-by-fire basis. If many or most of these steps could be automated, this approach could be applied and evaluated across multiple months and multiple years' fire seasons and will aid its benefit to operational air quality forecasts.

Acknowledgements

Funding for this work was provided by NSF grants 2013461 and 2238338, NASA grants 80NSSC18K0629 and 80NSSC20K1650, NOAA grant NA18OAR4310107, and by funding from the Anthony and Jeanne Pritzker Family Foundation.

Data Availability

NEXRAD Doppler weather radar is available for download from NOAA/NCEI online at https://www.ncei.noaa.gov/products/radar/next-generation-weather-radar (last access: 4 March 2024; NOAA National Centers for Environmental Information, 1991).

RAVE fire emissions data is available from the creators (Li et al.) upon request (last access: August 2023; Li et al., 2022).

GOES-17 ABI FRP is available online at doi.org/10.25921/tvws-w071 (last access: 2 February 2023; GOES-R Series Program, 2019).

OpenAQ air quality data is available for download online at https://www.openaq.org and via API at https://github.com/openaq (last access: October 2023, Hasenkopf et al., 2015).

4.5. Figures for chapter 4

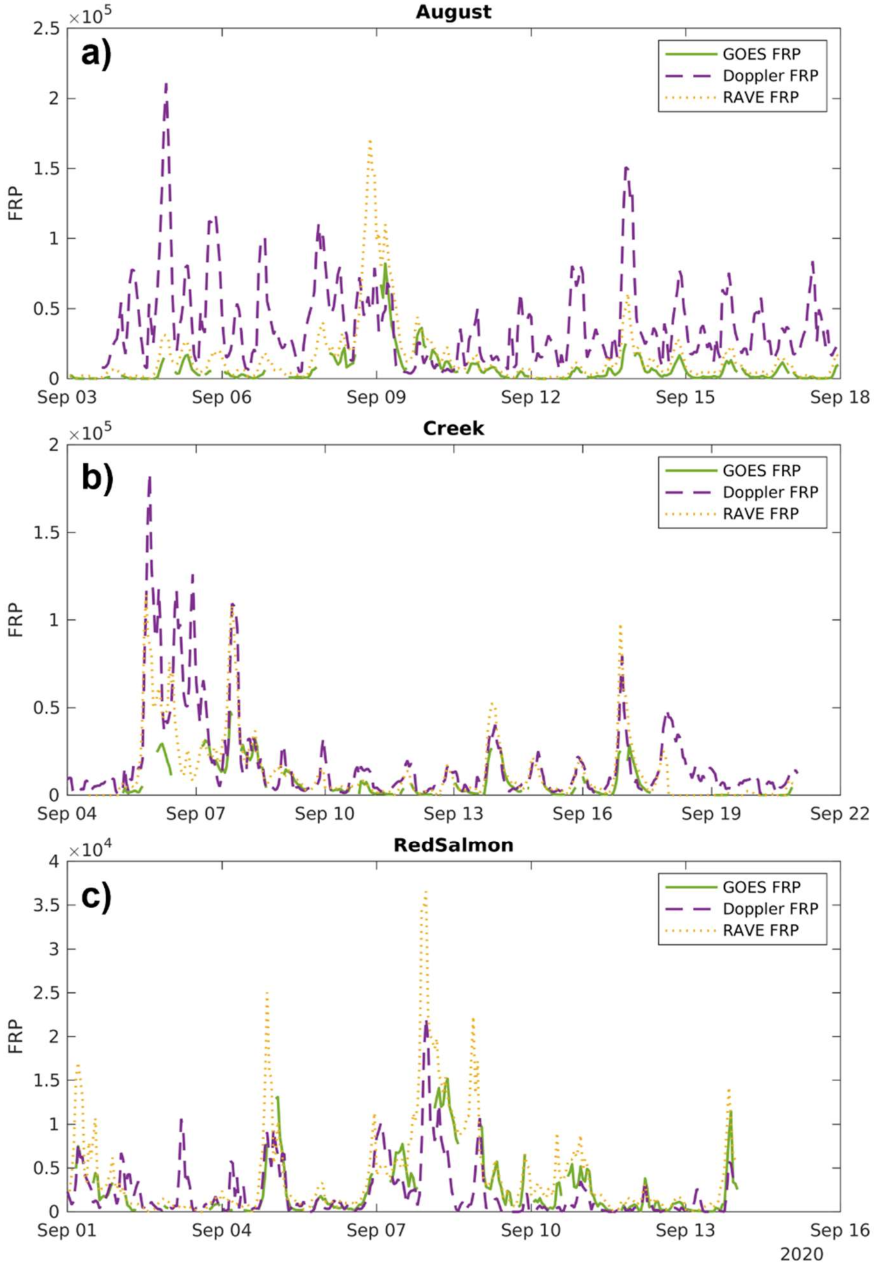

Figure 4.1: Time series of satellite and radar-based FRP from (a) August Complex (b) Creek Fire and (c) Red Salmon Fire in September of 2020. FRP's shown are from GOES-R ABI Geostationary (green), Doppler radar estimation (purple, dashed) and RAVE (yellow, dotted).

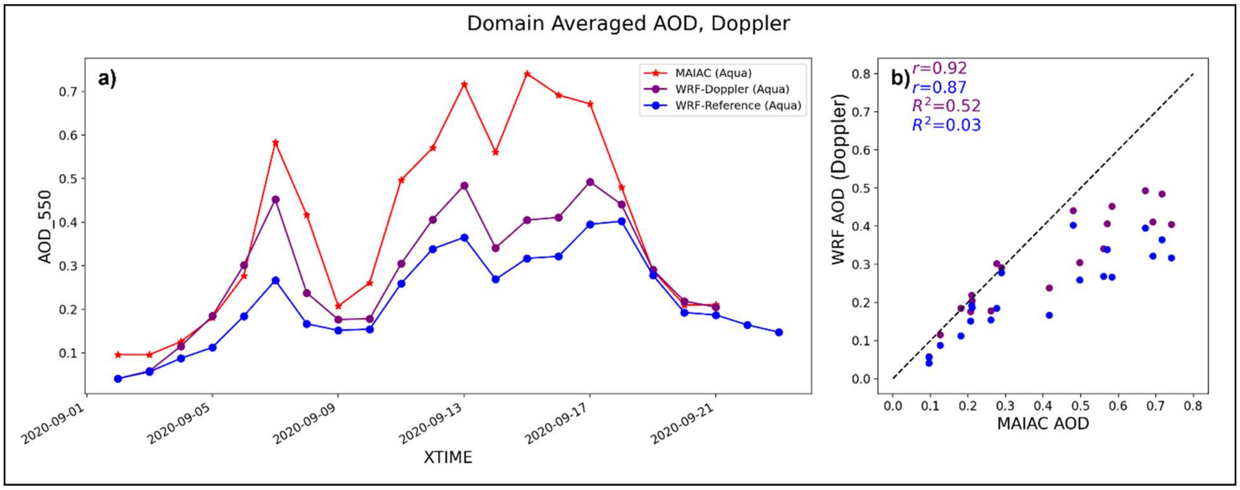

Figure 4.2: (a) Time series of daily mean AOD for MAIAC (red), the reference WRF-Chem run (purple) and Doppler run (blue); (b) scatter plot of daily-mean values from the Doppler run compared to MAIAC AOD. All point values are shown as a daily average for the entire model domain.

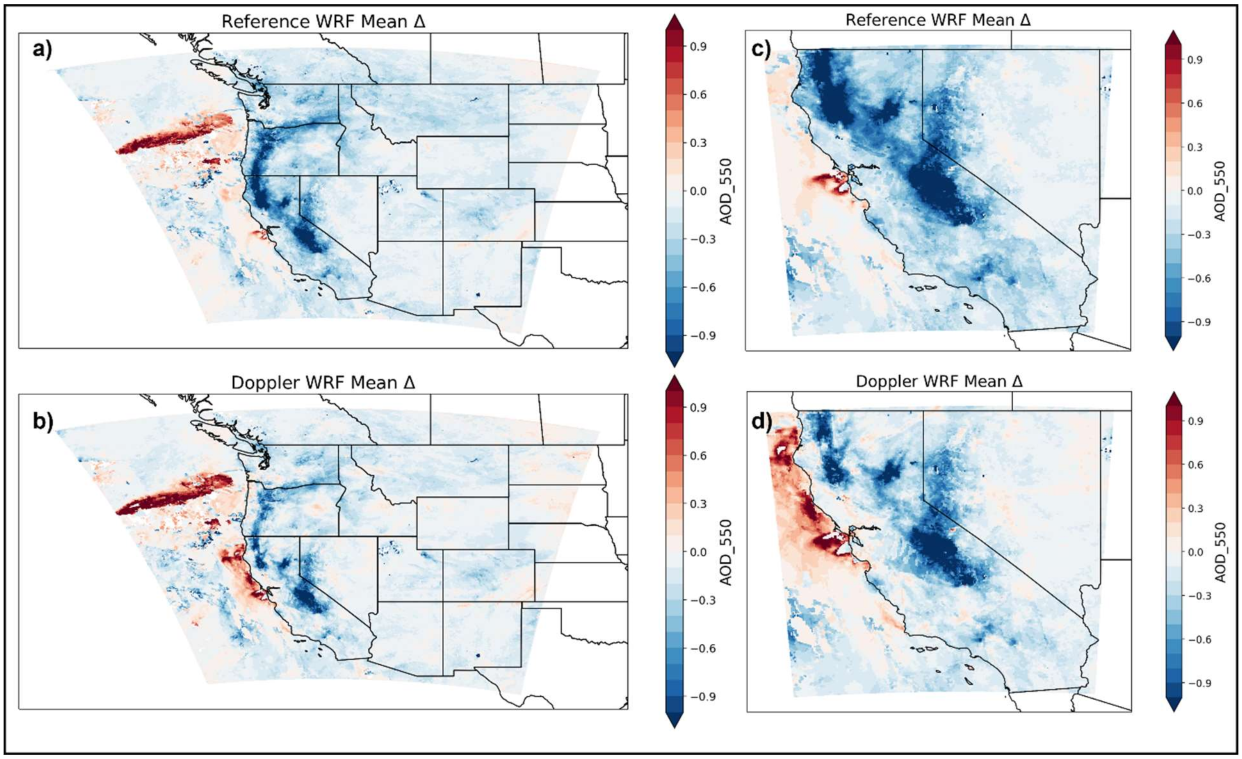

Figure 4.3: Maps of simple bias in AOD over the whole domain (a-b) and zoomed in showing CA/NV (c-d). The top row shows values from the reference WRF-Chem run, and bottom shows the Doppler WRF-Chem run, with a strong overall decrease in the largest bias regions.

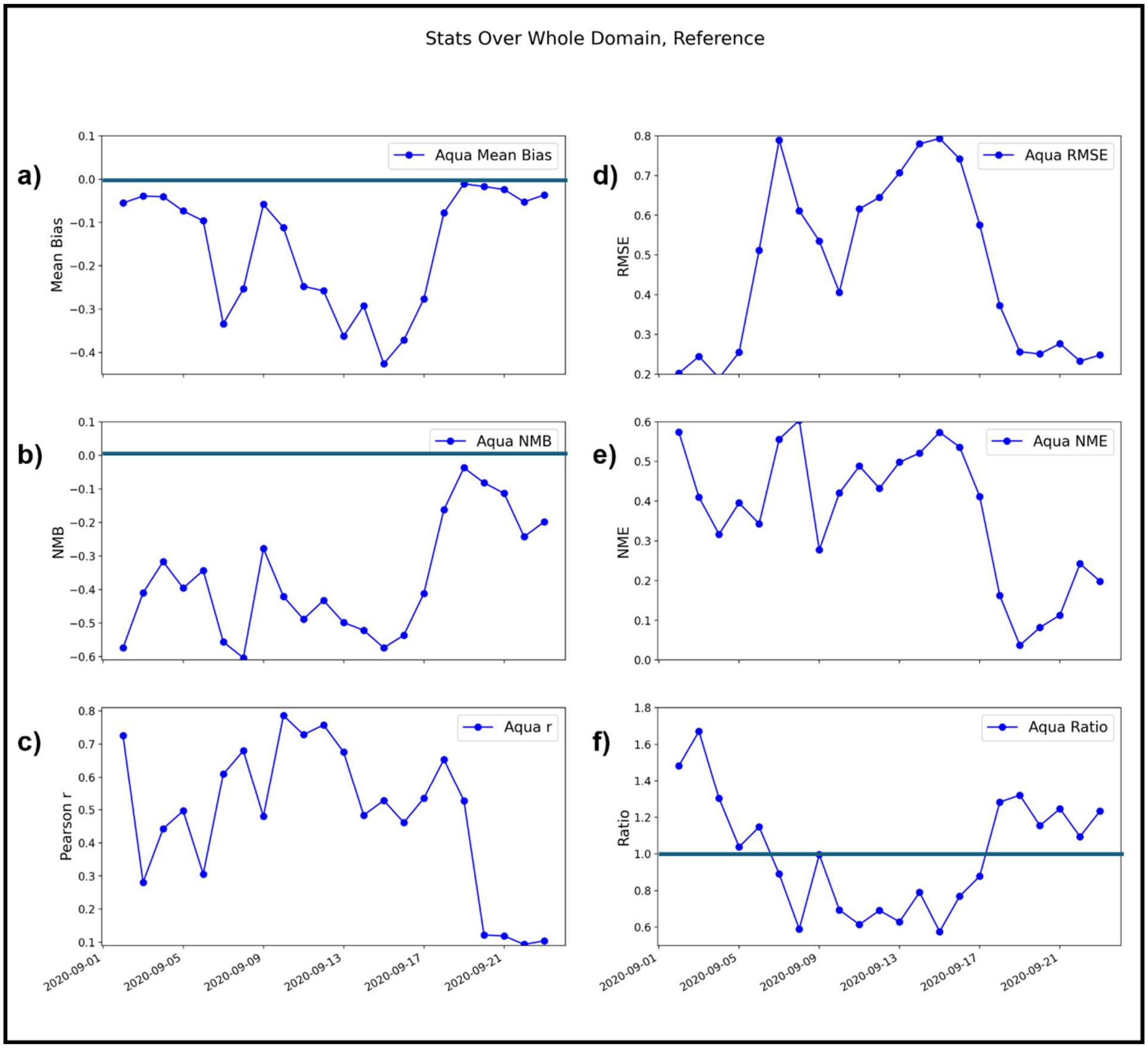

Figure 4.4: Time series of whole-domain AOD statistics comparing the reference WRF-Chem run and AOD from the MODIS instrument on Aqua, using the MAIAC algorithm. Plots show (a) mean bias against observations; (b) normalized mean bias; (c) Pearson r correlation coefficient; (d) root-mean-squared error; (e) normalized mean error; (f) ratio of modeled to observed AOD value. Horizontal lines are superimposed at the level of unity—a bias of zero, or a ratio of 1 between model and observations.

Figure 4.5: Time series of whole-domain AOD statistics comparing the Doppler WRF-Chem run and AOD from the MODIS instrument on Aqua, using the MAIAC algorithm. Plots show (a) mean bias against observations; (b) normalized mean bias; (c) Pearson r correlation coefficient; (d) root-mean-squared error; (e) normalized mean error; (f) ratio of modeled to observed AOD value. Horizontal lines are superimposed at the level of unity—a bias of zero, or a ratio of 1 between model and observations.

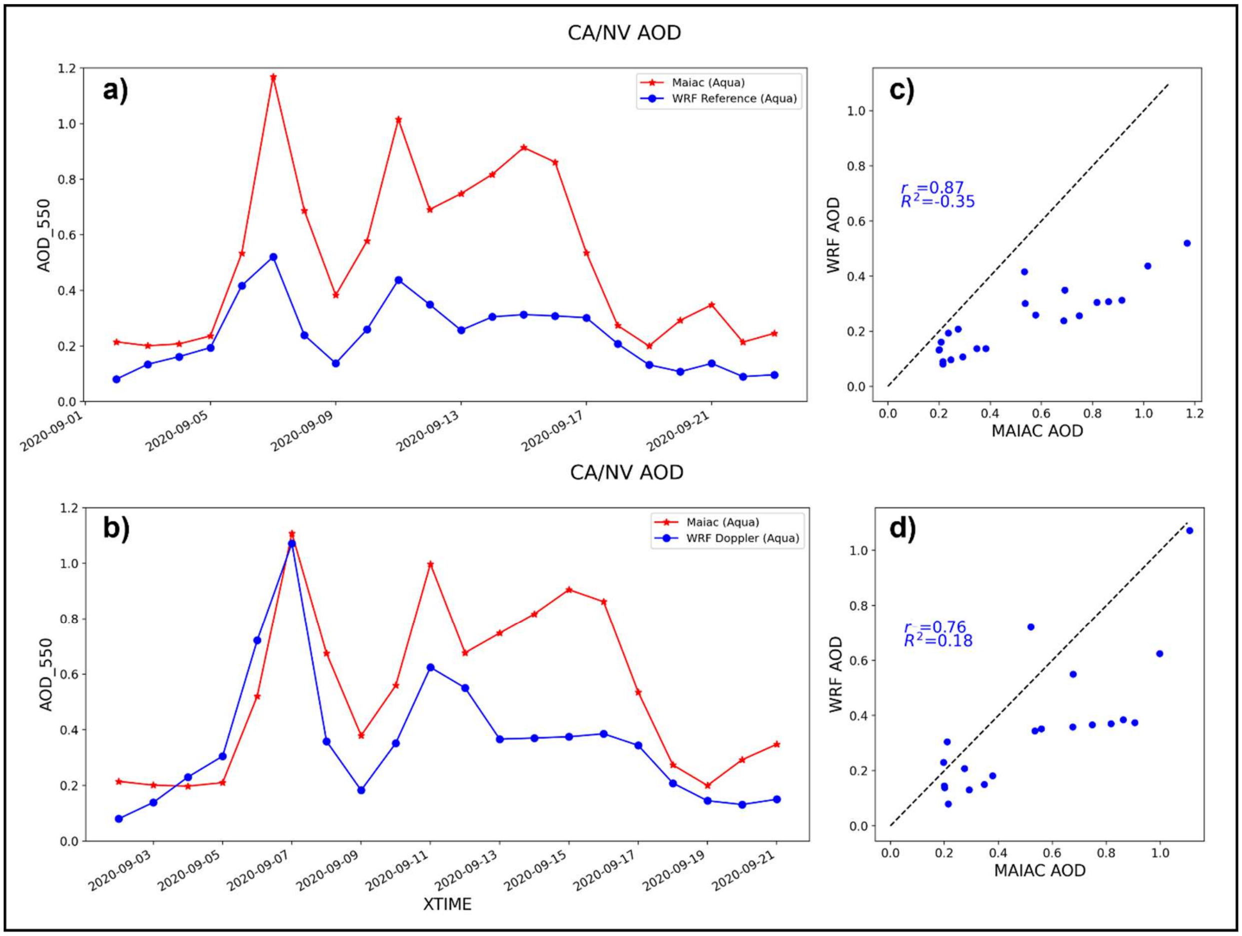

Figure 4.6: Time series (a-b) and scatter plots (c-d) of daily mean AOD for both the reference WRF-Chem run (top) and Doppler run (bottom). Values are shown for only the CA/NV region.

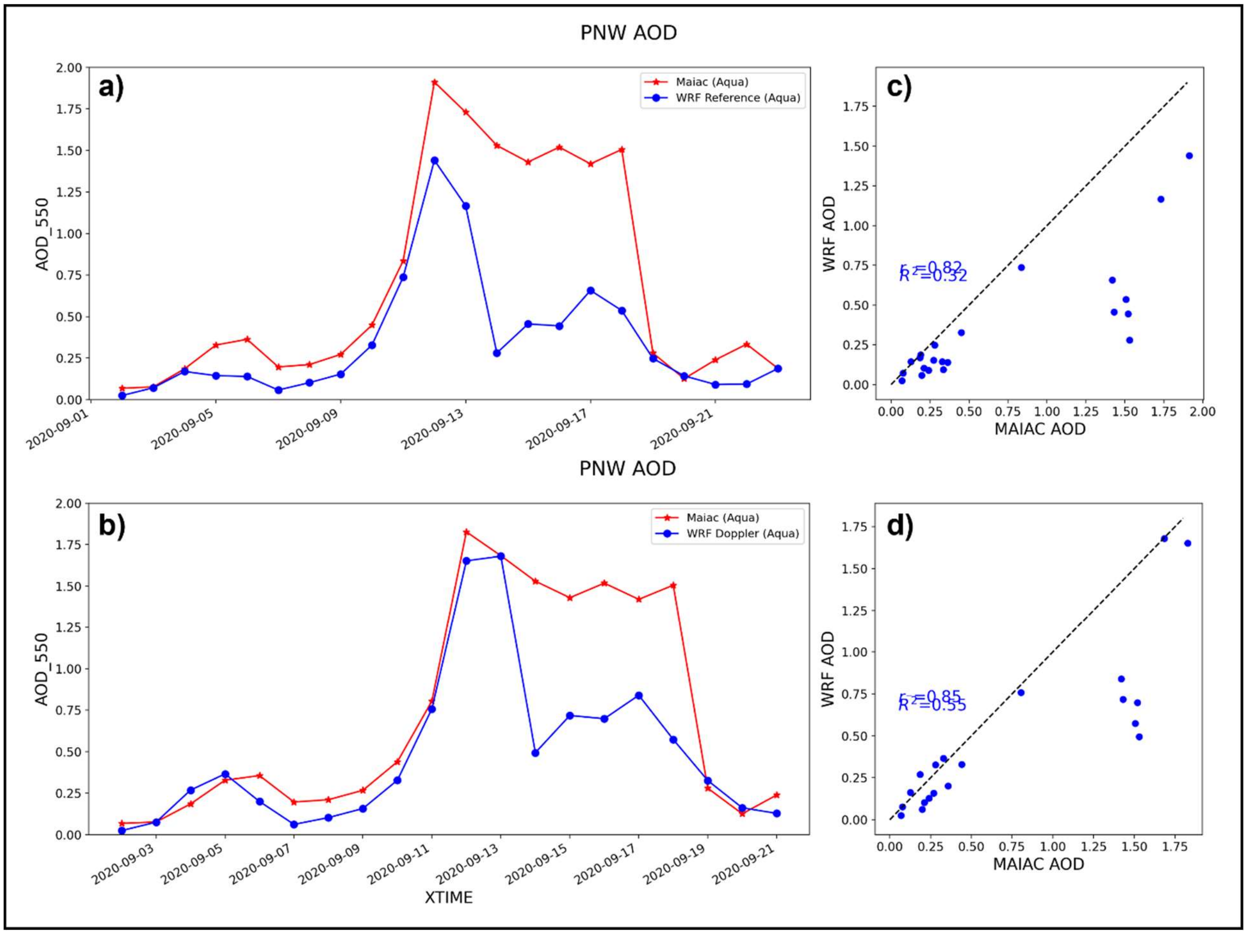

Figure 4.7: Time series (a-b) and scatter plots (c-d) of daily mean AOD for both the reference WRF-Chem run (top) and Doppler run (bottom). Values are shown for only the PNW region.

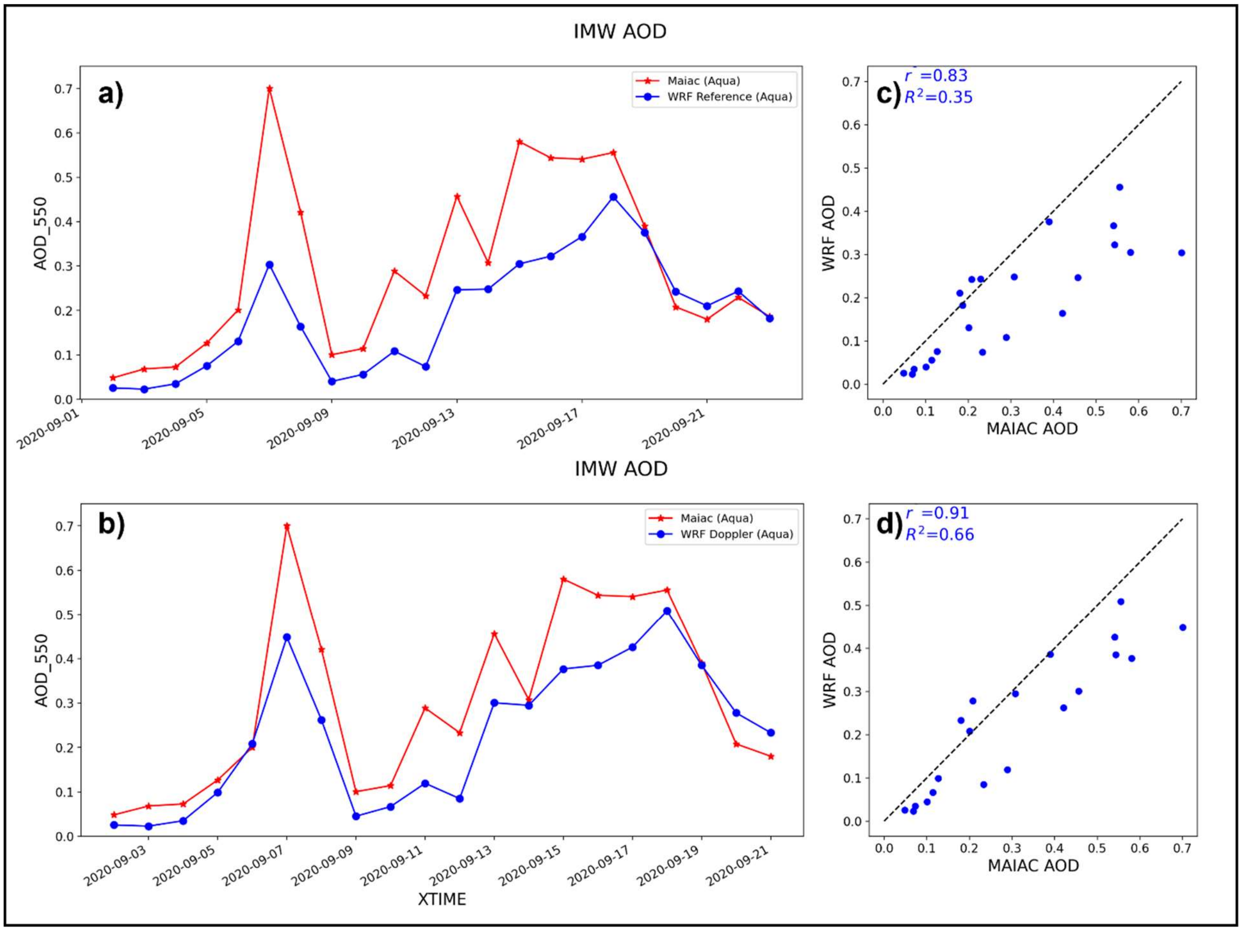

Figure 4.8: Time series (a-b) and scatter plots (c-d) of daily mean AOD for both the reference WRF-Chem run (top) and Doppler run (bottom). Values are shown for only the IMW region.

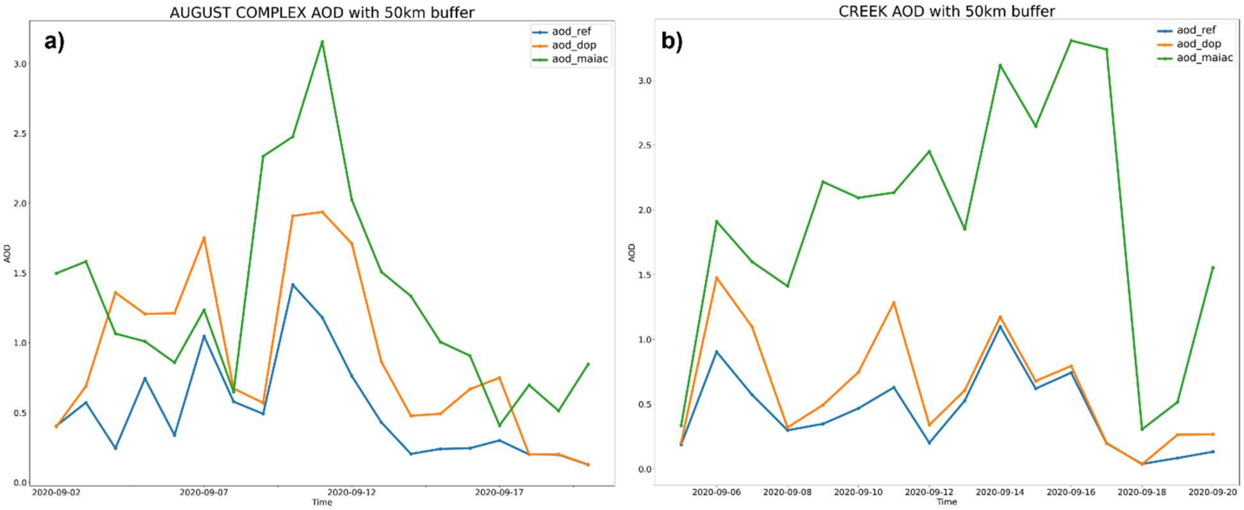

Figure 4.9: AOD from reference WRF-Chem (blue), radar-scaled WRF-Chem (orange) and MAIAC satellite observations (green) for the (a) August Complex and (b) Creek fires.

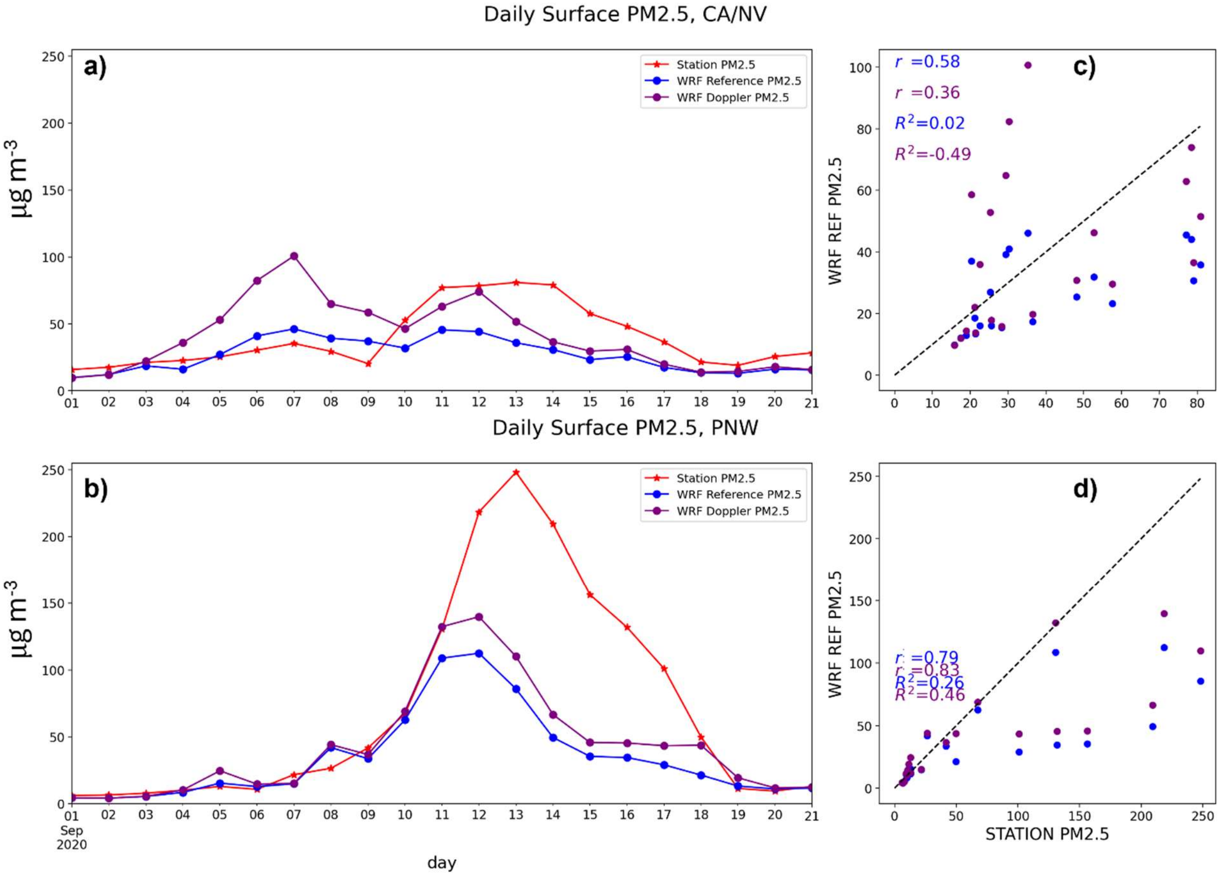

Figure 4.10: Surface $PM_{2.5}$ in the reference model (blue), radar-scaled model (purple), and OpenAQ observation stations (red). $PM_{2.5}$ is shown as a time series (a) and scatter plot (b) against observations for the California/Nevada (CA/NV) combined region (a-b) and Pacific Northwest (PNW) region (c-d).

Chapter 5

Thesis conclusions

Smoke and aerosols represent an enormous source of uncertainty in climate projections as well as an ongoing and increasing threat to public health. My research has been aimed at improving the micro- and macro-physical representation of smoke, its emission, and its interactions with the atmosphere. The impacts of this work overlap the fields of air quality research, high-resolution smoke plume modeling, atmospheric chemistry, and multifarious aerosol impacts on climate.

In Chapter 2, I analyzed the representation of smoke and its interactions with clouds in WRF-CAM5 to better constrain aerosol properties and aerosol-cloud-radiation interactions, towards a reduction in radiative forcing uncertainty. I compared model data against a very broad range of instruments from three overlapping campaigns in the southeastern Atlantic region in August 2017—ORACLES, CLARIFY, and LASIC. The wide range of spatial observations between the campaigns gave unique insight into long-term smoke evolution for model comparison. I found that the model shows a strong ability to represent smoke transport and placement in the atmosphere over the course of a month, even without strict meteorological nudging. I analyzed the smoke properties in the free troposphere, showing observational evidence of aging that is missing from the model despite an accurate overall picture of smoke properties. In the marine boundary layer, I found that WRF-CAM5 is often failing to scavenge smoke efficiently during the burning season and is underestimating the population of the Aitken mode quite substantially. In addition, the composition of observed aerosol in both the BL and FT was observed to differ quite substantially—based on hygroscopicity—across the accumulation mode, pointing at differential composition by size in the accumulation mode. WRF-CAM5 (and indeed most ESMs) cannot capture this as they use total-internal-mixing assumptions in their aerosol schemes. Examining aerosol-cloud interactions, I analyzed biases in the modeled activation of aerosols into cloud droplets, finding that a model bias towards very wide and bimodal distribution of turbulent updraft strength is tightly connected to a similarly wide cloud droplet number distribution.

A key factor in this work was the availability of instrumental data from multiple platforms separated by over 2000 km in the region, as well as redundant sensors across and within campaigns. Not only did these broad observations improve the representativeness of the field campaign data in total, but they also provided a window into processes that are difficult to observe on the spatial or temporal scales of a single aircraft campaign and which have large impacts on climate, such as long-term photochemical smoke aging. My evaluation also motivated a deeper look into the model and observational data that uncovered two important bugs. The first was a long-standing but unknown bug in WRF-Chem's calculation of CCN based on particle diameter. Due to my findings, the development team has since fixed the issue in the main WRF-Chem development branch. Second, by comparing instrumental data from ORACLES, CLARIFY, and LASIC, I found a strong underestimation in archived CLARIFY CCN data—now corrected in the data archive—that would have been invisible if not for my detailed examination of BL data.

In Chapter 3, I further evaluated smoke representation in the SEA from two global models, E3SM and CESM. This was a deep-dive into some of the process biases suggested in the WRF-CAM5 work to study their sensitivities in models used explicitly for global climate research. I implemented schemes into E3SM to represent photolytic volatilization and evaporation of organics—as a proxy for oxidative chemistry and evaporation broadly—and found it explained most observed OA losses over timescales of ~2 weeks. I also evaluated the response of BL aerosol sulfate to oceanic DMS emissions and the photolytic losses of OA, findings that both play a large part in accurately representing the large chemical shift between FT and BL aerosol populations in the smoky SEA. Connecting chemical and size properties of aerosols with the indication of turbulence dominating cloud droplet activation biases from chapter 2, I increased the turbulent updraft speeds in cloud activation for both models. This resulted in a large reduction in the bias of cloud nucleation efficiency in both models against observations. This demonstrated that, in this highly polluted region and time, accurately representing turbulence is critical to accurate representation of cloud droplet number. I also showed that removing DMS to curtail BL sulfate aerosol formation in E3SM, though not CESM, can reduce the number concentration enough to increase diameter and therefore cloud droplet nucleation, with an impact similar to increased turbulence.

This work provides multiple useful targets for improvement in future climate modeling projects. Aerosol size and composition strongly impact its radiative properties, and cloud droplet number is a major determinant of cloud albedo, precipitation, and thermodynamic evolution. A useful application of this work would be an assessment of the impacts of turbulence and biomass-burning smoke aging on long-term radiative balance in the highly uncertain southeastern Atlantic Ocean, including a disambiguation of changes in single-particle optical properties, composition, and size over time. We also recommend a broader evaluation of boundary layer schemes with high-resolution wind observations to improve the entire spectrum of modeled updrafts in highly polluted regions.

In Chapter 4, I evaluated fire emissions themselves by focusing on wildfires in the western US in September of 2020. Satellite observations of FRP are extremely useful to constructing emissions inventories, but the observations are subject to systemic uncertainties such as clouds obscuring fires or pixel saturation. I utilized NEXRAD weather Doppler as a complementary data source in order to fill in these emissions gaps, as radar-observable smoke properties correlate meaningfully with FRP of large fires. By scaling and reconstructing the RAVE emissions inventory and feeding it into WRF-Chem, I demonstrably improved modeled AOD and surface $PM_{2.5}$ throughout the western US, especially during the peak burning days. This will help to reduce uncertainty both for air quality forecasting and for broader research about biomass-burning smoke emissions, transport, chemistry, and climatic impacts.

The merging of satellite-based fire sensing with Doppler in order to adjust emissions is quite new in the field, and exciting future work remains to be done to analyze and implement this method. First, I plan on continuing analysis of air quality impacts from this emissions scaling with a more detailed and statistical quantification of transport and human exposure levels, especially analyzing ground-level $PM_{2.5}$ against observations. Second, for future research, Doppler smoke modulation can also be applied to other fire seasons and in other regions in order to better constrain this method and evaluate model performance. Third, automation will improve the operational viability of this analysis. For example, existing fire data and bounding algorithms can be deployed across a wide region to locate fires automatically over a given time period. Data from Doppler stations with fixed coverage can be downloaded, and iterations in the machine learning process can improve the FRP extrapolation with less human supervision. Combined, these improvements will expand the spatial coverage, number of fires, and the vital ability to update forecasts and warnings quickly when wildfires are exploding in size. I also see potential in radar-based modifications to improve existing historical emissions inventories and thereby improve model studies of past fires. The benefits of accurate fire emissions are as varied as the field—for one example, studies of overall climate sensitivity to aerosol emissions require a very sharp understanding of current smoke emissions trends, which many models and inventories tend to underestimate.

In summary, this work collectively presents improvements in model representation of biomass-burning smoke across a wide range of applications. On regional and global scales, I have shown that there remain large uncertainties and that observational constraints of size distribution, aging, chemistry, and turbulence are critical to representation of smoke properties and aerosol-cloud interactions. On interstate scales, Doppler radar is an exciting new source of validation and improvements to existing wildfire forecasts and can improve air quality forecasting as wildfires come to define many air quality regimes. These projects collectively show the tremendous benefits of observational constraints on chemical transport models and how creative fusion of observations can improve scientific understanding of complex fire and smoke behavior, while paving the way for deeper implementation of the improvements discovered here and advancing the field.

Appendix

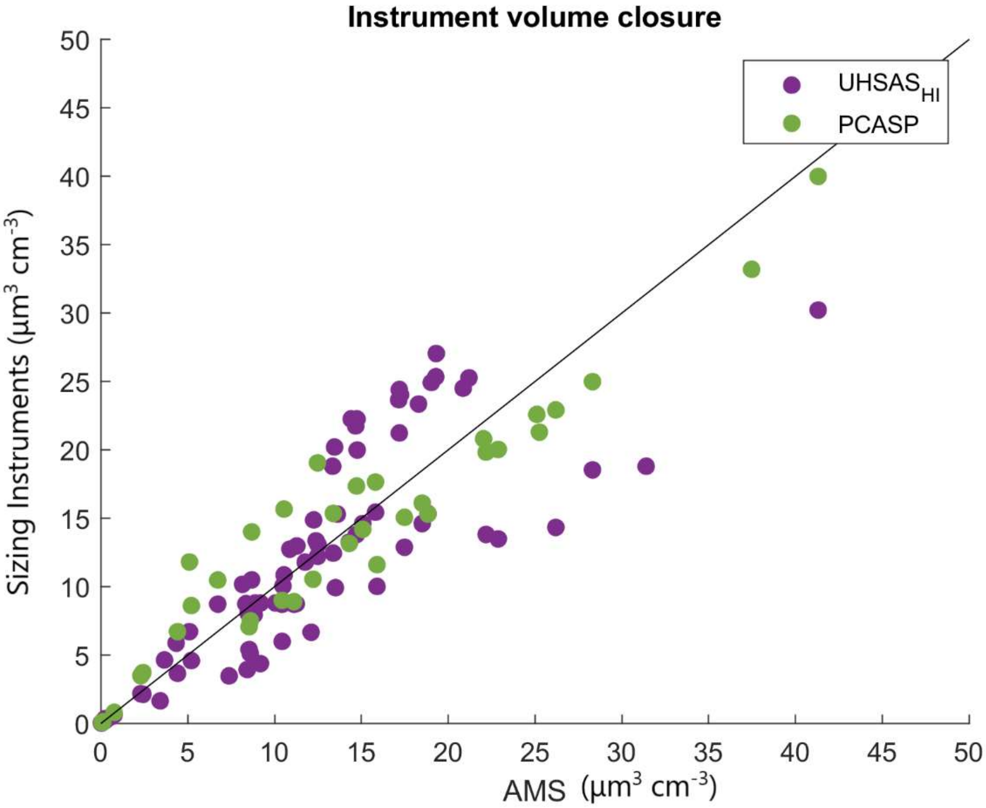

Figure A.1: Total volume concentration in the ORACLES FT, comparing both the U. HI UHSAS and PCASP each against the AMS. Densities assumed for the AMS are listed in Table 2 of main text.

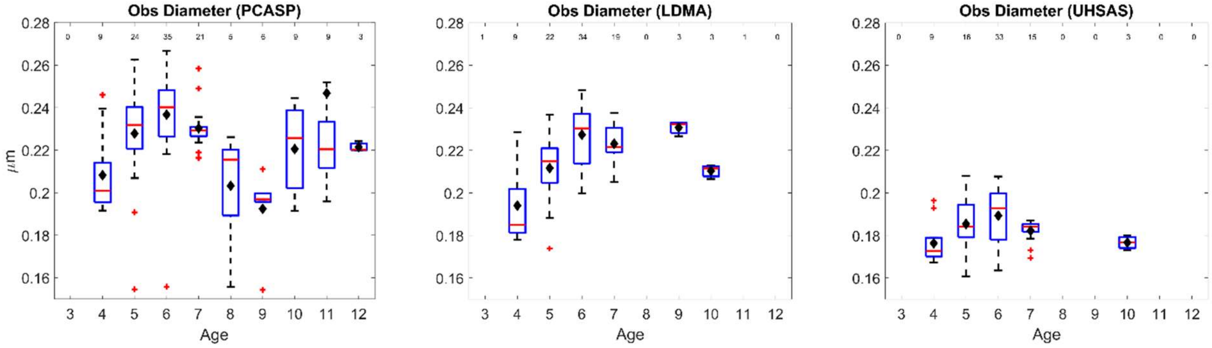

Figure A.2: Geometric mean diameter from observations, binned by WRF-AAM average plume age. PCASP plot uses samples from both ORACLES and CLARIFY, as the only aerosol sizing instrument available in both campaigns. LDMA and UHSAS are both only from ORACLES samples.

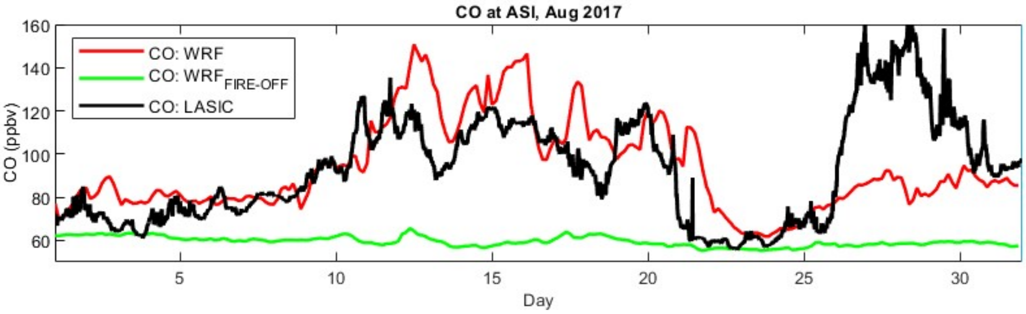

Figure A.3: CO concentrations from WRF-CAM5 both with and without QFED2 fire emissions to illustrate model background, and observations from LASIC for August 2017.

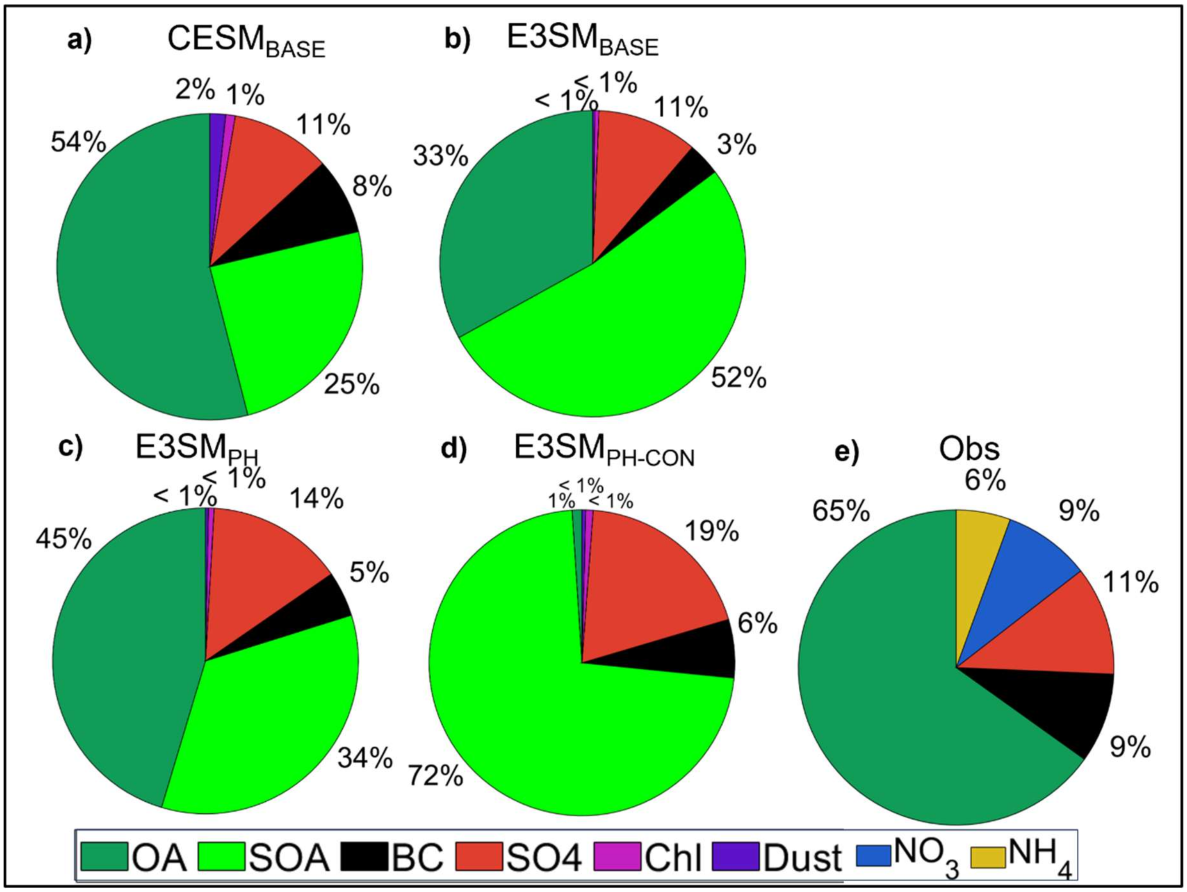

Figure A.4: Free troposphere mean composition breakdown from four model configurations and observations from the AMS and SP2, combining samples co-located with ORACLES and CLARIFY. These models do not represent aerosol nitrate (NO_3) or ammonium (NH_4), and observations do not measure chloride (Chl) or dust. The AMS data used in this work does not disambiguate primary and secondary OA.

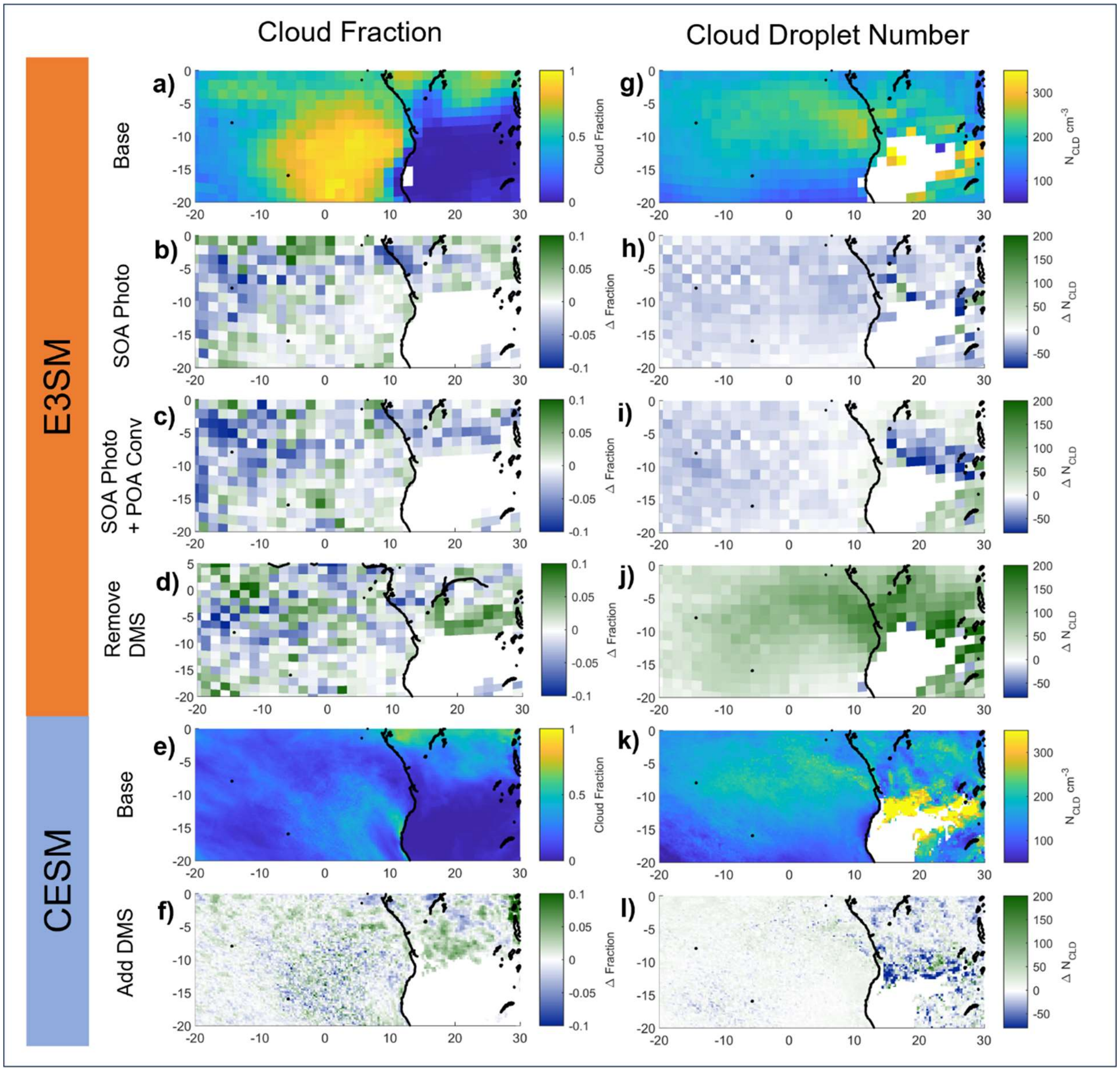

Figure A.5: Cloud properties in E3SM and CESM and their sensitivities to various changes in chemical schemes averaged per column in August 2017. (a-f) cloud fraction is a unitless decimal fraction between 0 and 1, and (g-l) cloud droplet number concentration is in cm^{-3}.

Bibliography

Abatzoglou, J. T., Williams, A. P., and Barbero, R.: Global Emergence of Anthropogenic Climate Change in Fire Weather Indices, Geophys. Res. Lett., 46, 326–336, https://doi.org/10.1029/2018GL080959, 2019.

Abel, S. J., Barrett, P. A., Zuidema, P., Zhang, J., Christensen, M., Peers, F., Taylor, J. W., Crawford, I., Bower, K. N., and Flynn, M.: Open cells exhibit weaker entrainment of free-tropospheric biomass burning aerosol into the south-east Atlantic boundary layer, Atmospheric Chem. Phys., 20, 4059–4084, https://doi.org/10.5194/ACP-20-4059-2020, 2020.

Adebiyi, A. A. and Zuidema, P.: The role of the southern African easterly jet in modifying the southeast Atlantic aerosol and cloud environments, Q. J. R. Meteorol. Soc., 142, 1574–1589, https://doi.org/10.1002/qj.2765, 2016.

Adebiyi, A. A. and Zuidema, P.: Low cloud cover sensitivity to biomass-burning aerosols and meteorology over the Southeast Atlantic, J. Clim., 31, 4329–4346, https://doi.org/10.1175/JCLI-D-17-0406.1, 2018.

Andela, N. and Van Der Werf, G. R.: Recent trends in African fires driven by cropland expansion and El Niño to La Niña transition, Nat. Clim. Change 2014 49, 4, 791–795, https://doi.org/10.1038/nclimate2313, 2014.

Andreae, M. O.: Emission of trace gases and aerosols from biomass burning – an updated assessment, Atmospheric Chem. Phys., 19, 8523–8546, https://doi.org/10.5194/acp-19-8523-2019, 2019.

Avey, L., Garrett, T. J., and Stohl, A.: Evaluation of the aerosol indirect effect using satellite, tracer transport model, and aircraft data from the International Consortium for Atmospheric Research on Transport and Transformation, J. Geophys. Res. Atmospheres, 112, https://doi.org/10.1029/2006JD007581, 2007.

Barrett, P. A., Abel, S. J., Coe, H., Crawford, I., Dobracki, A., Haywood, J., Howell, S., Jones, A., Langridge, J., Mcfarquhar, G. M., Nott, G. J., Price, H., Redemann, J., Shinozuka, Y., Szpek, K., Taylor, J. W., Wood, R., Wu, H., Zuidema, P., Bauguitte, S., Bennett, R., Bower, K., Chen, H., Cochrane, S., Cotterell, M., Davies, N., Delene, D., Flynn, C., Freedman, A., Freitag, S., Gupta, S., Noone, D., Onasch, T. B., Podolske, J., Poellot, M. R., Schmidt, S., Springston, S., Iii, A. J. S., Trembath, J., Vance, A., Zawadowicz, M. A., and Zhang, J.: Intercomparison of airborne and surface-based measurements during the CLARIFY, ORACLES and LASIC field experiments, Atmos Meas Tech, 15, 6329–6371, https://doi.org/10.5194/amt-15-6329-2022, 2022.

Bellouin, N., Quaas, J., Gryspeerdt, E., Kinne, S., and Stier, P.: Bounding Global Aerosol Radiative Forcing of Climate Change, Rev. Geophys., 1–45, https://doi.org/10.1029/2019RG000660, 2019.

Bellouin, N., Quaas, J., Gryspeerdt, E., Kinne, S., Stier, P., Watson-Parris, D., Boucher, O., Carslaw, K. S., Christensen, M., Daniau, A. L., Dufresne, J. L., Feingold, G., Fiedler, S., Forster, P., Gettelman, A., Haywood, J. M., Lohmann, U., Malavelle, F., Mauritsen, T., McCoy, D. T., Myhre, G., Mülmenstädt, J., Neubauer, D., Possner, A., Rugenstein, M., Sato, Y., Schulz, M., Schwartz, S. E., Sourdeval, O., Storelvmo, T., Toll, V., Winker, D., and Stevens, B.: Bounding Global Aerosol Radiative Forcing of Climate Change, Rev. Geophys., 58, e2019RG000660, https://doi.org/10.1029/2019RG000660, 2020.

Bianco, A., Passananti, M., Brigante, M., and Mailhot, G.: Photochemistry of the Cloud Aqueous Phase: A Review, Mol. 2020 Vol 25 Page 423, 25, 423, https://doi.org/10.3390/MOLECULES25020423, 2020.

Bilgiç, E., Tuna Tuygun, G., and Gündüz, O.: Development of an emission estimation method with satellite observations for significant forest fires and comparison with global fire emission inventories: Application to catastrophic fires of summer 2021 over the Eastern Mediterranean, Atmos. Environ., 308, 119871, https://doi.org/10.1016/j.atmosenv.2023.119871, 2023.

Bogenschutz, P. A., Gettelman, A., Morrisson., H., Larson, V. E., Schanen, D. P., Meyer, N. R., and Craig, C.: A PDF-Based Model for Boundary Layer Clouds. Part I: Method and Model Description in: Journal of the Atmospheric Sciences Volume 59 Issue 24 (2002), Geosci. Model Dev., 5, 1407–1423, https://doi.org/doi:10.5194/gmd-5-1407-2012, 2012.

Bond, T. C. and Bergstrom, R. W.: Light Absorption by Carbonaceous Particles: An Investigative Review, http://dx.doi.org/10.1080/02786820500421521, 40, 27–67, https://doi.org/10.1080/02786820500421521, 2007.

Bond, T. C., Doherty, S. J., Fahey, D. W., Forster, P. M., Berntsen, T., Deangelo, B. J., Flanner, M. G., Ghan, S., Kärcher, B., Koch, D., Kinne, S., Kondo, Y., Quinn, P. K., Sarofim, M. C., Schultz, M. G., Schulz, M., Venkataraman, C., Zhang, H., Zhang, S., Bellouin, N., Guttikunda, S. K., Hopke, P. K., Jacobson, M. Z., Kaiser, J. W., Klimont, Z., Lohmann, U., Schwarz, J. P., Shindell, D., Storelvmo, T., Warren, S. G., and Zender, C. S.: Bounding the role of black carbon in the climate system: A scientific assessment, J. Geophys. Res. Atmospheres, 118, 5380–5552, https://doi.org/10.1002/jgrd.50171, 2013.

Borchers-Arriagada, N., Schulz-Antipa, P., and Conte-Grand, M.: Future fire-smoke PM2.5 health burden under climate change in Paraguay, Sci. Total Environ., 924, 171356, https://doi.org/10.1016/j.scitotenv.2024.171356, 2024.

Boucher, O., Randall, D., Artaxo, P., Bretherton, C., Feingold, G., Forster, P., Kerminen, V.-M., Kondo, Y., Liao, H., Lohmann, U., Rasch, P., Satheesh, S. K., Sherwood, S., Stevens, B., and Zhang, X. Y.: Clouds and aerosols, Clim. Change 2013 Phys. Sci. Basis Work. Group Contrib. Fifth Assess. Rep. Intergov. Panel Clim. Change, 9781107057, 571–658, https://doi.org/10.1017/CBO9781107415324.016, 2013.

Bretherton, C. S. and Park, S.: A new moist turbulence parameterization in the community atmosphere model, J. Clim., 22, 3422–3448, https://doi.org/10.1175/2008JCLI2556.1, 2009.

Brown, P. T., Hanley, H., Mahesh, A., Reed, C., Strenfel, S. J., Davis, S. J., Kochanski, A. K., and Clements, C. B.: Climate warming increases extreme daily wildfire growth risk in California, Nature, 621, 760–766, https://doi.org/10.1038/s41586-023-06444-3, 2023.

Buechi, H., Weber, P., Heard, S., Cameron, D., and Plantinga, A. J.: Long-term trends in wildfire damages in California, Int. J. Wildland Fire, 30, 757–762, https://doi.org/10.1071/WF21024, 2021.

Burke, M., Driscoll, A., Heft-Neal, S., Xue, J., Burney, J., and Wara, M.: The changing risk and burden of wildfire in the United States, Proc. Natl. Acad. Sci., 118, e2011048118, https://doi.org/10.1073/pnas.2011048118, 2021.

Chand, D., Wood, R., Anderson, T. L., Satheesh, S. K., and Charlson, R. J.: Satellite-derived direct radiative effect of aerosols dependent on cloud cover, Nat. Geosci. 2009 23, 2, 181–184, https://doi.org/10.1038/ngeo437, 2009.

Chang, R. Y.-W., Slowik, J. G., Shantz, N. C., Vlasenko, A., Liggio, J., Sjostedt, S. J., Leaitch, W. R., and Abbatt, J. P. D.: The hygroscopicity parameter (κ) of ambient organic aerosol at a field site subject to biogenic and anthropogenic influences: relationship to degree of aerosol oxidation, Atmospheric Chem. Phys., 10, 5047–5064, https://doi.org/10.5194/acp-10-5047-2010, 2010.

Che, H., Stier, P., Gordon, H., Watson-Parris, D., and Deaconu, L.: Cloud adjustments dominate the overall negative aerosol radiative effects of biomass burning aerosols in UKESM1 climate model simulations over the south-eastern Atlantic, Atmospheric Chem. Phys., 21, 17–33, https://doi.org/10.5194/ACP-21-17-2021, 2021.

Che, H., Segal-Rozenhaimer, M., Zhang, L., Dang, C., Zuidema, P., Dobracki, A., Sedlacek, A. J., Coe, H., Wu, H., Taylor, J., Zhang, X., Redemann, J., and Haywood, J.: Cloud processing and weeklong ageing affect biomass burning aerosol properties over the south-eastern Atlantic, Commun. Earth Environ. 2022 31, 3, 1–9, https://doi.org/10.1038/s43247-022-00517-3, 2022.

Chen, D., Dai, A., and Hall, A.: The Convective-To-Total Precipitation Ratio and the “Drizzling” Bias in Climate Models, J. Geophys. Res. Atmospheres, 126, e2020JD034198, https://doi.org/10.1029/2020JD034198, 2021.

Chen, Y. and Penner, J. E.: Uncertainty analysis for estimates of the first indirect aerosol effect, Atmospheric Chem. Phys., 5, 2935–2948, https://doi.org/10.5194/acp-5-2935-2005, 2005.

Chen, Y., Zhang, Y., Fan, J., Leung, L. R., and Zhang, Q.: Application of an Online-Coupled Regional Climate Model, WRF-CAM5, over East Asia for Examination of Ice Nucleation Schemes: Part I. Comprehensive Model Evaluation and Trend Analysis for 2006 and 2011, 627–667 pp., https://doi.org/10.3390/cli3030627, 2015.

Chiu, J. C., Yang, C. K., van Leeuwen, P. J., Feingold, G., Wood, R., Blanchard, Y., Mei, F., and Wang, J.: Observational Constraints on Warm Cloud Microphysical Processes Using Machine

Learning and Optimization Techniques, Geophys. Res. Lett., 48, https://doi.org/10.1029/2020GL091236, 2021.

Clarke, A. D., Varner, J. L., Eisele, F., Mauldin, R. L., Tanner, D., and Litchy, M.: Particle production in the remote marine atmosphere: Cloud outflow and subsidence during ACE 1, J. Geophys. Res. Atmospheres, 103, 16397–16409, https://doi.org/10.1029/97JD02987, 1998.

Cochrane, S. P., Schmidt, K. S., Chen, H., Pilewskie, P., Kittelman, S., Redemann, J., Leblanc, S., Pistone, K., Kacenelenbogen, M., Rozenhaimer, M. S., and Shinozuka, Y.: Above-cloud aerosol radiative effects based on ORACLES 2016 and ORACLES 2017 aircraft experiments, Atmos Meas Tech, 12, 6505–6528, 2019.

Dahlkötter, F., Gysel, M., Sauer, D., Minikin, A., Baumann, R., Seifert, P., Ansmann, A., Fromm, M., Voigt, C., and Weinzierl, B.: The Pagami Creek smoke plume after long-range transport to the upper troposphere over Europe-aerosol properties and black carbon mixing state, Atmos Chem Phys, 14, 6111–6137, https://doi.org/10.5194/acp-14-6111-2014, 2014.

Dang, C., Segal-Rozenhaimer, M., Che, H., Zhang, L., Formenti, P., Taylor, J., Dobracki, A., Purdue, S., Wong, P. S., Nenes, A., Sedlacek, A., Coe, H., Redemann, J., Zuidema, P., Howell, S., and Haywood, J.: Biomass burning and marine aerosol processing over the southeast Atlantic Ocean: a TEM single-particle analysis, Atmospheric Chem. Phys., 22, 9389–9412, https://doi.org/10.5194/ACP-22-9389-2022, 2022.

Darmenov, A. S., da Silva, A. M., and Koster, R. D.: The Quick Fire Emissions Dataset (QFED): Documentation of Versions 2.1, 2.2 and 2.4 - NASA Technical Reports Server (NTRS), NASA Tech. Memo., 2015.

Das, S., Colarco, P. R., Oman, L. D., Taha, G., and Torres, O.: The long-term transport and radiative impacts of the 2017 British Columbia pyrocumulonimbus smoke aerosols in the stratosphere, Atmospheric Chem. Phys., 21, 12069–12090, https://doi.org/10.5194/acp-21-12069-2021, 2021.

Dedrick, J. L., Saliba, G., Williams, A. S., Russell, L. M., and Lubin, D.: Retrieval of the sea spray aerosol mode from submicron particle size distributions and supermicron scattering during LASIC, Atmospheric Meas. Tech., 15, 4171–4194, https://doi.org/10.5194/AMT-15-4171-2022, 2022.

Denjean, C., Brito, J., Libois, Q., Mallet, M., Bourrianne, T., Burnet, F., Dupuy, R., Flamant, C., and Knippertz, P.: Unexpected Biomass Burning Aerosol Absorption Enhancement Explained by Black Carbon Mixing State, Geophys. Res. Lett., 47, e2020GL089055, https://doi.org/10.1029/2020GL089055, 2020.

Diamond, M. S., Dobracki, A., Freitag, S., Small Griswold, J. D., Heikkila, A., Howell, S. G., Kacarab, M. E., Podolske, J. R., Saide, P. E., and Wood, R.: Time-dependent entrainment of smoke presents an observational challenge for assessing aerosol–cloud interactions over the southeast Atlantic Ocean, Atmospheric Chem. Phys., 18, 14623–14636, https://doi.org/10.5194/acp-18-14623-2018, 2018.

Diamond, M. S., Saide, P. E., Zuidema, P., Ackerman, A. S., Doherty, S. J., Fridlind, A. M., Gordon, H., Howes, C., Kazil, J., Yamaguchi, T., Zhang, J., Feingold, G., and Wood, R.: Cloud adjustments from large-scale smoke–circulation interactions strongly modulate the southeastern Atlantic stratocumulus-to-cumulus transition, Atmospheric Chem. Phys., 22, 12113–12151, https://doi.org/10.5194/ACP-22-12113-2022, 2022.

Dinar, E., Mentel, T. F., and Rudich, Y.: The density of humic acids and humic like substances (HULIS) from fresh and aged wood burning and pollution aerosol particles, Atmos Chem Phys, 6, 5213–5224, 2006.

Ditas, F., Shaw, R. A., Siebert, H., Simmel, M., Wehner, B., and Wiedensohler, A.: Atmospheric Chemistry and Physics Aerosols-cloud microphysics-thermodynamics-turbulence: evaluating supersaturation in a marine stratocumulus cloud, Atmos Chem Phys, 12, 2459–2468, https://doi.org/10.5194/acp-12-2459-2012, 2012.

Dobracki, A., Zuidema, P., Howell, S. G., Saide, P., Freitag, S., Aiken, A. C., Burton, S. P., Iii, A. J. S., Redemann, J., and Wood, R.: An attribution of the low single-scattering albedo of biomass burning aerosol over the southeastern Atlantic, Atmos Chem Phys, 23, 4775–4799, https://doi.org/10.5194/acp-23-4775-2023, 2023.

Doherty, S. J., Saide, P. E., Zuidema, P., Shinozuka, Y., Ferrada, G. A., Gordon, H., Mallet, M., Meyer, K., Painemal, D., Howell, S. G., Freitag, S., Dobracki, A., Podolske, J. R., Burton, S. P., Ferrare, R. A., Howes, C., Nabat, P., Carmichael, G. R., Da Silva, A., Pistone, K., Chang, I., Gao, L., Wood, R., and Redemann, J.: Modeled and observed properties related to the direct aerosol radiative effect of biomass burning aerosol over the southeastern Atlantic, Atmos Chem Phys, 22, 1–46, https://doi.org/10.5194/acp-22-1-2022, 2022a.

Doherty, S. J., Saide, P. E., Zuidema, P., Shinozuka, Y., Ferrada, G. A., Gordon, H., Mallet, M., Meyer, K., Painemal, D., Howell, S. G., Freitag, S., Dobracki, A., Podolske, J. R., Burton, S. P., Ferrare, R. A., Howes, C., Nabat, P., Carmichael, G. R., Da Silva, A., Pistone, K., Chang, I., Gao, L., Wood, R., and Redemann, J.: Modeled and observed properties related to the direct aerosol radiative effect of biomass burning aerosol over the southeastern Atlantic, Atmos Chem Phys, 22, 1–46, https://doi.org/10.5194/acp-22-1-2022, 2022b.

Duplissy, J., Decarlo, P. F., Dommen, J., Alfarra, M. R., Metzger, A., Barmpadimos, I., Prevot, A. S. H., Weingartner, E., Tritscher, T., Gysel, M., Aiken, A. C., Jimenez, J. L., Canagaratna, M. R., Worsnop, D. R., Collins, D. R., Tomlinson, J., and Baltensperger, U.: Atmospheric Chemistry and Physics Relating hygroscopicity and composition of organic aerosol particulate matter, Atmos Chem Phys, 11, 1155–1165, https://doi.org/10.5194/acp-11-1155-2011, 2011.

Earl, N., Simmonds, I., and Tapper, N.: Weekly cycles of global fires—Associations with religion, wealth and culture, and insights into anthropogenic influences on global climate, Geophys. Res. Lett., 42, 9579–9589, https://doi.org/10.1002/2015GL066383, 2015.

Eck, T. F., Holben, B. N., Reid, J. S., Mukelabai, M. M., Piketh, S. J., Torres, O., Jethva, H. T., Hyer, E. J., Ward, D. E., Dubovik, O., Sinyuk, A., Schafer, J. S., Giles, D. M., Sorokin, M., Smirnov, A., and Slutsker, I.: A seasonal trend of single scattering albedo in southern African biomass-burning particles: Implications for satellite products and estimates of emissions for the world's largest biomass-burning source, J. Geophys. Res. Atmospheres, 118, 6414–6432, https://doi.org/10.1002/JGRD.50500, 2013.

Eidhammer, T., Gettelman, A., Thayer-Calder, K., Watson-Parris, D., Elsaesser, G., Morrison, H., Van Lier-Walqui, M., Song, C., and McCoy, D.: An Extensible Perturbed Parameter Ensemble (PPE) for the Community Atmosphere Model Version 6, https://doi.org/10.5194/egusphere-2023-2165, 15 January 2024.

Facility for Airborne Atmospheric Measurements, Natural Environment Research Council, and Met Office: CLARIFY: in-situ airborne observations by the FAAM BAE-146 aircraft, 2017.

Faulstich, S. D., Schissler, A. G., Strickland, M. J., and Holmes, H. A.: Statistical Comparison and Assessment of Four Fire Emissions Inventories for 2013 and a Large Wildfire in the Western United States, Fire, 5, 27, https://doi.org/10.3390/fire5010027, 2022.

Fiedler, V., Arnold, F., Ludmann, S., Minikin, A., Hamburger, T., Pirjola, L., Dörnbrack, A., and Schlager, H.: African biomass burning plumes over the Atlantic: Aircraft based measurements and implications for H2SO4 and HNO 3 mediated smoke particle activation, Atmospheric Chem. Phys., 11, 3211–3225, https://doi.org/10.5194/ACP-11-3211-2011, 2011.

Fountoukis, C. and Nenes, A.: Continued development of a cloud droplet formation parameterization for global climate models, J. Geophys. Res. Atmospheres, 110, 1–10, https://doi.org/10.1029/2004JD005591, 2005.

Freeborn, P. H., Wooster, M. J., Hao, W. M., Ryan, C. A., Nordgren, B. L., Baker, S. P., and Ichoku, C.: Relationships between energy release, fuel mass loss, and trace gas and aerosol emissions during laboratory biomass fires, J. Geophys. Res. Atmospheres, 113, https://doi.org/10.1029/2007JD008679, 2008.

Freeborn, P. H., Wooster, M. J., Roy, D. P., and Cochrane, M. A.: Quantification of MODIS fire radiative power (FRP) measurement uncertainty for use in satellite-based active fire characterization and biomass burning estimation, Geophys. Res. Lett., 41, 1988–1994, https://doi.org/10.1002/2013GL059086, 2014.

Freeborn, P. H., Jolly, W. M., Cochrane, M. A., and Roberts, G.: Large wildfire driven increases in nighttime fire activity observed across CONUS from 2003–2020, Remote Sens. Environ., 268, 112777, https://doi.org/10.1016/j.rse.2021.112777, 2022.

Freitas, S. R., Longo, K. M., Silva Dias, M. A. F., Silva Dias, P. L., Chatfield, R., Prins, E., Artaxo, P., Grell, G. A., and Recuero, F. S.: Monitoring the Transport of Biomass Burning Emissions in South America, Environ. Fluid Mech., 5, 135–167, 2005.

Freitas, S. R., Longo, K. M., Chatfield, R., Latham, D., Silva Dias, M. a. F., Andreae, M. O., Prins, E., Santos, J. C., Gielow, R., and Carvalho, J. A. J.: Including the sub-grid scale plume rise of vegetation fires in low resolution atmospheric transport models, Atmospheric Chem. Phys., 7, 3385–3398, https://doi.org/10.5194/acp-7-3385-2007, 2007.

French, N. H. F. and Hudak, A. T.: Biomass Burning Fuel Consumption and Emissions for Air Quality, in: Landscape Fire, Smoke, and Health, American Geophysical Union (AGU), 69–88, https://doi.org/10.1002/9781119757030.ch5, 2023.

Garrett, T. J., Zhao, C., and Novelli, P. C.: Assessing the relative contributions of transport efficiency and scavenging to seasonal variability in Arctic aerosol, Tellus Ser. B Chem. Phys. Meteorol., 62, 190–196, https://doi.org/10.1111/J.1600-0889.2010.00453.X, 2010.

Garstang, M., Tyson, P. D., Swap, R., Edwards, M., Kållberg, P., and Lindesay, J. A.: Horizontal and vertical transport of air over southern Africa, J. Geophys. Res. Atmospheres, 101, 23721–23736, https://doi.org/10.1029/95JD00844, 1996.

Gelaro, R., McCarty, W., Suárez, M. J., Todling, R., Molod, A., Takacs, L., Randles, C. A., Darmenov, A., Bosilovich, M. G., Reichle, R., Wargan, K., Coy, L., Cullather, R., Draper, C., Akella, S., Buchard, V., Conaty, A., Silva, A. M. da, Gu, W., Kim, G.-K., Koster, R., Lucchesi, R., Merkova, D., Nielsen, J. E., Partyka, G., Pawson, S., Putman, W., Rienecker, M., Schubert, S. D., Sienkiewicz, M., and Zhao, B.: The Modern-Era Retrospective Analysis for Research and Applications, Version 2 (MERRA-2), J. Clim., 30, 5419–5454, https://doi.org/10.1175/JCLI-D-16-0758.1, 2017.

Giglio, L., Csiszar, I., and Justice, C. O.: Global distribution and seasonality of active fires as observed with the Terra and Aqua Moderate Resolution Imaging Spectroradiometer (MODIS) sensors, J. Geophys. Res. Biogeosciences, 111, https://doi.org/10.1029/2005JG000142, 2006.

Giglio, L., Randerson, J. T., van der Werf, G. R., Kasibhatla, P. S., Collatz, G. J., Morton, D. C., and DeFries, R. S.: Assessing variability and long-term trends in burned area by merging multiple satellite fire products, Biogeosciences, 7, 1171–1186, https://doi.org/10.5194/bg-7-1171-2010, 2010.

Giglio, L., Randerson, J. T., and van der Werf, G. R.: Analysis of daily, monthly, and annual burned area using the fourth-generation global fire emissions database (GFED4), J. Geophys. Res. Biogeosciences, 118, 317–328, https://doi.org/10.1002/jgrg.20042, 2013.

Gilardoni, S., Massoli, P., Paglione, M., Giulianelli, L., Carbone, C., Rinaldi, M., Decesari, S., Sandrini, S., Costabile, F., Gobbi, G. P., Pietrogrande, M. C., Visentin, M., Scotto, F., Fuzzi, S., and Facchini, M. C.: Direct observation of aqueous secondary organic aerosol from biomass-burning emissions, Proc. Natl. Acad. Sci., 113, 10013–10018, https://doi.org/10.1073/pnas.1602212113, 2016.

GOES-R Series Program: NOAA GOES-R Series Advanced Baseline Imager (ABI) Level 0 Data, https://doi.org/doi:10.25921/tvws-w071, 2019.

Golaz, J.-C., Larson, V. E., and Cotton, W. R.: A PDF-Based Model for Boundary Layer Clouds. Part I: Method and Model Description, J. Atmospheric Sci., 59, 3540–3551, https://doi.org/10.1175/1520-0469(2002)059<3540:APBMFB>2.0.CO;2, 2002.

Golaz, J.-C., Van Roekel, L. P., Zheng, X., Roberts, A. F., Wolfe, J. D., Lin, W., Bradley, A. M., Tang, Q., Maltrud, M. E., Forsyth, R. M., Zhang, C., Zhou, T., Zhang, K., Zender, C. S., Wu, M., Wang, H., Turner, A. K., Singh, B., Richter, J. H., Qin, Y., Petersen, M. R., Mametjanov, A., Ma, P.-L., Larson, V. E., Krishna, J., Keen, N. D., Jeffery, N., Hunke, E. C., Hannah, W. M., Guba, O., Griffin, B. M., Feng, Y., Engwirda, D., Di Vittorio, A. V., Dang, C., Conlon, L. M., Chen, C.-C.-J., Brunke, M. A., Bisht, G., Benedict, J. J., Asay-Davis, X. S., Zhang, Y., Zhang, M., Zeng, X., Xie, S., Wolfram, P. J., Vo, T., Veneziani, M., Tesfa, T. K., Sreepathi, S., Salinger, A. G., Reeves Eyre, J. E. J., Prather, M. J., Mahajan, S., Li, Q., Jones, P. W., Jacob, R. L., Huebler, G. W., Huang, X., Hillman, B. R., Harrop, B. E., Foucar, J. G., Fang, Y., Comeau, D. S., Caldwell, P. M., Bartoletti, T., Balaguru, K., Taylor, M. A., McCoy, R. B., Leung, L. R., and Bader, D. C.: The DOE E3SM Model Version 2: Overview of the Physical Model and Initial Model Evaluation, J. Adv. Model. Earth Syst., 14, e2022MS003156, https://doi.org/10.1029/2022MS003156, 2022.

Gordon, H., Field, P. R., Abe, S. J., Dalvi, M., Grosvenor, D. P., Hill, A. A., Johnson, B. T., Miltenberger, A. K., Yoshioka, M., and Carslaw, K. S.: Large simulated radiative effects of smoke in the south-east Atlantic, Atmospheric Chem. Phys., 18, 15261–15289, https://doi.org/10.5194/acp-18-15261-2018, 2018.

Gryspeerdt, E., Povey, A. C., Grainger, R. G., Hasekamp, O., Hsu, N. C., Mulcahy, J. P., Sayer, A. M., and Sorooshian, A.: Uncertainty in aerosol–cloud radiative forcing is driven by clean conditions, Atmospheric Chem. Phys., 23, 4115–4122, https://doi.org/10.5194/ACP-23-4115-2023, 2023.

Guenther, A., Jiang, X., Shah, T., Huang, L., Kemball-Cook, S., and Yarwood, G.: Model of Emissions of Gases and Aerosol from Nature Version 3 (MEGAN3) for Estimating Biogenic Emissions, in: Air Pollution Modeling and its Application XXVI, Cham, 187–192, https://doi.org/10.1007/978-3-030-22055-6_29, 2020.

Gupta, S., McFarquhar, G. M., O'Brien, J. R., Delene, D. J., Poellot, M. R., Dobracki, A., Podolske, J. R., Redemann, J., Leblanc, S. E., Segal-Rozenhaimer, M., and Pistone, K.: Impact of the variability in vertical separation between biomass burning aerosols and marine stratocumulus on cloud microphysical properties over the Southeast Atlantic, Atmospheric Chem. Phys., 21, 4615–4635, https://doi.org/10.5194/ACP-21-4615-2021, 2021.

Halofsky, J. E., Peterson, D. L., and Harvey, B. J.: Changing wildfire, changing forests: the effects of climate change on fire regimes and vegetation in the Pacific Northwest, USA, Fire Ecol., 16, 4, https://doi.org/10.1186/s42408-019-0062-8, 2020.

Hasenkopf, C. A., Flasher, J. C., Veerman, O., and DeWitt, H. L.: OpenAQ: A Platform to Aggregate and Freely Share Global Air Quality Data, AGU Fall Meet. Abstr., 2015, A31D-0097, 2015.

Hays, M. D., Fine, P. M., Geron, C. D., Kleeman, M. J., and Gullett, B. K.: Open burning of agricultural biomass: Physical and chemical properties of particle-phase emissions, Atmos. Environ., 39, 6747–6764, https://doi.org/10.1016/j.atmosenv.2005.07.072, 2005.

Haywood, J. M., Abel, S. J., Barrett, P. A., Bellouin, N., Blyth, A., Bower, K. N., Brooks, M., Carslaw, K., Che, H., Coe, H., Cotterell, M. I., Crawford, I., Cui, Z., Davies, N., Dingley, B., Field, P., Formenti, P., Gordon, H., De Graaf, M., Herbert, R., Johnson, B., Jones, A. C., Langridge, J. M., Malavelle, F., Partridge, D. G., Peers, F., Redemann, J., Stier, P., Szpek, K., Taylor, J. W., Watson-Parris, D., Wood, R., Wu, H., and Zuidema, P.: The CLoud-Aerosol-Radiation Interaction and Forcing: Year 2017 (CLARIFY-2017) measurement campaign, Atmospheric Chem. Phys., 21, 1049–1084, https://doi.org/10.5194/ACP-21-1049-2021, 2021.

Heinold, B., Baars, H., Barja, B., Christensen, M., Kubin, A., Ohneiser, K., Schepanski, K., Schutgens, N., Senf, F., Schrödner, R., Villanueva, D., and Tegen, I.: Important role of stratospheric injection height for the distribution and radiative forcing of smoke aerosol from the 2019–2020 Australian wildfires, Atmospheric Chem. Phys., 22, 9969–9985, https://doi.org/10.5194/acp-22-9969-2022, 2022.

Herbert, R. J., Bellouin, N., Highwood, E. J., and Hill, A. A.: Diurnal cycle of the semi-direct effect from a persistent absorbing aerosol layer over marine stratocumulus in large-eddy simulations, Atmospheric Chem. Phys., 20, 1317–1340, https://doi.org/10.5194/acp-20-1317-2020, 2020.

Hodzic, A., Kasibhatla, P. S., Jo, D. S., Cappa, C. D., Jimenez, J. L., Madronich, S., and Park, R. J.: Rethinking the global secondary organic aerosol (SOA) budget: Stronger production, faster removal, shorter lifetime, Atmospheric Chem. Phys., 16, 7917–7941, https://doi.org/10.5194/acp-16-7917-2016, 2016.

Howell, S. G., Freitag, S., Dobracki, A., Smirnow, N., and Sedlacek III, A. J.: Undersizing of aged African biomass burning aerosol by an ultra-high-sensitivity aerosol spectrometer, Atmospheric Meas. Tech., 14, 7381–7404, https://doi.org/10.5194/amt-14-7381-2021, 2021.

Howes, C., Saide, P. E., Coe, H., Dobracki, A., Freitag, S., Haywood, J. M., Howell, S. G., Gupta, S., Uin, J., Kacarab, M., Kuang, C., Leung, L. R., Nenes, A., McFarquhar, G. M., Podolske, J., Redemann, J., Sedlacek, A. J., Thornhill, K. L., Wong, J. P. S., Wood, R., Wu, H., Zhang, Y., Zhang, J., and Zuidema, P.: Biomass-burning smoke's properties and its interactions with marine stratocumulus clouds in WRF-CAM5 and southeastern Atlantic field campaigns, Atmospheric Chem. Phys., 23, 13911–13940, https://doi.org/10.5194/acp-23-13911-2023, 2023.

Inness, A., Ades, M., Agustí-Panareda, A., Barr, J., Benedictow, A., Blechschmidt, A. M., Jose Dominguez, J., Engelen, R., Eskes, H., Flemming, J., Huijnen, V., Jones, L., Kipling, Z., Massart, S., Parrington, M., Peuch, V. H., Razinger, M., Remy, S., Schulz, M., and Suttie, M.: The CAMS reanalysis of atmospheric composition, Atmospheric Chem. Phys., 19, 3515–3556, https://doi.org/10.5194/ACP-19-3515-2019, 2019.

Janssens-Maenhout, G., Dentener, F., van Aardenne, J., Monni, S., Pagliari, V., Orlandini, L., Klimont, Z., Kurokawa, J., Akimoto, H., Ohara, T., Wankmüller, R., Battye, B., Grano, D., Zuber, A., and Keating, T.: EDGAR-HTAP: a harmonized gridded air pollution emission dataset based on national inventories, JRC Sci. Tech. Rep., https://doi.org/10.2788/14102, 2012.

Jerrett, M., Jina, A. S., and Marlier, M. E.: Up in smoke: California's greenhouse gas reductions could be wiped out by 2020 wildfires, Environ. Pollut., 310, 119888, https://doi.org/10.1016/j.envpol.2022.119888, 2022.

Jimenez, J. L., Canagaratna, M. R., Donahue, N. M., Prevot, A. S. H., Zhang, Q., Kroll, J. H., DeCarlo, P. F., Allan, J. D., Coe, H., Ng, N. L., Aiken, A. C., Docherty, K. S., Ulbrich, I. M., Grieshop, A. P., Robinson, A. L., Duplissy, J., Smith, J. D., Wilson, K. R., Lanz, V. A., Hueglin, C., Sun, Y. L., Tian, J., Laaksonen, A., Raatikainen, T., Rautiainen, J., Vaattovaara, P., Ehn, M., Kulmala, M., Tomlinson, J. M., Collins, D. R., Cubison, M. J., Dunlea, E. J., Huffman, J. A., Onasch, T. B., Alfarra, M. R., Williams, P. I., Bower, K., Kondo, Y., Schneider, J., Drewnick, F., Borrmann, S., Weimer, S., Demerjian, K., Salcedo, D., Cottrell, L., Griffin, R., Takami, A., Miyoshi, T., Hatakeyama, S., Shimono, A., Sun, J. Y., Zhang, Y. M., Dzepina, K., Kimmel, J. R., Sueper, D., Jayne, J. T., Herndon, S. C., Trimborn, A. M., Williams, L. R., Wood, E. C., Middlebrook, A. M., Kolb, C. E., Baltensperger, U., and Worsnop, D. R.: Evolution of organic aerosols in the atmosphere, Science, 326, 1525–1529, https://doi.org/10.1126/SCIENCE.1180353/SUPPL_FILE/JIMENEZ.SOM.PDF, 2009.

Johnson, J. S., Regayre, L. A., Yoshioka, M., Pringle, K. J., Lee, L. A., Sexton, D. M. H., Rostron, J. W., Booth, B. B. B., and Carslaw, K. S.: The importance of comprehensive parameter sampling and multiple observations for robust constraint of aerosol radiative forcing, Atmospheric Chem. Phys., 18, 13031–13053, https://doi.org/10.5194/ACP-18-13031-2018, 2018.

Johnston, F. H., Borchers-Arriagada, N., Morgan, G. G., Jalaludin, B., Palmer, A. J., Williamson, G. J., and Bowman, D. M. J. S.: Unprecedented health costs of smoke-related PM2.5 from the 2019–20 Australian megafires, Nat. Sustain., 4, 42–47, https://doi.org/10.1038/s41893-020-00610-5, 2021.

Jones, M. W., Abatzoglou, J. T., Veraverbeke, S., Andela, N., Lasslop, G., Forkel, M., Smith, A. J. P., Burton, C., Betts, R. A., van der Werf, G. R., Sitch, S., Canadell, J. G., Santín, C., Kolden, C., Doerr, S. H., and Le Quéré, C.: Global and Regional Trends and Drivers of Fire Under Climate Change, Rev. Geophys., 60, e2020RG000726, https://doi.org/10.1029/2020RG000726, 2022.

Justice, C. O., Giglio, L., Korontzi, S., Owens, J., Morisette, J. T., Roy, D., Descloitres, J., Alleaume, S., Petitcolin, F., and Kaufman, Y.: The MODIS fire products, Remote Sens. Environ., 83, 244–262, https://doi.org/10.1016/S0034-4257(02)00076-7, 2002.

Kacarab, M., Lee Thornhill, K., Dobracki, A., Howell, S. G., O'Brien, J. R., Freitag, S., Poellot, M. R., Wood, R., Zuidema, P., Redemann, J., and Nenes, A.: Biomass burning aerosol as a modulator of the droplet number in the southeast Atlantic region, Atmospheric Chem. Phys., 20, 3029–3040, https://doi.org/10.5194/acp-20-3029-2020, 2020.

Kaiser, J. W., Heil, A., Andreae, M. O., Benedetti, A., Chubarova, N., Jones, L., Morcrette, J.-J., Razinger, M., Schultz, M. G., Suttie, M., and van der Werf, G. R.: Biomass burning emissions estimated with a global fire assimilation system based on observed fire radiative power, Biogeosciences, 9, 527–554, https://doi.org/10.5194/bg-9-527-2012, 2012.

Kalogridis, A.-C., Popovicheva, O. B., Engling, G., Diapouli, E., Kawamura, K., Tachibana, E., Ono, K., Kozlov, V. S., and Eleftheriadis, K.: Smoke aerosol chemistry and aging of Siberian biomass burning emissions in a large aerosol chamber, Atmos. Environ., 185, 15–28, https://doi.org/10.1016/j.atmosenv.2018.04.033, 2018.

Karlsson, J., Svensson, G., Cardoso, S., Teixeira, J., and Paradise, S.: Subtropical Cloud-Regime Transitions: Boundary Layer Depth and Cloud-Top Height Evolution in Models and Observations, J. Appl. Meteorol. Climatol., 49, 1845–1858, https://doi.org/10.1175/2010JAMC2338.1, 2010.

Karydis, V. A., Capps, S. L., Russell, A. G., and Nenes, A.: Adjoint sensitivity of global cloud droplet number to aerosol and dynamical parameters, Atmospheric Chem. Phys., 12, 9041–9055, https://doi.org/10.5194/acp-12-9041-2012, 2012.

Kaufman, Y. J., Haywood, J. M., Hobbs, P. V., Hart, W., Kleidman, R., and Schmid, B.: Remote sensing of vertical distributions of smoke aerosol off the coast of Africa, Geophys. Res. Lett., 30, 1831, https://doi.org/10.1029/2003GL017068, 2003.

Keeley, J. E. and Syphard, A. D.: Large California wildfires: 2020 fires in historical context, Fire Ecol., 17, 22, https://doi.org/10.1186/s42408-021-00110-7, 2021.

Keshtkar, H. and Ashbaugh, L. L.: Size distribution of polycyclic aromatic hydrocarbon particulate emission factors from agricultural burning, Atmos. Environ., 41, 2729–2739, https://doi.org/10.1016/j.atmosenv.2006.11.043, 2007.

Kok, J. F.: A scaling theory for the size distribution of emitted dust aerosols suggests climate models underestimate the size of the global dust cycle, Proc. Natl. Acad. Sci. U. S. A., 108, 1016–1021, https://doi.org/10.1073/pnas.1014798108, 2011.

Konovalov, I. B., Beekmann, M., Golovushkin, N. A., and Andreae, M. O.: Nonlinear behavior of organic aerosol in biomass burning plumes: A microphysical model analysis, Atmospheric Chem. Phys., 19, 12091–12119, https://doi.org/10.5194/ACP-19-12091-2019, 2019.

Kroll, J. H., Smith, J. D., Che, D. L., Kessler, S. H., Worsnop, D. R., and Wilson, K. R.: Measurement of fragmentation and functionalization pathways in the heterogeneous oxidation of oxidized organic aerosol, Phys. Chem. Chem. Phys., 11, https://doi.org/10.1039/b905289e, 2009.

Kuang, Y., Xu, W., Tao, J., Ma, N., Zhao, C., and Shao, M.: A Review on Laboratory Studies and Field Measurements of Atmospheric Organic Aerosol Hygroscopicity and Its Parameterization Based on Oxidation Levels, Curr. Pollut. Rep. 2020 64, 6, 410–424, https://doi.org/10.1007/S40726-020-00164-2, 2020.

Kuwata, M., Zorn, S. R., and Martin, S. T.: Using Elemental Ratios to Predict the Density of Organic Material Composed of Carbon, Hydrogen, and Oxygen, Environ. Sci. Technol., 46, 787–794, https://doi.org/10.1021/ES202525Q, 2011.

Lamarque, J.-F., Emmons, L. K., Hess, P. G., Kinnison, D. E., Tilmes, S., Vitt, F., Heald, C. L., Holland, E. A., Lauritzen, P. H., Neu, J., Orlando, J. J., Rasch, P., and Tyndall, G.: CAM-chem: description and evaluation of interactive atmospheric chemistry in CESM, https://doi.org/10.5194/gmdd-4-2199-2011, 16 September 2011.

Le Clainche, Y., Vézina, A., Levasseur, M., Cropp, R. A., Gunson, J. R., Vallina, S. M., Vogt, M., Lancelot, C., Allen, J. I., Archer, S. D., Bopp, L., Deal, C., Elliott, S., Jin, M., Malin, G., Schoemann, V., Simó, R., Six, K. D., and Stefels, J.: A first appraisal of prognostic ocean DMS models and prospects for their use in climate models, Glob. Biogeochem. Cycles, 24, https://doi.org/10.1029/2009GB003721, 2010.

Leahy, L. V., Anderson, T. L., Eck, T. F., and Bergtrom, R. W.: A synthesis of single scattering albedo of biomass burning aerosol over southern Africa during SAFARI 2000, Geophys. Res. Lett., 34, 12814, https://doi.org/10.1029/2007GL029697, 2007.

Li, C., Li, J., Dubovik, O., Zeng, Z. C., and Yung, Y. L.: Impact of Aerosol Vertical Distribution on Aerosol Optical Depth Retrieval from Passive Satellite Sensors, Remote Sens. 2020 Vol 12 Page 1524, 12, 1524, https://doi.org/10.3390/RS12091524, 2020.

Li, F., Val Martin, M., Andreae, M. O., Arneth, A., Hantson, S., Kaiser, J. W., Lasslop, G., Yue, C., Bachelet, D., Forrest, M., Kluzek, E., Liu, X., Mangeon, S., Melton, J. R., Ward, D. S., Darmenov, A., Hickler, T., Ichoku, C., Magi, B. I., Sitch, S., van der Werf, G. R., Wiedinmyer, C., and Rabin, S. S.: Historical (1700–2012) global multi-model estimates of the fire emissions from the Fire Modeling Intercomparison Project (FireMIP), Atmospheric Chem. Phys., 19, 12545–12567, https://doi.org/10.5194/acp-19-12545-2019, 2019.

Li, F., Zhang, X., and Kondragunta, S.: Highly anomalous fire emissions from the 2019–2020 Australian bushfires, Environ. Res. Commun., 3, 105005, https://doi.org/10.1088/2515-7620/ac2e6f, 2021a.

Li, F., Zhang, X., Kondragunta, S., Lu, X., Csiszar, I., and Schmidt, C. C.: Hourly biomass burning emissions product from blended geostationary and polar-orbiting satellites for air quality forecasting applications, Remote Sens. Environ., 281, 113237, https://doi.org/10.1016/j.rse.2022.113237, 2022.

Li, X., Wang, S., Duan, L., Hao, J., Li, C., Chen, Y., and Yang, L.: Particulate and trace gas emissions from open burning of wheat straw and corn stover in China, Environ. Sci. Technol., 41, 6052–6058, https://doi.org/10.1021/es0705137, 2007.

Li, Y., Tong, D., Ma, S., Zhang, X., Kondragunta, S., Li, F., and Saylor, R.: Dominance of Wildfires Impact on Air Quality Exceedances During the 2020 Record-Breaking Wildfire Season in the United States, Geophys. Res. Lett., 48, e2021GL094908, https://doi.org/10.1029/2021GL094908, 2021b.

Li, Y., Tong, D., Makkaroon, P., DelSole, T., Tang, Y., Campbell, P., Baker, B., Cohen, M., Darmenov, A., Ahmadov, R., James, E., Hyer, E., and Xian, P.: Multi-Agency Ensemble Forecast of Wildfire Air Quality in the United States: Toward Community Consensus of Early Warning, Bull. Am. Meteorol. Soc., 1, https://doi.org/10.1175/BAMS-D-23-0208.1, 2024.

Liu, S. and Liang, X. Z.: Observed Diurnal Cycle Climatology of Planetary Boundary Layer Height, J. Clim., 23, 5790–5809, https://doi.org/10.1175/2010JCLI3552.1, 2010.

Liu, T., Mickley, L. J., Marlier, M. E., DeFries, R. S., Khan, M. F., Latif, M. T., and Karambelas, A.: Diagnosing spatial biases and uncertainties in global fire emissions inventories: Indonesia as regional case study, Remote Sens. Environ., 237, 111557, https://doi.org/10.1016/j.rse.2019.111557, 2020.

Liu, X., Easter, R. C., Ghan, S. J., Zaveri, R., Rasch, P., Shi, X., Lamarque, J. F., Gettelman, A., Morrison, H., Vitt, F., Conley, A., Park, S., Neale, R., Hannay, C., Ekman, A. M. L., Hess, P., Mahowald, N., Collins, W., Iacono, M. J., Bretherton, C. S., Flanner, M. G., and Mitchell, D.: Toward a minimal representation of aerosols in climate models: Description and evaluation in the Community Atmosphere Model CAM5, Geosci. Model Dev., 5, 709–739, https://doi.org/10.5194/GMD-5-709-2012, 2012.

Liu, X., Ma, P.-L., Wang, H., Tilmes, S., Singh, B., Easter, R. C., Ghan, S. J., and Rasch, P. J.: Description and evaluation of a new four-mode version of the Modal Aerosol Module (MAM4) within version 5.3 of the Community Atmosphere Model, Geosci. Model Dev., 9, 505–522, https://doi.org/10.5194/gmd-9-505-2016, 2016.

Liu, Y., Stanturf, J., and Goodrick, S.: Trends in global wildfire potential in a changing climate, For. Ecol. Manag., 259, 685–697, https://doi.org/10.1016/j.foreco.2009.09.002, 2010.

Lou, S., Shrivastava, M., Easter, R. C., Yang, Y., Ma, P. L., Wang, H., Cubison, M. J., Campuzano-Jost, P., Jimenez, J. L., Zhang, Q., Rasch, P. J., Shilling, J. E., Zelenyuk, A., Dubey, M., Cameron-Smith, P., Martin, S. T., Schneider, J., and Schulz, C.: New SOA Treatments Within the Energy Exascale Earth System Model (E3SM): Strong Production and Sinks Govern Atmospheric SOA Distributions and Radiative Forcing, J. Adv. Model. Earth Syst., 12, e2020MS002266, https://doi.org/10.1029/2020MS002266, 2020.

Lu, Z., Liu, X., Zhang, Z., Zhao, C., Meyer, K., Rajapakshe, C., Wu, C., Yang, Z., and Penner, J. E.: Biomass smoke from southern Africa can significantly enhance the brightness of stratocumulus over the southeastern Atlantic Ocean, Proc. Natl. Acad. Sci., 115, 2924–2929, https://doi.org/10.1073/pnas.1713703115, 2018.

Lu, Z., Liu, X., Zaveri, R. A., Easter, R. C., Tilmes, S., Emmons, L. K., Vitt, F., Singh, B., Wang, H., Zhang, R., and Rasch, P. J.: Radiative Forcing of Nitrate Aerosols From 1975 to 2010 as Simulated by MOSAIC Module in CESM2-MAM4, J. Geophys. Res. Atmospheres, 126, e2021JD034809, https://doi.org/10.1029/2021JD034809, 2021.

Ma, P. L., Rasch, P. J., Fast, J. D., Easter, R. C., Gustafson, W. I., Liu, X., Ghan, S. J., and Singh, B.: Assessing the CAM5 physics suite in the WRF-Chem model: Implementation, resolution sensitivity, and a first evaluation for a regional case study, Geosci. Model Dev., 7, 755–778, https://doi.org/10.5194/GMD-7-755-2014, 2014.

Magi, B. I., Fu, Q., Redemann, J., and Schmid, B.: Using aircraft measurements to estimate the magnitude and uncertainty of the shortwave direct radiative forcing of southern African biomass burning aerosol, J. Geophys. Res. Atmospheres, 113, 5213, https://doi.org/10.1029/2007JD009258, 2008.

Marshall, J. S. and Palmer, W. M. K.: THE DISTRIBUTION OF RAINDROPS WITH SIZE, J. Atmospheric Sci., 5, 165–166, https://doi.org/10.1175/1520-0469(1948)005<0165:TDORWS>2.0.CO;2, 1948.

Matz, C. J., Egyed, M., Xi, G., Racine, J., Pavlovic, R., Rittmaster, R., Henderson, S. B., and Stieb, D. M.: Health impact analysis of PM2.5 from wildfire smoke in Canada (2013–2015, 2017–2018), Sci. Total Environ., 725, 138506, https://doi.org/10.1016/j.scitotenv.2020.138506, 2020.

McCarthy, N., Guyot, A., Dowdy, A., and McGowan, H.: Wildfire and Weather Radar: A Review, J. Geophys. Res. Atmospheres, 124, 266–286, https://doi.org/10.1029/2018JD029285, 2019.

Mesinger, F., DiMego, G., Kalnay, E., Mitchell, K., Shafran, P. C., Ebisuzaki, W., Jović, D., Woollen, J., Rogers, E., Berbery, E. H., Ek, M. B., Fan, Y., Grumbine, R., Higgins, W., Li, H., Lin, Y., Manikin, G., Parrish, D., and Shi, W.: North American Regional Reanalysis, Bull. Am. Meteorol. Soc., 87, 343–360, https://doi.org/10.1175/BAMS-87-3-343, 2006.

Meskhidze, N., Petters, M. D., Tsigaridis, K., Bates, T., O'Dowd, C., Reid, J., Lewis, E. R., Gantt, B., Anguelova, M. D., Bhave, P. V., Bird, J., Callaghan, A. H., Ceburnis, D., Chang, R., Clarke, A., de Leeuw, G., Deane, G., Demott, P. J., Elliot, S., Facchini, M. C., Fairall, C. W., Hawkins, L., Hu, Y., Hudson, J. G., Johnson, M. S., Kaku, K. C., Keene, W. C., Kieber, D. J., Long, M. S., Mårtensson, M., Modini, R. L., Osburn, C. L., Prather, K. A., Pszenny, A., Rinaldi, M., Russell, L. M., Salter, M., Sayer, A. M., Smirnov, A., Suda, S. R., Toth, T. D., Worsnop, D. R., Wozniak, A., and Zorn, S. R.: Production mechanisms, number concentration, size distribution, chemical composition, and optical properties of sea spray aerosols, Atmospheric Sci. Lett., 14, 207–213, https://doi.org/10.1002/ASL2.441, 2013.

Miller, R. M., McFarquhar, G. M., Rauber, R. M., O'Brien, J. R., Gupta, S., Segal-Rozenhaimer, M., Dobracki, A. N., Sedlacek, A. J., Burton, S. P., Howell, S. G., Freitag, S., and Dang, C.: Observations of supermicron-sized aerosols originating from biomass burning in southern Central Africa, Atmospheric Chem. Phys., 21, 14815–14831, https://doi.org/10.5194/ACP-21-14815-2021, 2021.

Morales, R. and Nenes, A.: Characteristic updrafts for computing distribution-averaged cloud droplet number and stratocumulus cloud properties, J. Geophys. Res. Atmospheres, 115, 18220, https://doi.org/10.1029/2009JD013233, 2010.

Morrison, H. and Gettelman, A.: A New Two-Moment Bulk Stratiform Cloud Microphysics Scheme in the Community Atmosphere Model, Version 3 (CAM3). Part I: Description and Numerical Tests, J. Clim., 21, 3642–3659, https://doi.org/10.1175/2008JCLI2105.1, 2008.

Myhre, G., Samset, B. H., Schulz, M., Balkanski, Y., Bauer, S., Berntsen, T. K., Bian, H., Bellouin, N., Chin, M., Diehl, T., Easter, R. C., Feichter, J., Ghan, S. J., Hauglustaine, D., Iversen, T., Kinne, S., Kirkevåg, A., Lamarque, J. F., Lin, G., Liu, X., Lund, M. T., Luo, G., Ma, X., Van Noije, T., Penner, J. E., Rasch, P. J., Ruiz, A., Seland, Skeie, R. B., Stier, P., Takemura, T., Tsigaridis, K., Wang, P., Wang, Z., Xu, L., Yu, H., Yu, F., Yoon, J. H., Zhang, K., Zhang, H., and Zhou, C.: Radiative forcing of the direct aerosol effect from AeroCom Phase II simulations, Atmospheric Chem. Phys., 13, 1853–1877, https://doi.org/10.5194/ACP-13-1853-2013, 2013.

National Centers for Environmental Prediction, National Weather Service, NOAA, U.S. Department of Commerce: NCEP FNL Operational Model Global Tropospheric Analyses, continuing from July 1999, 2000.

Niemand, M., Möhler, O., Vogel, B., Vogel, H., Hoose, C., Connolly, P., Klein, H., Bingemer, H., DeMott, P., Skrotzki, J., Leisner, T., Niemand, M., Möhler, O., Vogel, B., Vogel, H., Hoose, C., Connolly, P., Klein, H., Bingemer, H., DeMott, P., Skrotzki, J., and Leisner, T.: A Particle-Surface-Area-Based Parameterization of Immersion Freezing on Desert Dust Particles, J. Atmospheric Sci., 69, 3077–3092, https://doi.org/10.1175/JAS-D-11-0249.1, 2012.

NOAA National Centers for Environmental Information: NOAA Next Generation Radar (NEXRAD) Level 2 Base Data, https://doi.org/doi:10.7289/V5W9574V, 1991.

Annual 2020 Wildfires Report | National Centers for Environmental Information (NCEI): https://www.ncei.noaa.gov/access/monitoring/monthly-report/fire/202013, last access: 10 May 2024.

O'Brien, R. E. and Kroll, J. H.: Photolytic Aging of Secondary Organic Aerosol: Evidence for a Substantial Photo-Recalcitrant Fraction, J. Phys. Chem. Lett., 10, 4003–4009, https://doi.org/10.1021/ACS.JPCLETT.9B01417, 2019.

O'Dell, K., Bilsback, K., Ford, B., Martenies, S. E., Magzamen, S., Fischer, E. V., and Pierce, J. R.: Estimated Mortality and Morbidity Attributable to Smoke Plumes in the United States: Not Just a Western US Problem, GeoHealth, 5, e2021GH000457, https://doi.org/10.1029/2021GH000457, 2021.

Ogura, T., Shiogama, H., Watanabe, M., Yoshimori, M., Yokohata, T., Annan, J. D., Hargreaves, J. C., Ushigami, N., Hirota, K., Someya, Y., Kamae, Y., Tatebe, H., and Kimoto, M.: Effectiveness and limitations of parameter tuning in reducing biases of top-of-atmosphere radiation and clouds in MIROC version 5, Geosci. Model Dev., 10, 4647–4664, https://doi.org/10.5194/gmd-10-4647-2017, 2017.

Pagonis, D., Selimovic, V., Campuzano-Jost, P., Guo, H., Day, D. A., Schueneman, M. K., Nault, B. A., Coggon, M. M., DiGangi, J. P., Diskin, G. S., Fortner, E. C., Gargulinski, E. M., Gkatzelis, G. I., Hair, J. W., Herndon, S. C., Holmes, C. D., Katich, J. M., Nowak, J. B., Perring, A. E., Saide, P., Shingler, T. J., Soja, A. J., Thapa, L. H., Warneke, C., Wiggins, E. B., Wisthaler, A., Yacovitch, T. I., Yokelson, R. J., and Jimenez, J. L.: Impact of Biomass Burning Organic Aerosol Volatility on Smoke Concentrations Downwind of Fires, Environ. Sci. Technol., 57, 17011–17021, https://doi.org/10.1021/acs.est.3c05017, 2023.

Painemal, D.: Global Estimates of Changes in Shortwave Low-Cloud Albedo and Fluxes Due to Variations in Cloud Droplet Number Concentration Derived From CERES-MODIS Satellite Sensors, Geophys. Res. Lett., 45, 9288–9296, https://doi.org/10.1029/2018GL078880, 2018.

Pennypacker, S., DIamond, M., and Wood, R.: Ultra-clean and smoky marine boundary layers frequently occur in the same season over the southeast Atlantic, Atmospheric Chem. Phys., 20, 2341–2351, https://doi.org/10.5194/ACP-20-2341-2020, 2020.

Pesenson, I.: Implementation and evaluation of the Heffter method to calculate the height of the planetary boundary layer above the ARM Southern Great Plains site, https://doi.org/10.2172/822178, 2003.

Peterson, D. A., Fromm, M. D., McRae, R. H. D., Campbell, J. R., Hyer, E. J., Taha, G., Camacho, C. P., Kablick, G. P., Schmidt, C. C., and DeLand, M. T.: Australia's Black Summer pyrocumulonimbus super outbreak reveals potential for increasingly extreme stratospheric smoke events, Npj Clim. Atmospheric Sci., 4, 1–16, https://doi.org/10.1038/s41612-021-00192-9, 2021.

Petters, M. D. and Kreidenweis, S. M.: Atmospheric Chemistry and Physics A single parameter representation of hygroscopic growth and cloud condensation nucleus activity, Atmos Chem Phys, 7, 1961–1971, 2007.

Petters, M. D. and Kreidenweis, S. M.: A single parameter representation of hygroscopic growth and cloud condensation nucleus activity - Part 2: Including solubility, Atmospheric Chem. Phys., 8, 6273–6279, https://doi.org/10.5194/acp-8-6273-2008, 2008.

Phillips, N.: Marshall fire losses now expected to exceed $2 billion — making it the 10th costliest wildfire in U.S. history, Denver Post, 27th October, 2022.

Ponczek, M., A. Franco, M., Carbone, S., V. Rizzo, L., Santos, D. M. dos, G. Morais, F., Duarte, A., J. Barbosa, H. M., and Artaxo, P.: Linking the chemical composition and optical properties of biomass burning aerosols in Amazonia, Environ. Sci. Atmospheres, 2, 252–269, https://doi.org/10.1039/D1EA00055A, 2022.

Prabhakaran, P., Shawon, A. S. M., Kinney, G., Thomas, S., Cantrell, W., and Shaw, R. A.: The role of turbulent fluctuations in aerosol activation and cloud formation, Proc. Natl. Acad. Sci. U. S. A., 117, 16831–16838, https://doi.org/10.1073/PNAS.2006426117/SUPPL_FILE/PNAS.2006426117.SAPP.PDF, 2020.

Qin, W., Fang, H., Wang, L., Wei, J., Zhang, M., Su, X., Bilal, M., and Liang, X.: MODIS high-resolution MAIAC aerosol product: Global validation and analysis, Atmos. Environ., 264, 118684, https://doi.org/10.1016/j.atmosenv.2021.118684, 2021.

Randerson, J. T., van der Werf, G. R., Giglio, L., Collatz, G. J., and Kasibhatla, P. S.: Global Fire Emissions Database, Version 4.1 (GFEDv4), , https://doi.org/10.3334/ORNLDAAC/1293, 2017.

Redemann, J., Wood, R., Zuidema, P., Doherty, S. J., Luna, B., LeBlanc, S. E., Diamond, M. S., Shinozuka, Y., Chang, I. Y., Ueyama, R., Pfister, L., Ryoo, J. M., Dobracki, A. N., da Silva, A. M., Longo, K. M., Kacenelenbogen, M. S., Flynn, C. J., Pistone, K., Knox, N. M., Piketh, S. J., Haywood, J. M., Formenti, P., Mallet, M., Stier, P., Ackerman, A. S., Bauer, S. E., Fridlind, A. M., Carmichael, G. R., Saide, P. E., Ferrada, G. A., Howell, S. G., Freitag, S., Cairns, B., Holben, B. N., Knobelspiesse, K. D., Tanelli, S., L'Ecuyer, T. S., Dzambo, A. M., Sy, O. O., McFarquhar, G. M., Poellot, M. R., Gupta, S., O'Brien, J. R., Nenes, A., Kacarab, M., Wong, J. P. S., Small-Griswold, J. D., Thornhill, K. L., Noone, D., Podolske, J. R., Sebastian Schmidt, K., Pilewskie, P., Chen, H., Cochrane, S. P., Sedlacek, A. J., Lang, T. J., Stith, E., Segal-Rozenhaimer, M., Ferrare, R. A., Burton, S. P., Hostetler, C. A., Diner, D. J., Seidel, F. C., Platnick, S. E., Myers, J. S., Meyer, K. G., Spangenberg, D. A., Maring, H., and Gao, L.: An overview of the ORACLES (ObseRvations of aerosols above CLouds and their intEractionS) project: Aerosol-cloud-radiation interactions in the southeast Atlantic basin, Atmospheric Chem. Phys., 21, 1507–1563, https://doi.org/10.5194/ACP-21-1507-2021, 2021.

Reid, C. E., Brauer, M., Johnston, F. H., Jerrett, M., Balmes, J. R., and Elliott, C. T.: Critical Review of Health Impacts of Wildfire Smoke Exposure, Environ. Health Perspect., 124, 1334–1343, https://doi.org/10.1289/ehp.1409277, 2016.

Reid, J. S., Hobbs, P. V., Ferek, R. J., Blake, D. R., Martins, J. V., Dunlap, M. R., and Liousse, C.: Physical, chemical, and optical properties of regional hazes dominated by smoke in Brazil, J. Geophys. Res. Atmospheres, 103, 32059–32080, https://doi.org/10.1029/98JD00458, 1998.

Rickly, P. S., Guo, H., Campuzano-Jost, P., Jimenez, J. L., Wolfe, G. M., Bennett, R., Bourgeois, I., Crounse, J. D., Dibb, J. E., Digangi, J. P., Diskin, G. S., Dollner, M., Gargulinski, E. M., Hall, S. R., Halliday, H. S., Hanisco, T. F., Hannun, R. A., Liao, J., Moore, R., Nault, B. A., Nowak, J. B., Peischl, J., Robinson, C. E., Ryerson, T., Sanchez, K. J., Schöberl, M., Soja, A. J., St. Clair, J. M., Thornhill, K. L., Ullmann, K., Wennberg, P. O., Weinzierl, B., Wiggins, E. B., Winstead, E. L., and Rollins, A. W.: Emission factors and evolution of SO2 measured from biomass burning in wildfires and agricultural fires, Atmospheric Chem. Phys., 22, 15603–15620, https://doi.org/10.5194/ACP-22-15603-2022, 2022.

Saide, P. E., Spak, S. N., Carmichael, G. R., Mena-Carrasco, M. A., Yang, Q., Howell, S., Leon, D. C., Snider, J. R., Bandy, A. R., Collett, J. L., Benedict, K. B., De Szoeke, S. P., Hawkins, L. N., Allen, G., Crawford, I., Crosier, J., and Springston, S. R.: Evaluating WRF-chem aerosol indirect effects in southeast pacific marine stratocumulus during VOCALS-REx, Atmospheric Chem. Phys., 12, 3045–3064, https://doi.org/10.5194/acp-12-3045-2012, 2012.

Saide, P. E., Peterson, D. A., da Silva, A., Anderson, B., Ziemba, L. D., Diskin, G., Sachse, G., Hair, J., Butler, C., Fenn, M., Jimenez, J. L., Campuzano-Jost, P., Perring, A. E., Schwarz, J. P., Markovic, M. Z., Russell, P., Redemann, J., Shinozuka, Y., Streets, D. G., Yan, F., Dibb, J., Yokelson, R., Toon, O. B., Hyer, E., and Carmichael, G. R.: Revealing important nocturnal and day-to-day variations in fire smoke emissions through a multiplatform inversion, Geophys. Res. Lett., 42, 3609–3618, https://doi.org/10.1002/2015GL063737, 2015.

Saide, P. E., Gao, M., Lu, Z., Goldberg, D. L., Streets, D. G., Woo, J. H., Beyersdorf, A., Corr, C. A., Thornhill, K. L., Anderson, B., Hair, J. W., Nehrir, A. R., Diskin, G. S., Jimenez, J. L., Nault,

B. A., Campuzano-Jost, P., Dibb, J., Heim, E., Lamb, K. D., Schwarz, J. P., Perring, A. E., Kim, J., Choi, M., Holben, B., Pfister, G., Hodzic, A., Carmichael, G. R., Emmons, L., and Crawford, J. H.: Understanding and improving model representation of aerosol optical properties for a Chinese haze event measured during KORUS-AQ, Atmospheric Chem. Phys., 20, 6455–6478, https://doi.org/10.5194/ACP-20-6455-2020, 2020.

Saide, P. E., Thapa, L. H., Ye, X., Pagonis, D., Campuzano-Jost, P., Guo, H., Schuneman, M. L., Jimenez, J.-L., Moore, R., Wiggins, E., Winstead, E., Robinson, C., Thornhill, L., Sanchez, K., Wagner, N. L., Ahern, A., Katich, J. M., Perring, A. E., Schwarz, J. P., Lyu, M., Holmes, C. D., Hair, J. W., Fenn, M. A., and Shingler, T. J.: Understanding the Evolution of Smoke Mass Extinction Efficiency Using Field Campaign Measurements, Geophys. Res. Lett., 49, e2022GL099175, https://doi.org/10.1029/2022GL099175, 2022.

Saide, P. E., Krishna, M., Ye, X., Thapa, L. H., Turney, F., Howes, C., and Schmidt, C. C.: Estimating Fire Radiative Power Using Weather Radar Products for Wildfires, Geophys. Res. Lett., 50, e2023GL104824, https://doi.org/10.1029/2023GL104824, 2023.

Saliba, G., Chen, C. L., Lewis, S., Russell, L. M., Rivellini, L. H., Lee, A. K. Y., Quinn, P. K., Bates, T. S., Haëntjens, N., Boss, E. S., Karp-Boss, L., Baetge, N., Carlson, C. A., and Behrenfeld, M. J.: Factors driving the seasonal and hourly variability of sea-spray aerosol number in the North Atlantic, Proc. Natl. Acad. Sci. U. S. A., 116, 20309–20314, https://doi.org/10.1073/PNAS.1907574116/SUPPL_FILE/PNAS.1907574116.SD01.XLSX, 2019.

Schneider, T., Teixeira, J., Bretherton, C. S., Brient, F., Pressel, K. G., Schär, C., and Siebesma, A. P.: Climate goals and computing the future of clouds, Nat. Clim. Change 2017 71, 7, 3–5, https://doi.org/10.1038/nclimate3190, 2017.

Sedlacek, A. J., Lewis, E. R., Onasch, T. B., Zuidema, P., Redemann, J., Jaffe, D., and Kleinman, L. I.: Using the Black Carbon Particle Mixing State to Characterize the Lifecycle of Biomass Burning Aerosols, Environ. Sci. Technol., 56, 14315–14325, https://doi.org/10.1021/ACS.EST.2C03851/ASSET/IMAGES/LARGE/ES2C03851_0003.JPEG, 2022.

Shinozuka, Y., Saide, P. E., Ferrada, G. A., Burton, S. P., Ferrare, R., Doherty, S. J., Gordon, H., Longo, K., Mallet, M., Feng, Y., Wang, Q., Cheng, Y., Dobracki, A., Freitag, S., Howell, S. G., LeBlanc, S., Flynn, C., Segal-Rosenhaimer, M., Pistone, K., Podolske, J. R., Stith, E. J., Bennett, J. R., Carmichael, G. R., da Silva, A., Govindaraju, R., Leung, R., Zhang, Y., Pfister, L., Ryoo, J.-M., Redemann, J., Wood, R., and Zuidema, P.: Modeling the smoky troposphere of the southeast Atlantic: a comparison to ORACLES airborne observations from September of 2016, Atmospheric Chem. Phys., 20, 11491–11526, https://doi.org/10.5194/acp-20-11491-2020, 2020.

Shrivastava, M., Cappa, C. D., Fan, J., Goldstein, A. H., Guenther, A. B., Jimenez, J. L., Kuang, C., Laskin, A., Martin, S. T., Ng, N. L., Petaja, T., Pierce, J. R., Rasch, P. J., Roldin, P., Seinfeld, J. H., Shilling, J., Smith, J. N., Thornton, J. A., Volkamer, R., Wang, J., Worsnop, D. R., Zaveri, R. A., Zelenyuk, A., and Zhang, Q.: Recent advances in understanding secondary organic aerosol: Implications for global climate forcing, Rev. Geophys., 55, 509–559, https://doi.org/10.1002/2016RG000540, 2017.

Skamarock, W. C., Klemp, J. B., Dudhia, J., Gill, D. O., Barker, D. M., Duda, M. G., Huang, X.-Y., Wang, W., and Powers, J. G.: A Description of the Advanced Research WRF Version 3, 2008.

Spracklen, D. V., Logan, J. A., Mickley, L. J., Park, R. J., Yevich, R., Westerling, A. L., and Jaffe, D. A.: Wildfires drive interannual variability of organic carbon aerosol in the western U.S. in summer, Geophys. Res. Lett., 34, https://doi.org/10.1029/2007GL030037, 2007.

Stephens, G. L., L'Ecuyer, T., Forbes, R., Gettlemen, A., Golaz, J. C., Bodas-Salcedo, A., Suzuki, K., Gabriel, P., and Haynes, J.: Dreary state of precipitation in global models, J. Geophys. Res. Atmospheres, 115, 24211, https://doi.org/10.1029/2010JD014532, 2010.

Stowell, J. D., Geng, G., Saikawa, E., Chang, H. H., Fu, J., Yang, C.-E., Zhu, Q., Liu, Y., and Strickland, M. J.: Associations of wildfire smoke PM2.5 exposure with cardiorespiratory events in Colorado 2011–2014, Environ. Int., 133, 105151, https://doi.org/10.1016/j.envint.2019.105151, 2019.

Szopa, S., Naik, V., B., A., P., A., Berntsen, T., Collins, W.D., Fuzzi, S., Gallardo, L., Kiendler-Scharr, A., Klimont, Z., Liao, H., Unger, N., and Zanis, P.: Climate Change 2021 – The Physical Science Basis: Working Group I Contribution to the Sixth Assessment Report of the Intergovernmental Panel on Climate Change, 817–922, https://doi.org/10.1017/9781009157896.008, 2021.

Tang, S., Fast, J. D., Zhang, K., Hardin, J. C., Varble, A. C., Shilling, J. E., Mei, F., Zawadowicz, M. A., and Ma, P. L.: Earth System Model Aerosol-Cloud Diagnostics (ESMAC Diags) package, version 1: Assessing E3SM aerosol predictions using aircraft, ship, and surface measurements, Geosci. Model Dev., 15, 4055–4076, https://doi.org/10.5194/GMD-15-4055-2022, 2022a.

Tang, W., Emmons, L. K., Buchholz, R. R., Wiedinmyer, C., Schwantes, R. H., He, C., Kumar, R., Pfister, G. G., Worden, H. M., Hornbrook, R. S., Apel, E. C., Tilmes, S., Gaubert, B., Martinez-Alonso, S.-E., Lacey, F., Holmes, C. D., Diskin, G. S., Bourgeois, I., Peischl, J., Ryerson, T. B., Hair, J. W., Weinheimer, A. J., Montzka, D. D., Tyndall, G. S., and Campos, T. L.: Effects of Fire Diurnal Variation and Plume Rise on U.S. Air Quality During FIREX-AQ and WE-CAN Based on the Multi-Scale Infrastructure for Chemistry and Aerosols (MUSICAv0), J. Geophys. Res. Atmospheres, 127, e2022JD036650, https://doi.org/10.1029/2022JD036650, 2022b.

Tang, W., Emmons, L. K., Worden, H. M., Kumar, R., He, C., Gaubert, B., Zheng, Z., Tilmes, S., Buchholz, R. R., Martinez-Alonso, S.-E., Granier, C., Soulie, A., McKain, K., Daube, B. C., Peischl, J., Thompson, C., and Levelt, P.: Application of the Multi-Scale Infrastructure for Chemistry and Aerosols version 0 (MUSICAv0) for air quality research in Africa, Geosci. Model Dev., 16, 6001–6028, https://doi.org/10.5194/gmd-16-6001-2023, 2023.

Taylor, J. W., Allan, J. D., Allen, G., Coe, H., Williams, P. I., Flynn, M. J., Le Breton, M., Muller, J. B. A., Percival, C. J., Oram, D., Forster, G., Lee, J. D., Rickard, A. R., Parrington, M., and

Palmer, P. I.: Size-dependent wet removal of black carbon in Canadian biomass burning plumes, Atmos Chem Phys, 14, 13755–13771, https://doi.org/10.5194/acp-14-13755-2014, 2014.

Taylor, J. W., Wu, H., Szpek, K., Bower, K., Crawford, I., Flynn, M. J., Williams, P. I., Dorsey, J., Langridge, J. M., Cotterell, M. I., Fox, C., Davies, N. W., Haywood, J. M., Coe, H., and Taylor, J.: Absorption closure in highly aged biomass burning smoke, Atmos Chem Phys, 20, 11201–11221, https://doi.org/10.5194/acp-20-11201-2020, 2020.

Thapa, L. H., Ye, X., Hair, J. W., Fenn, M. A., Shingler, T., Kondragunta, S., Ichoku, C., Dominguez, R., Ellison, L., Soja, A. J., Gargulinski, E., Ahmadov, R., James, E., Grell, G. A., Freitas, S. R., Pereira, G., and Saide, P. E.: Heat flux assumptions contribute to overestimation of wildfire smoke injection into the free troposphere, Commun. Earth Environ., 3, 1–11, https://doi.org/10.1038/s43247-022-00563-x, 2022.

Tilmes, S., Hodzic, A., Emmons, L. K., Mills, M. J., Gettelman, A., Kinnison, D. E., Park, M., Lamarque, J.-F., Vitt, F., Shrivastava, M., Campuzano-Jost, P., Jimenez, J. L., and Liu, X.: Climate Forcing and Trends of Organic Aerosols in the Community Earth System Model (CESM2), J. Adv. Model. Earth Syst., 11, 4323–4351, https://doi.org/10.1029/2019MS001827, 2019.

Trenberth, K. E. and Zhang, Y.: How Often Does It Really Rain?, Bull. Am. Meteorol. Soc., 99, 289–298, https://doi.org/10.1175/BAMS-D-17-0107.1, 2018.

Trenberth, K. E., Dai, A., Rasmussen, R. M., and Parsons, D. B.: The Changing Character of Precipitation, Bull. Am. Meteorol. Soc., 84, 1205–1218, https://doi.org/10.1175/BAMS-84-9-1205, 2003.

US EPA, O.: 2017 National Emissions Inventory (NEI) Data (2017), 2017.

van der Velde, I. R., van der Werf, G. R., Houweling, S., Maasakkers, J. D., Borsdorff, T., Landgraf, J., Tol, P., van Kempen, T. A., van Hees, R., Hoogeveen, R., Veefkind, J. P., and Aben, I.: Vast CO2 release from Australian fires in 2019–2020 constrained by satellite, Nature, 597, 366–369, https://doi.org/10.1038/s41586-021-03712-y, 2021.

Waquet, F., Peers, F., Ducos, F., Goloub, P., Platnick, S., Riedi, J., Tanré, D., and Thieuleux, F.: Global analysis of aerosol properties above clouds, Geophys. Res. Lett., 40, 5809–5814, https://doi.org/10.1002/2013GL057482, 2013.

Weber, K. T. and Yadav, R.: Spatiotemporal Trends in Wildfires across the Western United States (1950–2019), Remote Sens., 12, 2959, https://doi.org/10.3390/rs12182959, 2020.

van der Werf, G. R., Randerson, J. T., Giglio, L., Collatz, G. J., Mu, M., Kasibhatla, P. S., Morton, D. C., DeFries, R. S., Jin, Y., and van Leeuwen, T. T.: Global fire emissions and the contribution of deforestation, savanna, forest, agricultural, and peat fires (1997–2009), Atmospheric Chem. Phys., 10, 11707–11735, https://doi.org/10.5194/acp-10-11707-2010, 2010.

Wiggins, E. B., Soja, A. J., Gargulinski, E., Halliday, H. S., Pierce, R. B., Schmidt, C. C., Nowak, J. B., DiGangi, J. P., Diskin, G. S., Katich, J. M., Perring, A. E., Schwarz, J. P., Anderson, B. E., Chen, G., Crosbie, E. C., Jordan, C., Robinson, C. E., Sanchez, K. J., Shingler, T. J., Shook, M., Thornhill, K. L., Winstead, E. L., Ziemba, L. D., and Moore, R. H.: High Temporal Resolution Satellite Observations of Fire Radiative Power Reveal Link Between Fire Behavior and Aerosol and Gas Emissions, Geophys. Res. Lett., 47, e2020GL090707, https://doi.org/10.1029/2020GL090707, 2020.

Wilcox, E. M.: Stratocumulus cloud thickening beneath layers of absorbing smoke aerosol, Atmospheric Chem. Phys., 10, 11769–11777, https://doi.org/10.5194/ACP-10-11769-2010, 2010.

Winijkul, E., Yan, F., Lu, Z., Streets, D. G., Bond, T. C., and Zhao, Y.: Size-resolved global emission inventory of primary particulate matter from energy-related combustion sources, Atmos. Environ., 107, 137–147, https://doi.org/10.1016/j.atmosenv.2015.02.037, 2015.

Wonaschütz, A., Coggon, M., Sorooshian, A., Modini, R., Frossard, A. A., Ahlm, L., Mülmenstädt, J., Roberts, G. C., Russell, L. M., Dey, S., Brechtel, F. J., and Seinfeld, J. H.: Hygroscopic properties of smoke-generated organic aerosol particles emitted in the marine atmosphere, Atmospheric Chem. Phys., 13, 9819–9835, https://doi.org/10.5194/ACP-13-9819-2013, 2013.

Wooster, M. J.: Small-scale experimental testing of fire radiative energy for quantifying mass combusted in natural vegetation fires, Geophys. Res. Lett., 29, 23-1-23–4, https://doi.org/10.1029/2002GL015487, 2002.

Wu, H., Taylor, J. W., Szpek, K., Langridge, J. M., Williams, P. I., Flynn, M., Allan, J. D., Abel, S. J., Pitt, J., Cotterell, M. I., Fox, C., Davies, N. W., Haywood, J., and Coe, H.: Vertical variability of the properties of highly aged biomass burning aerosol transported over the southeast Atlantic during CLARIFY-2017, Atmos Chem Phys, 20, 12697–12719, https://doi.org/10.5194/acp-20-12697-2020, 2020.

Wyant, M. C., Bretherton, C. S., Wood, R., Carmichael, G. R., Clarke, A., Fast, J., George, R., Gustafson Jr., W. I., Hannay, C., Lauer, A., Lin, Y., Morcrette, J.-J., Mulcahy, J., Saide, P. E., Spak, S. N., and Yang, Q.: Global and regional modeling of clouds and aerosols in the marine boundary layer during VOCALS: the VOCA intercomparison, Atmospheric Chem. Phys., 15, 153–172, https://doi.org/10.5194/acp-15-153-2015, 2015.

XiaoCong, W., Liu, Y., and Bao, Q.: Impacts of cloud overlap assumptions on radiative budgets and heating fields in convective regions, Atmospheric Res., 167, 89–99, https://doi.org/10.1016/j.atmosres.2015.07.017, 2016.

Xu, W., Wooster, M. J., Roberts, G., and Freeborn, P.: New GOES imager algorithms for cloud and active fire detection and fire radiative power assessment across North, South and Central America, Remote Sens. Environ., 114, 1876–1895, https://doi.org/10.1016/j.rse.2010.03.012, 2010.

Xu, W., Wooster, M. J., He, J., and Zhang, T.: Improvements in high-temporal resolution active fire detection and FRP retrieval over the Americas using GOES-16 ABI with the geostationary Fire Thermal Anomaly (FTA) algorithm, Sci. Remote Sens., 3, 100016, https://doi.org/10.1016/j.srs.2021.100016, 2021.

Yamaguchi, T., Feingold, G., Kazil, J., and McComiskey, A.: Stratocumulus to cumulus transition in the presence of elevated smoke layers, Geophys. Res. Lett., 42, 10478–10485, https://doi.org/10.1002/2015GL066544, 2015.

Yamaguchi, T., Feingold, G., and Kazil, J.: Stratocumulus to Cumulus Transition by Drizzle, J. Adv. Model. Earth Syst., 9, 2333–2349, https://doi.org/10.1002/2017MS001104, 2017.

Ye, X., Arab, P., Ahmadov, R., James, E., Grell, G. A., Pierce, B., Kumar, A., Makar, P., Chen, J., Davignon, D., Carmichael, G. R., Ferrada, G., Mcqueen, J., Huang, J., Kumar, R., Emmons, L., Herron-Thorpe, F. L., Parrington, M., Engelen, R., Peuch, V.-H., Da Silva, A., Soja, A., Gargulinski, E., Wiggins, E., Hair, J. W., Fenn, M., Shingler, T., Kondragunta, S., Lyapustin, A., Wang, Y., Holben, B., Giles, D. M., and Saide, P. E.: Evaluation and intercomparison of wildfire smoke forecasts from multiple modeling systems for the 2019 Williams Flats fire, Atmos Chem Phys, 21, 14427–14469, https://doi.org/10.5194/acp-21-14427-2021, 2021.

Ye, X., Saide, P. E., Hair, J., Fenn, M., Shingler, T., Soja, A., Gargulinski, E., and Wiggins, E.: Assessing Vertical Allocation of Wildfire Smoke Emissions Using Observational Constraints From Airborne Lidar in the Western U.S., J. Geophys. Res. Atmospheres, 127, e2022JD036808, https://doi.org/10.1029/2022JD036808, 2022.

Yu, P., Froyd, K. D., Portmann, R. W., Toon, O. B., Freitas, S. R., Bardeen, C. G., Brock, C., Fan, T., Gao, R. S., Katich, J. M., Kupc, A., Liu, S., Maloney, C., Murphy, D. M., Rosenlof, K. H., Schill, G., Schwarz, J. P., and Williamson, C.: Efficient In-Cloud Removal of Aerosols by Deep Convection, Geophys. Res. Lett., 46, 1061–1069, https://doi.org/10.1029/2018GL080544, 2019.

Zaveri, R. A. and Peters, L. K.: A new lumped structure photochemical mechanism for large-scale applications, J. Geophys. Res. Atmospheres, 104, 30387–30415, https://doi.org/10.1029/1999JD900876, 1999.

Zawadowicz, M. A., Lee, B. H., Shrivastava, M., Zelenyuk, A., Zaveri, R. A., Flynn, C., Thornton, J. A., and Shilling, J. E.: Photolysis Controls Atmospheric Budgets of Biogenic Secondary Organic Aerosol, Environ. Sci. Technol., 54, 3861–3870, https://doi.org/10.1021/ACS.EST.9B07051, 2020.

Zender, C. S., Bian, H., and Newman, D.: Mineral Dust Entrainment and Deposition (DEAD) model: Description and 1990s dust climatology, J. Geophys. Res. Atmospheres, 108, 4416, https://doi.org/10.1029/2002JD002775, 2003.

Zhai, J., Lu, X., Li, L., Zhang, Q., Zhang, C., Chen, H., Yang, X., and Chen, J.: Size-resolved chemical composition, effective density, and optical properties of biomass burning particles, Atmospheric Chem. Phys., 17, 7481–7493, https://doi.org/10.5194/acp-17-7481-2017, 2017.

Zhang, H., Hu, D., Chen, J., Ye, X., Wang, S. X., Hao, J. M., Wang, L., Zhang, R., and An, Z.: Particle size distribution and polycyclic aromatic hydrocarbons emissions from agricultural crop residue burning, Environ. Sci. Technol., 45, 5477–5482, https://doi.org/10.1021/es1037904, 2011.

Zhang, J. and Zuidema, P.: The diurnal cycle of the smoky marine boundary layer observed during August in the remote southeast Atlantic, Atmospheric Chem. Phys., 19, 14493–14516, https://doi.org/10.5194/ACP-19-14493-2019, 2019.

Zhang, J. and Zuidema, P.: Sunlight-absorbing aerosol amplifies the seasonal cycle in low-cloud fraction over the southeast Atlantic, Atmos Chem Phys, 21, 11179–11199, https://doi.org/10.5194/acp-21-11179-2021, 2021.

Zhang, Y., Zhang, X., Wang, K., He, J., Leung, L. R., Fan, J., and Nenes, A.: Incorporating an advanced aerosol activation parameterization into WRF-CAM5: Model evaluation and parameterization intercomparison, J. Geophys. Res. Atmospheres, 120, 6952–6979, https://doi.org/10.1002/2014JD023051, 2015.

Zhang, Z., Meyer, K., Yu, H., Platnick, S., Colarco, P., Liu, Z., and Oreopoulos, L.: Shortwave direct radiative effects of above-cloud aerosols over global oceans derived from 8 years of CALIOP and MODIS observations, Atmospheric Chem. Phys., 16, 2877–2900, https://doi.org/10.5194/acp-16-2877-2016, 2016.

Zheng, G., Wang, Y., Wood, R., Jensen, M. P., Kuang, C., McCoy, I. L., Matthews, A., Mei, F., Tomlinson, J. M., Shilling, J. E., Zawadowicz, M. A., Crosbie, E., Moore, R., Ziemba, L., Andreae, M. O., and Wang, J.: New particle formation in the remote marine boundary layer, Nat. Commun. 2021 121, 12, 1–10, https://doi.org/10.1038/s41467-020-20773-1, 2021.

Zhou, X., Ackerman, A. S., Fridlind, A. M., Wood, R., and Kollias, P.: Impacts of solar-absorbing aerosol layers on the transition of stratocumulus to trade cumulus clouds, Atmospheric Chem. Phys., 17, 12725–12742, https://doi.org/10.5194/acp-17-12725-2017, 2017.

Zorn, S. R., Drewnick, F., Schott, M., Hoffmann, T., and Borrmann, S.: Characterization of the South Atlantic marine boundary layer aerosol using an aerodyne aerosol mass spectrometer, Atmospheric Chem. Phys., 8, 4711–4728, https://doi.org/10.5194/ACP-8-4711-2008, 2008.

Zuidema, P., Redemann, J., Haywood, J., Wood, R., Piketh, S., Hipondoka, M., and Formenti, P.: Smoke and clouds above the southeast Atlantic: Upcoming field campaigns probe absorbing aerosol's impact on climate, Bull. Am. Meteorol. Soc., 97, 1131–1135, https://doi.org/10.1175/BAMS-D-15-00082.1, 2016.

Zuidema, P., Alvarado, M., Chiu, C., de Szoeke, S., Fairall, C., Feingold, G., Freedman, A., Ghan, S., Haywood, J., Kollias, P., Lewis, E., McFarquhar, G., McComiskey, A., Mechem, D., Onasch, T., Redemann, J., Romps, D., Turner, D., Wang, H., Wood, R., Yuter, S., and Zhu, P.: Layered Atlantic Smoke Interactions with Clouds (LASIC) Field Campaign Report, US Dep. Energy Off. Sci. Tech. Inf., https://doi.org/10.2172/1467425, 2018a.

Zuidema, P., Sedlacek, A. J., Flynn, C., Springston, S., Delgadillo, R., Zhang, J., Aiken, A. C., Koontz, A., and Muradyan, P.: The Ascension Island Boundary Layer in the Remote Southeast Atlantic is Often Smoky, Geophys. Res. Lett., 45, 4456–4465, https://doi.org/10.1002/2017GL076926, 2018b.